Production of steel matrix composites by mechanical milling and spark plasma sintering

Anna Fedrizzi

2 μm

April 2013

PRODUCTION OF STEEL MATRIX COMPOSITES BY

MECHANICAL MILLING AND SPARK PLASMA SINTERING

Anna Fedrizzi

Tutors:

Prof. Massimo Pellizzari,
Department of Industrial Engineering
University of Trento, Italy.

PhD. Mario Zadra,
K4Sint, Italy.

Ph.D. Commission:

Prof. Claudio Migliaresi,
Department of Industrial Engineering
University of Trento, Italy.

Dr. Pranesh Aswath,
Department of Materials Science and
Engineering and Mechanical and
Aerospace Engineering
University of Texas Arlington, USA.

Prof. Orfeo Sbaizero,
Department of Architecture and
Engineering
University of Trieste, Italy.

PhD. Arthur J. Coury,
Coury Consulting Service Boston, USA.

University of Trento,

Department of Industrial Engineering

April 2013

To my beloved A. and L.

Abstract

Hot work tool steels (HWTSs) are ferrous alloys for tooling application, particularly developed to meet high toughness and good hot hardness. Increasing hardness generally leads to a decrease in toughness, therefore metal matrix composite (MMC) coatings and functionally graded materials have been proposed as a good solution for improving wear resistance.

In this PhD thesis powder metallurgy has been applied for the production of particle reinforced HWTSs. Mechanical milling (MM) and mechanical alloying (MA) have been considered as suited techniques for the production of powders showing higher sinterability and finer microstructure. Spark plasma sintering (SPS) has been used for the consolidation. As reinforcement a harder high speed steel (HSS) and different ceramic powders (TiB_2, TiC and TiN) have been selected.

The production of HWTS/HSS blends has highlighted the negative interaction on densification of the two components due to their different sintering kinetics. This interference can be minimised by selecting powders with smaller particles size. With this respect MM was proved to be a very useful method, which enhances sintering. Fully dense blends with good dispersion of the reinforcing particles can be sintered using small sized powders and setting the particle size ratio (PSR) smaller than 1.

For the production of MMCs the formation of aggregates has been overcome by MA which promotes a uniform dispersion of hard particles into the parent steel. Among the reinforcement considered in this work, TiB_2 is not suitable because it reacts with steel depleting carbon and producing TiC and brittle Fe_2B. HWTS composites with 20%vol of TiC can be fully densified by SPS at 1100 °C for 30 minutes and 60 MPa uniaxial pressure. On the other hand TiN-reinforced MMC shows high resistance to densification and fully dense materials could not be produced.

Table of contents

Chapter I

Introduction

Hot work tool steels (HWTSs) are ferrous alloys for tooling application, particularly developed to meet high toughness and good hot hardness (Roberts et al., 1992). They find application for the production of tools working at temperature higher than 300 °C, such as forging, die casting, extrusion dies and punches. Their lower carbon content results in a lower amount of carbides than the one of cold work tool steels or high speed steels (HSSs). These carbides are mainly vanadium carbides, which are quite stable at high temperature assuring good hot hardness. Due to their fine distribution these small carbides avoid grain growth during the thermal treatment enhancing material toughness.

It is known that increasing hardness generally leads to a decrease in toughness (Roberts et al., 1992). Therefore to guarantee high toughness these steels are characterized by lower hardness and lower wear resistance than other tool steels, such as HSS. The low wear resistance negatively influences tool performance and life. Since wear resistance strongly depends on material hardness (dos Santos et al., 2007), present solutions to increase tool life intend to increase surface hardness in order to enhance wear resistance without affecting toughness. The most common surface treatments applied to HWTS are nitriding or physical vapour deposition (PVD) of hard coatings (TiN, TiAlN, TiC, CrN…) (dos Santos et al., 2007; Kugler et al., 2006; Söderberg, 2001). Some systems, called duplex treatment, combine nitriding and PVD coatings (Duarte et al., 2009). The nitrided surface layer increases the load bearing capability of the hard and brittle coating improving its resistance to crack which is one of the most common causes of failure for these systems. The main limitations of these solutions are the low hardening depth and the low thickness of the hard coating. When wear starts to damage the thin hard surface layer the substrate remains without any protection and its deterioration suddenly increases leading to quick failure.

In order to further improve the load bearing capability of hard surface layers and to increase tool life thick metal matrix composite (MMC) coatings and functionally graded materials (FGMs) have been proposed (Matula et al., 2006; Rajasekaran et al., 2010). These systems combine the toughness and strength of the metal phase with the high hardness and wear resistance of the ceramic

constituent. Their thickness guarantees longer protection of the substrate and their tailored properties improve hard layer adhesion and reduce residual thermal stresses in the component. Due to their complexity and to the high number of variables influencing their final behaviour their design is quite elaborate and their production can be relatively expensive, but their promising properties encourage research in this field. It has been demonstrated that in general particle reinforcement improves the wear resistance of steel, (Akhtar, 2008; Berns, 2003; Berns et al., 1999; Oliveira et al., 1999; Pagounis et al., 1997; Pagounis et al., 1998; Tjong et al., 1999[2]), but not much work has been done on reinforced HWTSs.

The fundamental goal of this PhD thesis is to study and develop particle reinforced HWTSs. The composite materials studied in this work have been produced starting from metallic and ceramic powders. Harder steel powders as well as ceramic compounds have been considered as reinforcing particles. Powder Metallurgy (PM) is a technology apt to the production of composite materials (Chawla et al., 2006; Pagounis et al., 1998) and offering many advantages such as a finer and more homogeneous microstructure which results in increasing both hardness and toughness (Grinder, 1999).

Generally speaking material properties are strongly influenced by the phase distribution and densification (Akhtar, 2008). In this work mechanical milling (MM) and mechanical alloying (MA) have been considered to improve the hard phase dispersion (Liu et al., 2001). MA is a solid state process performed at low temperature thus reducing or avoiding chemical reactions between metallic and ceramic phases. Moreover MM and MA refine both the metallic microstructure and the powder particle size (Zoz et al., 2003). The microstructure refinement results in increased strength and the particle size reduction enhances sintering and densification.

The materials investigated in this work have been sintered by Spark Plasma Sintering (SPS). This technology applies a uniaxial pressure and a pulsed direct continuous (DC) current allowing sintering at lower temperature and in a shorter time comparing to conventional processes like hot isostatic pressing (HIP) (Li et al., 2010; Mamedov, 2002). The high heating rate and the DC current pulses preserve the fine microstructure produced by MM and reduce the interaction between the metal matrix and the reinforcing particles (Zoz et al., 2003).

This PhD thesis is divided into two main parts. The first one, following previous studies on the sintering of tool steel blends (Pellizzari et al., 2009), is aimed at the investigation of the advantages deriving from MM on the densification and the mechanical properties of HWTS/HSS blends. The second part is focused on the development of HWTS based MMCs. The influence of the MMC processing route on the hard phase distribution and on densification has been investigated. Two different processing routes have been considered: in the first one pure HWTS has been mechanically milled and then mixed with the reinforcing ceramic powder while in the

second one steel and ceramic powders have been mechanically alloyed. Finally the MA process has been applied to produce MMCs with different reinforcing types (carbides, nitrides and borides). The interactions between the matrix and the reinforcing phases have been studied and the properties of the different MMCs have been compared.

Chapter II

Metal Matrix Composite Materials

2.1   Introduction

Depending on their development and their applications different definitions of composite materials have been proposed. Staab (1999) considers as composite materials a material which contains two or more distinct constituents with significantly different macroscopic behaviour and a distinct interface between each constituent. Generally speaking it is possible to identify a continuous phase, named matrix, which embeds a more discontinuous phase, called reinforcement (Staab, 1999). Composite materials have been developed to combine the different characteristics of the matrix and the reinforcement in a new material with novel properties. They have a peculiar feature which makes them very attractive for many different applications, i.e. their possibility to meet a wide range of properties (Akhtar, 2008; Pagounis et al., 1997; Sadagopan et al., 1998). This means that their composition and internal architecture can be manipulated to achieve the desired properties. This design is rather complex and involves the optimization of several variables, such as the reinforcement geometry, the matrix and reinforcement materials, the architecture of reinforcement arrangement and the volume fraction of reinforcement phase.

Among all composite materials, MMCs are a class of composites in which rigid ceramic reinforcements are embedded in a ductile metal or alloy matrix (Tjong et al., 2000). The combination of hard ceramic particles with a metal matrix permits to increase the hardness and stiffness preserving the suited toughness and machinability of the metal matrix material (Akhtar, 2008; Berns, 2003; Degnan et al., 2002; Pagounis et al., 1997; Pagounis et al., 1998; Tjong et al., 1999[1]; Tjong et al., 2000). Although historically research has been mainly focused on other alloys (Angers et al., 1999; Tjong et al., 1999[1]), recently interest in steel matrix has grown (Akhtar, 2008; Berns et al., 1999; Degnan et al., 2002; Farid et al., 2007; Li et al., 2010; Tjong et al., 1999[2]), also including MMCs based on tool steel matrix (Berns, 2003; Bolton et al., 1998; Lemster et al., 2006; Liu et al., 2001; Oliveira et al., 1999; Pagounis et al., 1997; Pagounis et al., 1998; Rajasekaran et al., 2010). Steel matrix composites are quite fascinating materials for many high temperature applications, including tooling and automotive, since they combine high hardness and wear

4

resistance of ceramic particles with the toughness and hot strength characteristic of iron alloys (Oliveira et al., 1999; Pagounis et al., 1997; Pagounis et al., 1998; Tjong et al., 1999[2]).

2.2 Reinforcing Mechanisms

MMCs were firstly developed to increase strength and elastic moduli of light metals for aerospace applications (Pagounis et al., 1998). At the beginning aligned continuous fibres were used as reinforcement, but later they were replaced by less expensive ceramic particulates (Pagounis et al., 1998). These materials showed very high wear resistance which is a main requirement in many industrial applications, such as for metal forming tools. Nowadays the best wear resistant materials are cermets, i.e. ceramic particles bounded together by a thin layer of metal matrix, but their high costs reduce their competitiveness comparing to MMCs based on highly wear resistant iron alloys (Pagounis et al., 1997). In the last decades the production of steel based particle reinforced MMCs has gained increased scientific and industrial interest (Pagounis et al., 1997). Some companies have already developed tool steel matrix composites which are now commercially available, such as Ferro-TiC® by Reade (Reade) or Ferro-Titanit® by Deutsche Edelstahlwerke GmbH (Deutsche Edelstahlwerke). These materials are TiC reinforced machineable and hardenable alloy/steel produced by PM. They combine steel and cemented carbide properties particularly showing high wear resistance and they find applications for high-production tooling, highly wear resistant parts, high temperatures and severe corrosion resistant components and for tools requiring additional toughness. Due to their hardenable steel matrix, which can vary from tool steels to stainless steels, in the annealed condition these carbide-alloyed materials can be easily machined by customary methods and then a conventional heat treatment guarantees the achievement of their maximum hardness.

The two constituents of MMCs have different duties: the hard particles (HPs) have to withstand wear by grooving or indenting; the metal matrix has to guarantee toughness and enough support for the HPs (Berns, 2003).

From the mechanical and tribological point of view not all the HPs and metal matrix combinations are good for producing a tough and wear resistant composite. Both properties depend on the hardness and toughness of the base constituents but they are also strongly influenced by the amount, size and distribution of HPs as well as by the strength of the HP and metal matrix bond (Berns, 2003). Previous studies (Berns, 2003; Berns et al., 1996; Berns et al., 1997; Zum Gahr, 1998) deeply investigated these relations. HPs improve the resistance against grooving wear only if they are bigger and of course harder than the abrasive medium (Berns et al., 1997; Zum Gahr, 1998). Figure 1 schematically shows the interactions between the HPs and the abrasive medium. Small HPs (Fig. 1a,c) can be easily dug out by both hard

and soft abrasive medium. Bigger HPs can substantially reduce the abrasion depth if they are well bonded to the matrix and if the mean free path between them is smaller than the abrasive particle size. As the HP size increases, however, the tensile and bending strength heavily decreases (Berns et al., 1996), in view of the lowered cracking resistance as it reported in Figure 2a. At a given content of HPs, their mean spacing increases with particle size. As shown in Figure 2b, when loading a precracked sample, the plastic zone ahead of the crack tip in the metal matrix will not contain any fractured HP, giving rise to improved toughness (Berns et al., 1996). In conclusion there is a suitable HP size which combines the two different requirements: small HPs to reduce the decrease of bending strength and big HPs to increase wear resistance and to improve fracture toughness due to the larger particle spacing.
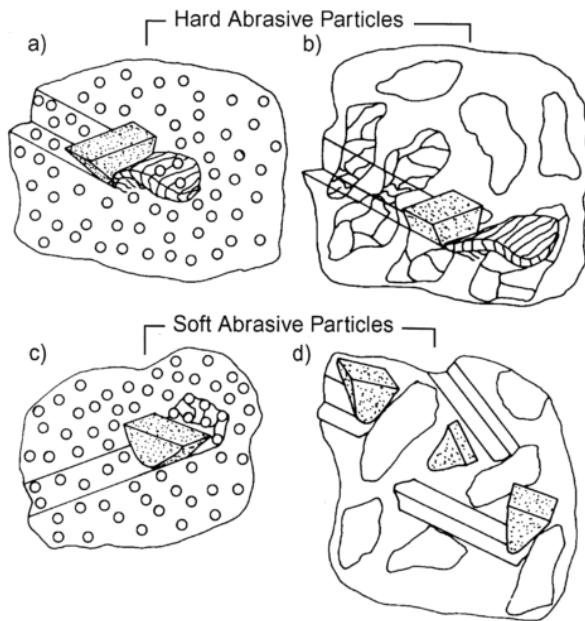
Figure II – 1. Interactions between HPs and abrasive medium. HP size increases moving from left to right (adapted from Zum Gahr, 1998).
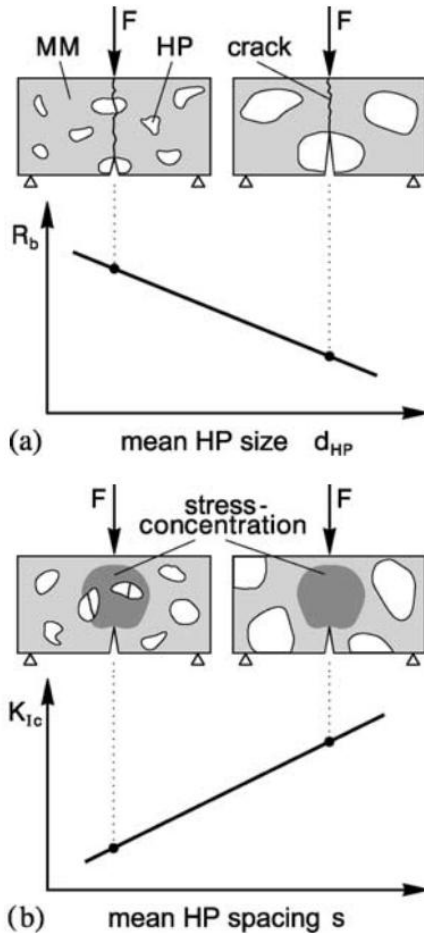
Figure II – 2. Schematic representation of the influence at a give HP content of the mean HP size on the bending strength R_b (a) and of the mean HP spacing on the fracture toughness K_{Ic} (b) (Berns, 2003)**.**

Beside HP size, many studies on MMCs have highlighted the relevance of the HP distribution on the composite properties (Berns et al., 1996; Berns et al., 1998; Liu et al., 2001). To optimize their reinforcing effects HPs have to be finely and homogeneously distributed in the matrix. When producing MMCs by simply mixing the two constituent powders, the HP dispersion is ruled by two factors: the volume ratio (f_{HP}/f_{MM}) and the size ratio (d_{HP}/d_{MM}) (Berns, 2003; Berns et al., 1996; Berns et al., 1998). Figure 3 schematically represent the effects of both factors. To obtain high toughness is important that HPs are well dispersed, i.e. avoid a net-like

arrangement. As the volume fraction ratio increases the size ratio has also to be increased so that the small tough metal matrix particles surround the big HPs as satellites, forming a continuous matrix (Berns, 2003; Berns et al., 1996; Berns et al., 1998).
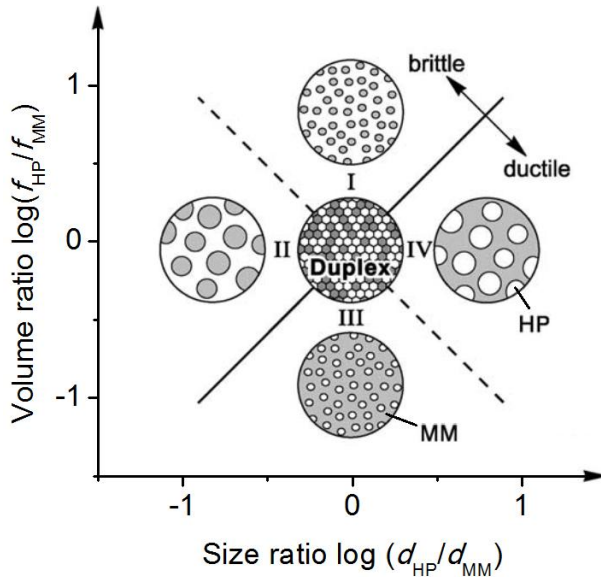
Figure II – 3. Microstructure of MMC produced by powder mixing as a function of the HP volume fraction *f* and of the size ratio *d* (Berns, 2003).

2.2.1 "Double dispersion" microstructure

Considering the opposite influence of HP size on bending strength and on wear resistance, Berns et al. (1996) proposed a new microstructure, composed by a relatively tough metal matrix (MM-I, i.e., HWTS) strengthened by a dispersion of harder particles. In order to contain the decrease of the bending strength, the HPs were replaced by powder particles of a second metal matrix (MM-II, i.e., a HSS) with a fine dispersion of carbides. This microstructure is called "double dispersion" because small HPs, i.e. the carbides, are dispersed in a metal matrix (MM-II) and these particles are dispersed them self in another tough metal matrix (MM-I) (Berns et al., 1996; Berns et al., 1998; Berns et al., 2006). This new design combines the high fracture toughness, owing to large spacing between the harder MM-II particles, with a high bending strength, due to the small carbides (i.e. the brittle phase) in MM-II, and a sufficient wear resistance, through large harder MM-II areas (Berns et al., 1996).

Following the way traced by Berns, hybrid tool steels showing this "double dispersion" microstructure were produced and investigated (Pellizzari et al., 2009). Results showed that properties change almost linearly with the hybrid steel composition giving the possibility to tailor material properties in agreement with the final application.

2.3 MMC Densification Behaviour

As introduced previously, PM is particularly suited for the production of MMCs. As for all PM products, density strongly determines MMC properties and therefore it is important to predict the densification behaviour during sintering. Densification strongly depends on the characteristic of the starting powder. According to German (1992[1]; 1992[2]), high packing density is favoured by wide particle size distributions but on the other hand narrow particle size distributions exhibit higher densification rate leading to higher density after sintering. As a result final density generally increases as the mean particle size decreases and as the particle size distribution becomes narrower (Ting et al., 1994; Ting et al., 1995).

Considering MMC production by powder blending, the starting powder is a mixture of soft and hard particles, where the matrix alloy acts as the soft component and the reinforcement particles as the hard one. Literature data about the densification of soft/hard mixture for different kind of materials state that densification still depends on particle size but it is also strongly influenced by other factors such as the volume fraction of reinforcement, the ratio between soft and hard particle size or the reinforcement shape (Bonnenfant et al., 1998; Bouvard, 2000; Cho et al., 2001; Delie et al., 1998; Lange et al., 1991).

Bouvard (2000) examined the densification behaviour under pressure of metal and ceramic powder mixtures. Ceramic HPs are assumed to be non-deforming under the applied pressure, while soft metal particles are assumed to behave in a visco-plastic manner. According to the value of applied pressure, Bouvard (2000) proposed two main densification mechanisms. If the applied pressure is lower than the soft particle yield strength densification results from particle rearrangement. This mechanism is strongly influenced by the particle size distribution and the particle shape and it is favoured by high fraction of HPs. If the applied pressure increases, densification results from plastic or viscous deformation of soft particles. When applied pressure is high enough or the holding time is sufficiently long, particle deformation can lead to full density but the presence of HPs generally hinders the densification. In this situation, Bouvard (2000) distinguished three cases according to the fraction of HPs. If the HP fraction is low, then HPs are well dispersed and, depending on sintering condition, soft particles can deform to fill all the gaps and complete densification can be reached. For a medium content of HPs, these reinforcing particles form aggregates. The pores that Lange et al. (1991) called

"excluded volume" in the middle of these aggregates are difficult to be filled by deformed soft particles and so their presence reduces the relative density of sintered compound. When the volume fraction of HPs is high, HPs form a continuous net, called percolate, which supports part of the external load. In this case plastic deformation of soft particles is difficult and rearrangement of the HP skeleton is also required to achieve high density. As it is schematically shown in Figure 4, the HP fraction which defines the densification behaviour of mixtures depend on the particle size ratio (PSR), defined as the ratio of the mean diameter of soft particles on the mean diameter of HPs (d_{SOFT}/d_{HARD}) (Bonnenfant et al., 1998; Bouvard, 2000). Generally speaking, as PSR decreases densification rate increases and the maximum fraction of HPs which allows densification by soft particle deformation increases. In other words, HP dispersion and thus high density can be achieved even for higher fractions of HPs when the PSR is much lower than one. Other than for high densification, it can be recalled that HPs dispersion is mandatory for achieving good toughness, as stated in paragraph 2.2.
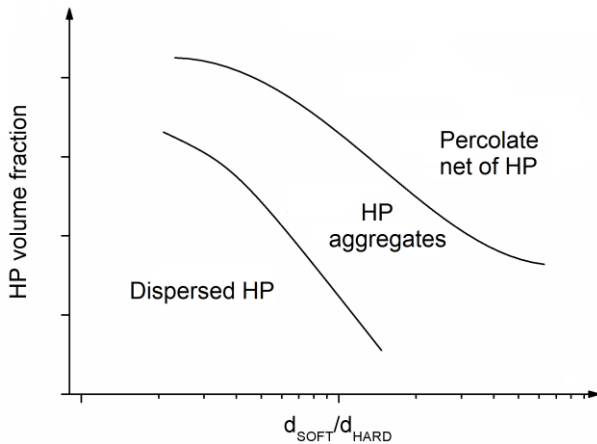
Figure II – 4. HP distribution as a function of the HP volume fraction and of the PSR d_{SOFT}/d_{HARD} (Fedrizzi et al., 2012[1]).

Jagota et al. (1995) showed that the percolation threshold is also influenced by HP contact. This means that if physical and chemical bonds between HPs are weak, these particles can easily slide one against the other allowing high densification even for high volume fraction of reinforcements. On the other hand, if at the beginning of sintering process strong bonds between HPs are created, these result in the formation of a rigid structure which hinders densification and therefore the percolation threshold decreases.

Delie et al. (1998) analysed the effect of HP aspect ratio resulting that it is better to choose spherical HPs with a low specific area, i.e. bigger size, to favour densification processes.

To improve densification of powder mixture with high content of HP the application of cycling pressure has been proposed (Zavaliangos et al., 2000). The pressure cycling achieves a predetermined density applying a lower pressure than static pressing and it is quite promising for the densification of composites with more than 50-60%vol of HPs. Authors suggest that application of cycling pressure improves the HP rearrangement thus increasing densification compared to static pressure (Zavaliangos et al., 2000).

Finer sized reinforcements (<2 µm) result in higher specific mechanical properties, but on the other side they can give significant agglomeration problems resulting in poor dispersion and subsequently less than optimal mechanical properties (Liu et al., 2001). To reduce the problem of agglomeration MA has been proposed as a successful producing route (Angers et al., 1999). MA allows the production of MMCs with a homogeneous distribution of HPs and exhibiting superior mechanical properties (Angers et al., 1999). Therefore MA has been selected as suited technology for the production of MMCs and its fundaments are described in the following chapter.

Chapter III

Innovative powder production and consolidation

3.1 Introduction

Beside costs reduction, materials development aims at increasing materials properties and performances. In the field of tool steels great improvement came from PM technology (Hillskog, 2003; Zhong et al., 2010). PM offers many advantages compared to traditional production routes. First of all PM tool steels present a finer and more homogeneous carbide distribution which results in increasing hardness and improving cracking and fatigue resistance (Hillskog, 2003; Grinder, 1999). This small and uniform carbide structure guarantees a better dimensional stability during heat treatment and an easier machinability (Hillskog, 2003). Moreover the most common solid phase processes for MMC production are based on PM techniques (Chawla et al., 2006). Compared to liquid phase processes, the solid state ones allow better control of the reinforcement distribution and the production of more uniform matrix microstructure. Furthermore they generally involve lower processing temperature thus reducing the reactivity between metal matrix and reinforcement phase (Chawla et al., 2006).

MA has been proposed as an advantageous method for the production of composite powders (Angers et al., 1999; El-eskandarany, 2001; Liu et al., 2001; Suryanarayana, 2001; Zhu et al., 1999). The mechanically alloyed powders are characterized by uniform distribution of reinforcement and the milling process allows the refinement of microstructure as well as of particle size (Huang et al., 1996; Oh-ishi et al., 2007; Zoz et al., 2003). Generally speaking finer mean particle size and narrower particles size distribution improve sintering allowing the production of highly dense materials (Pellizzari et al., 2011[1]; Ting et al., 1994; Ting et al., 1995). A fine microstructure is also beneficial for sintering since small grain size enhances the grain boundary diffusion increasing the sintering rate. In view of all these advantages, in this work MA has been investigated for the production MMC powders and in order to preserve the microstructure refinement and to enhance densification the MA powders have been consolidated by SPS. This emerging technology is very promising for the production of those advanced materials which are difficult to produce by conventional sintering methods, like for example MMCs, fibre reinforced

ceramics, nanocrystalline materials, intermetallic compounds and functionally graded materials (Tokita, 1993).

3.2 Mechanical Milling and Alloying

MM is a high energy process in which metallic powders continuously undergo flattening, cold welding and fragmentation (Maurice et al., 1994). The repetition of all these events causes the modifications in the particle size and morphology and also the evolution of the microstructure.

Originally milling has been developed for the fine reduction of ores and other row materials for many industrial applications. In the last decades this process has gained more relevance also for the development of advanced materials. Nowadays in the metallurgical field MM and MA refer to solid state processes occurring at room temperature in which reactions between the fresh powder surfaces and the reactant materials occur (El-eskandarany, 2001). The main difference between MM and MA lies in the starting powder: generally MA refers to the milling of a mixture of powders during which material transfer is required to homogenize the microstructure; on the other hand MM is the milling of a uniform composition powder which does not need any material transport for homogenization (Suryanarayana, 2001).

At the beginning of the '60 ball milling was firstly applied to produce oxide powders with a metal coating which could not be produced by other methods (El-eskandarany, 2001; Suryanarayana, 2001). Later Benjamin (1970) also used MA for the development of oxide dispersion strengthened nickel alloys opening a new field of research which drew much interest, (Benjamin et al., 1974; Benjamin et al., 1977; Benjamin et al., 1981; Dai et al., 2012; Wilcox et al., 1974). The strong refinement of the microstructure occurring during MM was applied for the development of nanostructured materials, (Fecht, 1995; Kuhrt et al., 1993; Libardi et al., 2008) and longer milling time can even lead to the formation of amorphous phases (Guo et al., 1994; Koch et al., 1983; Salahinejad et al., 2010).

The base principle of MM is that the impacts between the powder and the milling medium cause an energy transfer which is responsible for the morphological and microstructural evolution. Even if this concept is quite simple, MM and MA are complex processes influenced by many variables which determine the final material microstructure and properties (Suryanarayana, 2001). Some parameters which influence the final products are the type of mill, the milling container, the milling speed, the milling time, the grinding medium, ball-to-powder weight ratio (BPR), the extent of filling the vial, the milling atmosphere, the process control agent (PCA) and the temperature of milling (Suryanarayana, 2001). These variables influence the milling process to a different extent and generally they are not completely independent.

There is a large number of different high energy mills suited for MA. Their main differences are their capacity, the speed of operation and the ability to control the operation. The planetary ball mill, which has been used in this work, is one of the most popular and its name comes from the plant-like movements of its vials. The vials indeed rotate around their own axes while they also follow the rotation of the disc on which they are placed (Fig. 1) (El-eskandarany, 2001; Suryanarayana, 2001). The powder and the balls are subjected to both the centrifugal forces which are alternatively synchronized and opposite because the two rotatory motions have opposite directions. Therefore the balls and the powder roll on the inner wall of the vial for a while and then they are lifted and thrown off across the bowl at high speed (Fig. 1) (El-eskandarany, 2001).
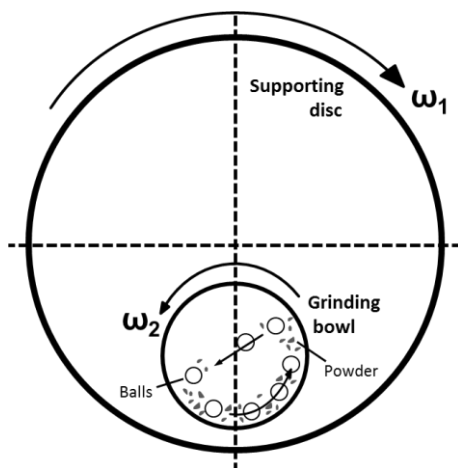
Figure III – 1. Schematic drowing of a high-energy planetary ball mill.

This type of mill can process few hundred grams of powder at a time. Its capacity is higher than other mills, such as the shaker mill. On the other hand its frequency of impacts is much lower, therefore compared to shaker mills, planetary ball mills can be considered lower energy mills (Suryanarayana, 2001).

Generally speaking as milling speed increases the energy input also increases. However, there are some limitations to the maximum speed which can be applied. The energy input usually rises up to a certain speed, then decreases by further speed increase. Therefore, it is possible to determine a critical value of speed which limits the maximum speed (Suryanarayana, 2001). Another limitation is related to the temperature increase. MM is a low efficiency process in which only a small percentage of the total energy is used for the milling process. The major part of energy is wasted and it is turned into heat. Higher speed means higher energy and therefore higher heating. This raise of temperature can be detrimental because it can

cause dynamical recrystallization or the decomposition of supersaturated solid solution or metastable phases (Kuhrt et al., 1993; Suryanarayana, 2001). Low milling speed was shown to favour the formation of amorphous phases (Guo et al., 1994).

Among all parameters the milling time is the one which deeply influence the process. For every system, depending on the type of mill, the energy, the BPR and of course on the milled material, there is an optimum milling time for which the fragmentation and the cold welding processes are in dynamic equilibrium. At this stage the powder presents the minimum particle size and the finest crystallite size, as well (Maurice et al., 1994; Suryanarayana, 2001). In any case too long milling time is to be avoided because the level of contaminations increases (Suryanarayana, 2001).

The BPR strongly influences the time required to produce a specific microstructure: generally the higher the BPR, the shorter is the time required (El-eskandarany, 2001; Suryanarayana, 2001). That is because at high BPR, i.e. when ball weight is proportionally high, the number of collisions per unit time increases resulting in a much higher energy transfer. On the other side the temperature increase must be considered: increasing the energy transfer causes a higher increase of temperature which can change the powder constitution or lead to re-crystallization phenomena.

"Soft" milling conditions (i.e. low BPR, low speed...) favour the formation of metastable phases whereas "hard" conditions produce the equilibrium phases (Suryanarayana, 2001).

3.2.1   Morphological and microstructural evolution

MM is based on the repeated cold welding, fracturing and rewelding of the milled powder. The optimum of this process can be achieved when the fracturing and the welding phenomena are balanced (El-eskandarany, 2001).

Every time that two grinding balls collide some powder particles are trapped in the collision. The impact forces plastically deform the powder particles determining their morphological evolution and the changes in the particle size (Fig. 2).
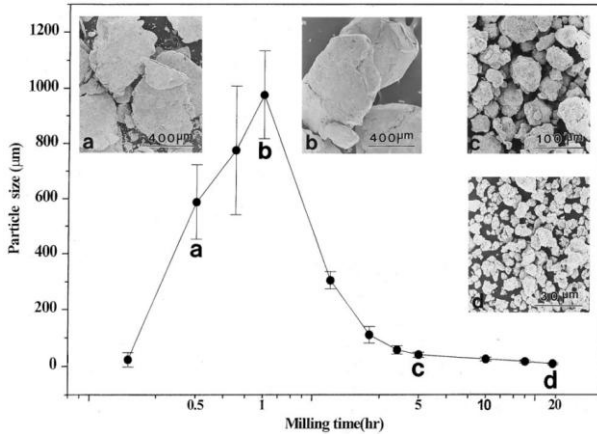
Figure III – 2. Morphological and dimensional evolution of the powder particles as a function of milling time (Suryanarayana, 2001).

In the early steps the impact forces cause the flattening and work hardening of the ductile metal particles. The flatten particles overlap and are brought into intimate contact, forming layered structure of composite particles (El-eskandarany, 2001). At the beginning of the process the metal particles are soft and ductile therefore their tendency to cold weld is high. At this stage the particle size increases, even becoming three times bigger than the starting powder (Suryanarayana, 2001). The particle morphology shows a considerable change, particles become flat and elongated instead of round as most of the row powders (Bailon-Poujol et al., 2011; Maurice et al., 1994).

For longer milling time these layered aggregates are continuously deformed and work hardened so that their microstructure is further refined. The increase of particle hardness due to the work hardening leads to fracturing of these agglomerates resulting in the decrease of the particle size. At this point fracturing predominates over cold welding, particle size keeps decreasing and the milled powder shape becomes round again (El-eskandarany, 2001; Maurice et al., 1994; Suryanarayana, 2001).

When particles become very small they may tend to aggregate again. The system then reaches a steady-state equilibrium, in which the rates of welding and of fracturing are balanced. At the equilibrium, the mean particle size and particle hardness remain constant and the size distribution is quite narrow because bigger particles are fragmented at the same rate at which smaller particles aggregate (Maurice et al., 1994; Suryanarayana, 2001).

This analysis of the particle size evolution highlights that fracturing has to be promoted to achieve a fine reduction of the particle size. PCA can modify the particle surfaces inhibiting the metal-to-metal contact necessary for cold welding thus

enhancing fragmentation (El-eskandarany, 2001). Another way to promote fracturing is cooling the mill chamber. This changes the deformation behaviour of the powder which is not able anymore to deform to the large compressive strains and prefers to fracture (El-eskandarany, 2001). The presence of a brittle component in the starting powder also accelerates the fragmentation phenomenon. In this case the milling stages are the same as those described previously but they all occur for shorter milling times (Bailon-Poujol et al., 2011). The brittle phase is not able to store plastic deformation and breaks easily. This favours the fragmentation and inhibits the first stage of milling where cold welding predominates. Therefore the reduction of particle size starts sooner and higher is the amount of brittle phase, shorter is the milling time required to achieve the steady-state.

Beside the particle size and shape changes, MM also deeply modifies the microstructure of the powder. This modification depends on the starting powder deformation behaviour, so that three categories can be distinguished: ductile-ductile system, ductile-brittle system and brittle-brittle system.

The MA of ductile-ductile components is the ideal system. The true alloying process requires an intimate contact between the powders which can be achieved only by the repeated action of cold welding. This process forms a composite lamellar structure (Benjamin et al., 1974). Increasing milling time these elemental lamellae become convoluted and thinner. For a metal-metal system, the reduction of the interlamellar spacing results in decreasing the diffusion distances and this together with the increased lattice defect density and any heating occurring during milling activates the true alloying process forming solid solutions. The lamellar structure becomes finer and even disappears for long milling time (Suryanarayana, 2001).

In the initial stage of MA of ductile-brittle systems the collisions flattens the metal powder and fragments the brittle component. These brittle fragments are entrapped by the ductile deformed particles and so they are arranged along the interlamellar spacing, as schematically shown for oxide dispersion strengthen alloys (Fig. 3-a). Further milling twists and refine the lamellae decreasing the interlamellar spacing and uniformly dispersing the brittle fragments (Fig. 3b) (Suryanarayana, 2001). If the brittle phase is soluble, true alloying occurs for longer milling time. In this case the achievement of chemical homogeneity depends also on the solid solubility of the brittle phase in the ductile matrix.

In the case of MA of brittle-brittle systems the lack of a ductile component preclude the welding phenomenon. Brittle components get fragmented until they reach a minimum size, called "limit of comminution". Even though cold welding does not take place, it has been observed that the fragments of the harder component get embedded in the softer component (Suryanarayana, 2001).
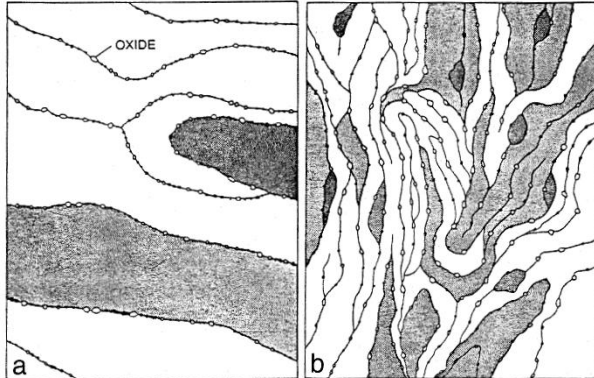
Figure III – 3. Scheme of the microstructural evolution during MA for oxide dispersion strengthened alloys (adapted from Suryanarayana, 2001).

Regardless of the ductile or brittle behaviour of the components, MM and MA always bring a microstructure refinement. It has been reported that crystallite size changes during milling (Dai et al., 2012; Fecht, 1995; Huang et al., 1996). Generally speaking crystallite size is strongly reduced in the early stage of MM due to the intense collisions. Further milling continuously refines the crystallite size but at a lower rate.

In some systems MM can also lead to the formation of new phases. This is the case for example of austenitic steels, in which the strain induced austenite to martensite transformation can occur (Huang et al., 1996).

3.2.2   Case of study: mechanical milling of AISI H13

Before considering the production of MMCs, MM of a HWTS (grade AISI H13) has been investigated (Fedrizzi et al., 2012[3]). This study has been focused on the influence of milling time on the morphological and microstructural evolution of milled powders. Figure 4 shows effect of the milling time on particle morphology. Atomized spherical powder (Fig. 4a) is flattened and elongated in the early stage of milling (Fig. 4b). For longer milling time the particle morphology becomes round again (Fig. 4c,d).
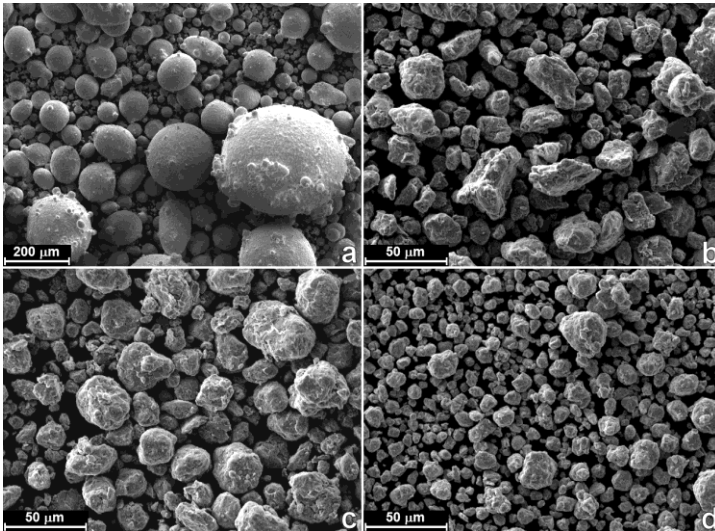
Figure III – 4. SEM micrographs of the morphology of the atomized AISI H13 powder (a) and of the milled AISI H13 for 200 min (b), 400 min (c) and 2000 min (d) (Fedrizzi et al., 2012[3]).

From Figure 4 it is also possible to see the strong particle size reduction produced by MM. The mean particle size as a function of the milling time is shown in Figure 5a. The particle size is quickly reduced to 30 µm in the early stage of MM and then continuously decreases but at a lower rate. Together with the particle size reduction, MM produces also a microstructural refinement (Fig. 5b). As well as for the particle size, the crystallite size shows a sharp reduction in the early stage of MM followed by a low rate decrease for longer milling time. This behaviour is in good agreement with literature data (Dai et al., 2012; Fecht, 1995; Huang et al., 1996).
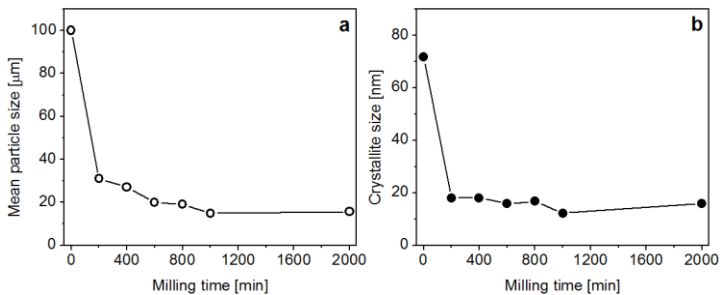
Figure III – 5. Mean particle size (a) and crystallite size (b) as a function of milling time (adapted from Fedrizzi et al., 2012[3]).

Microstructural investigation shows that the solidification structure of the AISI H13 (Fig. 6a) is being progressively deformed during MM. The dendritic structure is stretched and aligned forming a lamellar structure (Fig. 6b). Further milling reduces the size of lamellae and the microstructure becomes more and more homogeneous until the lamellar structure completely disappears (Fig. 6d).
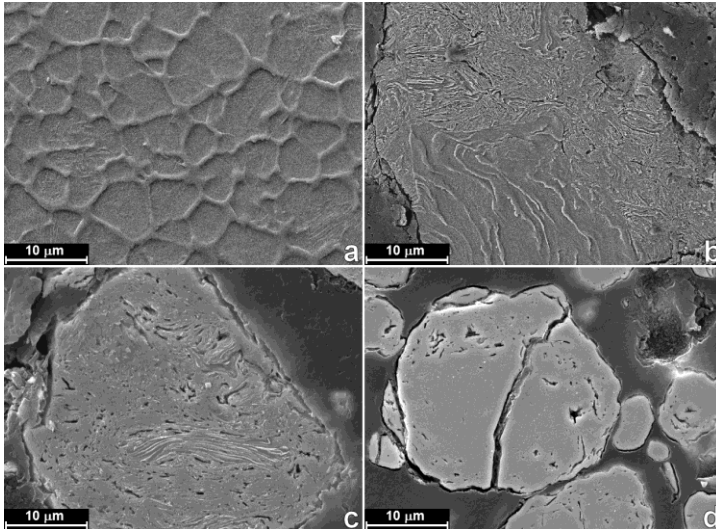
Figure III – 6. SEM micrographs of the microstructure of the atomized AISI H13 powder (a) and of the milled AISI H13 for 200 min (b), 400 min (c) and 2000 min (d) (Fedrizzi et al, 2012[3]).

This investigation has pointed out that for this milling conditions the system achieve the steady state at about 1000 min. Longer milling time does not significantly improve the powder features and therefore carry on long MM it is not worthwhile.

3.3   Consolidation by SPS

Tool steels by PM are mainly produced by HIP (Grinder, 1999). In mass production this process has still the leading role but new technologies, such as metal injection moulding, hot extrusion sintering, are becoming quite attractive for the production of advanced materials (El-eskandarany, 2001).

It has been demonstrated that electric current can be applied to enhance sintering and therefore to shorten the processing route (Munir et al., 2006). In the 60s in Japan a sintering process based on pulse current was researched and in the 80s-90s some small experimental Plasma Activated Sintering systems were produced. Later research developed the third generation of SPS systems and this advanced technology has gained more and more attention among the materials

researchers as well as in the production industry (Tokita, 1993). The main features which make SPS so attractive are the very high thermal efficiency, the uniform heating and the powder particle surface purification and activation occurring due to the current pulse (Tokita, 1993).

SPS is a pressure sintering in which DC pulsed current is applied. Due to the Joule effect the current directly heats the graphite mould and the stacked powder at a very high heating rate. Compared to HIP, SPS offers a finer control of the sintering energy, high production rate, high reliability (Tokita, 1993).

The SPS unit (Fig. 7) is formed by a uniaxial vertical press and a vacuum chamber. A water cooling system controls the chamber and punches temperature. The punches are conductive, usually graphite made, and they are connected to the DC current generator so to work also as electrodes.
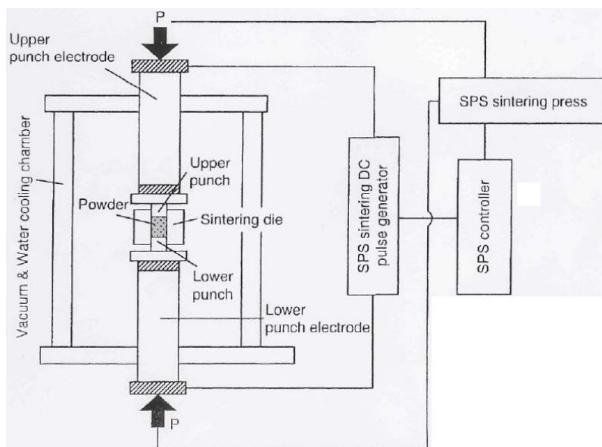
Figure III – 7. Schematic representation of SPS configuration (adapted from Tokita, 1993).

Beside Joule heating the ON-OFF pulses of DC current applied in SPS are believe to generate spark plasma, spark impact pressure and an electric field diffusion (Tokita, 1993). However the physical phenomena taking place during SPS have not been fully understood yet. Hulbert et al. (Hulbert et al., 2009) experimentally proved the absence of plasma at any time of the process for many configurations. In any case the direct heating by electric current allows fast heating rate and the production of innovative materials, some of which cannot be prepared without SPS (Omori, 2000). For example, SPS can break the stable oxide layer covering aluminium particles. Diffusion of aluminium occurs through these small holes in the oxide allowing the formation of metallurgical bonds and consolidation. Moreover it has been proved that very high temperature can be reached at the contact points leading to localized melting and enhancing the interparticle bonding

(Diouf et al., 2012; Song et al., 2006). All these features and the plastic deformation due to the applied pressure allow the production of fully dense high quality materials working at lower temperature and in a shorter time than conventional sintering processes (Tokita, 1993). Li et al. (2006) pointed out the beneficial effect of the pulsed current on the formation of neck in the initial stage of sintering.

3.3.1   Densification mechanisms

The sintering mechanism occurring during SPS have been described by Zhaohui et al. (2008) who have proposed a sequence of four stages: i) activation and refining of the powder; ii) formation of the sintering neck; iii) growth of the sintering neck and iv) plastic deformation. Due to the oxide breakage and the fast heating up of the surfaces, the spark discharges mainly activate the first two stages. The other two steps play the main role in densification and they are promoted by the heating due to Joule effect and by the applied pressure. These two mechanisms are quite similar to those acting in classic pressure sintering (like HIP) therefore constitutive models for densification in SPS (Olevsky et al., 2006) are generally based on those developed for HIP (Artz et al., 1983; Helle et al., 1985). These analyses pointed out four main densification mechanisms described in the following. In the early stage, when relative density is lower than 90%, the densification by rate-independent plasticity plays the main role. This mechanism is related to the plastic deformation of the contact areas, it needs a local pressure higher than the yield stress to be activated and it ends when the contact areas are big enough that the acting pressure is lower than the yield stress. The second mechanism is the densification by power-law creep and it is related to the deformation of the contact areas at high temperature under constant load. Another mechanism is the densification by diffusion. It is based on either grain boundary and bulk diffusion. This mechanism is strongly influenced by the particle size and generally speaking diffusion increases as particle size decreases. The last mechanism is the densification by Nabarro-Herring and Coble creep which acts only when the grain size is much smaller than the particle size. This mechanism accelerates densification even when the applied pressure is low.

Experimental studies indicate that in SPS electric current directly contributes to the diffusion mass transport leading to densification (Munir et al., 2006). Olevsky et al. (2006) developed a constitutive model for SPS densification kinetics. They considered two major components of mass transfer leading to densification: the grain boundary diffusion and the power-law creep. Beside the applied load these two phenomena are activated by the sintering stress, or surface tension, and stady-state electromigration due to the electric field contribution to diffusion (Olevsky et al., 2006). Creep due to applied load has the main role in densification when porosity is higher than 30%. Otherwise the leading phenomena depends on the grain size. For

conventional micron-size materials (grain size around 40 µm) the applied load still plays the dominant role in material transport. In the case of ultrafine powders (grain size smaller than 1 µm) the electromigration is the principal phenomenon promoting densification, even if for the final collapse of void externally applied load may be required. Finally for nano-powders (having grain size of 100 nm) the main contribution to sintering comes from the surface tension.

It has been demonstrated that by SPS full density can be achieved sintering at lower temperature and in shorter time (Mamedov, 2002). Hence, SPS is considered to be suitable for the fabrication of the nanocrystalline metals and ultrafine-grained metals (Zhaohui et al., 2008).

Chapter IV

Materials and Experimental Procedures

4.1   Hybrid Tool Steels

4.1.1   Materials

For the production of hybrid tool steel a HWTS (grade AISI H13) and a HSS (grade AISI M3:2) powders were selected. Their composition is given in Table 1.

Table IV – 1. Nominal composition of the alloying elements in the steel powders [weight %].

Material	C	W	Mo	Cr	V	Mn	Si	N*	O*
AISI H13	0.41	-	1.6	5.1	1.1	0.35	0.90	383	105
AISI M3:2	1.28	6.4	5.0	4.2	3.1			559	163

* composition in ppm.

Both powders were produced by nitrogen atomization and they present spherical morphology with many satellites around the surface of the bigger particles (Fig. 1). Their particle size distribution is quite wide, with more than 5% of particles having size bigger than 355 μm and the mean particle size about 100 μm (Fig. 2).
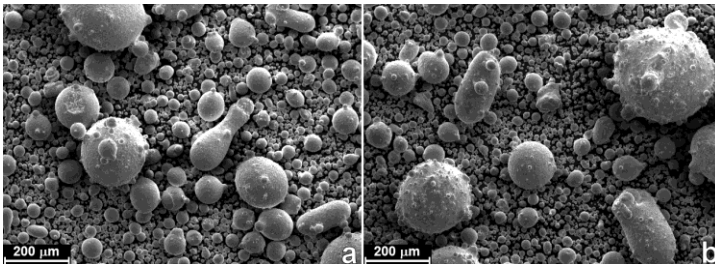

Figure IV – 1. SEM micrographs of the AISI H13 (a) and AISI M3:2 (b) powders.
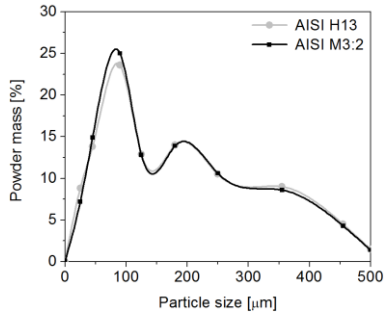
Figure IV – 2. Particle size distribution of the AISI H13 and AISI M3:2 powders.

The microstructure of both steels is constituted by primary martensite dendrites surrounded by microsegregated regions resulting from the solidification of the last liquid phase richer in alloying elements (Fig. 3). Due to the relatively high amount of carbon and alloying elements retained austenite is detected by X-rays diffraction (XRD) analysis in both steels (Fig. 4). The higher content of alloying elements in AISI M3:2 is responsible for the higher content of retained austenite and for the precipitation of some primary carbides (Fig. 4b).
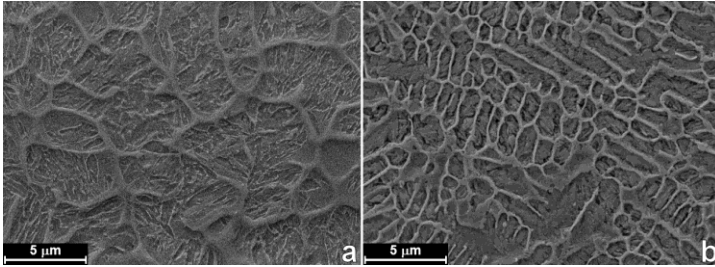
Figure IV – 3. SEM micrographs of the microstructure of the AISI H13 (a) and AISI M3:2 (b) powders.
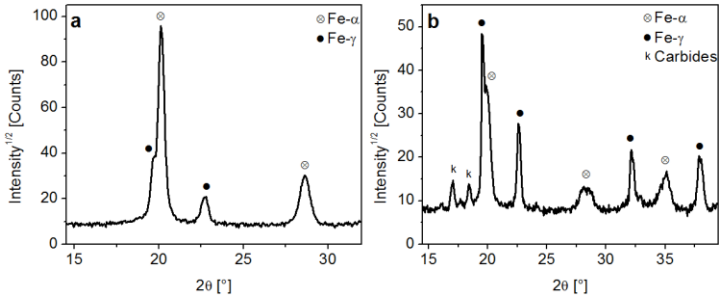
Figure IV – 4. XRD patterns for the AISI H13 (a) and AISI M3:2 (b) powders.

4.1.1.1 Influence of the particle size ratio

For the analysis of the influence of the PSR both powders were sieved in three groups having particle size range 0-45 µm, 45-125 µm and 125-250 µm, respectively. Fixing the composition to 80% H13 – 20% M3:2 (vol %), the sieved powders were dry mixed in a "Turbula©" mixer for 20 minutes so to produce nine blends with different PSR, defined as the ratio between the mean particle size of AISI H13 (d_{H13}) and AISI M3:2 ($d_{M3:2}$) (Tab. 2). The sample codes identify the composition (80%vol of AISI H13) and the powder size, so that the main number indicates the maximum size of AISI H13 powder while the small subscript number indicates the maximum size of AISI M3:2 powder. In the following paragraphs the name "80H13 blends" is used to generally refer to these samples.

Table IV – 2. Composition and codes of the 80H13 blends.

Sample code	H13 particle size [µm]	M3:2 particle size [µm]	PSR ($d_{H13}/d_{M3:2}$) [µm]
80H13-250$_{250}$	125-250	125-250	1.00
80H13-250$_{125}$	125-250	45-125	2.21
80H13-250$_{45}$	125-250	0-45	6.47
80H13-125$_{250}$	45-125	125-250	0.45
80H13-125$_{125}$	45-125	45-125	1.01
80H13-125$_{45}$	45-125	0-45	2.95
80H13-45$_{250}$	0-45	125-250	0.15
80H13-45$_{125}$	0-45	45-125	0.32
80H13-45$_{45}$	0-45	0-45	0.95

4.1.1.2 Influence of the composition

Previous study (Pellizzari et al., 2011[2]) investigating the influence of the composition on the properties of a hybrid tool steel highlighted a negative interference between the two steels during sintering. The achievement of high density is obstructed by their different densification kinetic, resulting in decreased material properties. Larger particle size distribution amplifies this negative effect. In this work MM has been considered to refine the powder particle size in order to reduce this interference.

MM was conducted in a Fritsch Pulverisette 6 planetary mono mill at 450 rpm in vacuum atmosphere. Spheres with 10 mm diameter of 100Cr6 (63HRC) and a BPR of 10:1 were used. To avoid overheating cycles of 2 min on + 9 min off were used for a total milling time of 1000 minutes. As PCA 0.2%wt Kenolube was added to the starting powder. It has been demonstrated that these parameters optimize the refinement of both grain size and particle size in AISI H13 (Fedrizzi et al., 2012[3]).

The milled powders were dry mixed in a "Turbula©" mixer for 20 minutes so to produce four blends with different composition (Tab. 3). Two reference samples were produced using the base milled powders. All these six materials are generally called "MM-samples" in the following paragraphs.

Table IV – 3. Composition and codes of the MM-samples.

| Sample code	Composition [volume fraction]	
	AISI H13	AISI M3:2
MM-H13	1.0	0.0
MM-80H13	0.8	0.2
MM-60H13	0.6	0.4
MM-40H13	0.4	0.6
MM-20H13	0.2	0.8
MM-M3:2	0.0	1.0

4.2 HWTS Based MMCs

4.2.1 Materials

For the MMC matrix the same HWTS powder (grade AISI H13) selected for the production of the hybrid tool steel was used. Its composition is given in Table 1 and its main characteristics are discussed in paragraph 4.1.1. As reinforcement three different compounds were chosen, namely titanium diboride (TiB_2), titanium carbide (TiC) and titanium nitride (TiN). Their composition is listed in Table 4. These compounds have been proved to be suitable reinforcement for steel matrix (Akhtar, 2008; Du et al., 2008; Liu et al., 2001; Ma et al., 2012; Oliveira et al., 1999; Pagounis et al., 1998; Tjong et al., 1999[2]). They are all characterized by high hardness, i.e. 29.4 GPa, 28 GPa and 18-22 GPa for TiB_2, TiC and TiN, respectively (Du et al., 2008; Ma et al., 2012).

Table IV – 4. Nominal composition of the TiB_2, TiC and TiN powders [weight %].

Material	C	O	N	Fe	B	Ti
TiB_2	0.03	0.4	0.15	0.025	33.2	balance
TiC	19.2	0.5	0.1	0.044	-	balance
TiN	0.02	0.4	22.1	0.163	-	balance

The three powders show different particle size and morphology (Fig. 5). The TiB_2 particles mainly show a hexagonal prism shape and they are quite big: 90%wt of the particles are smaller than 31.21 μm and their mean diameter is 11.99μm. TiC and TiN powders are finer and more irregular and their mean particle size is 1.3μm and 3.6μm, respectively.
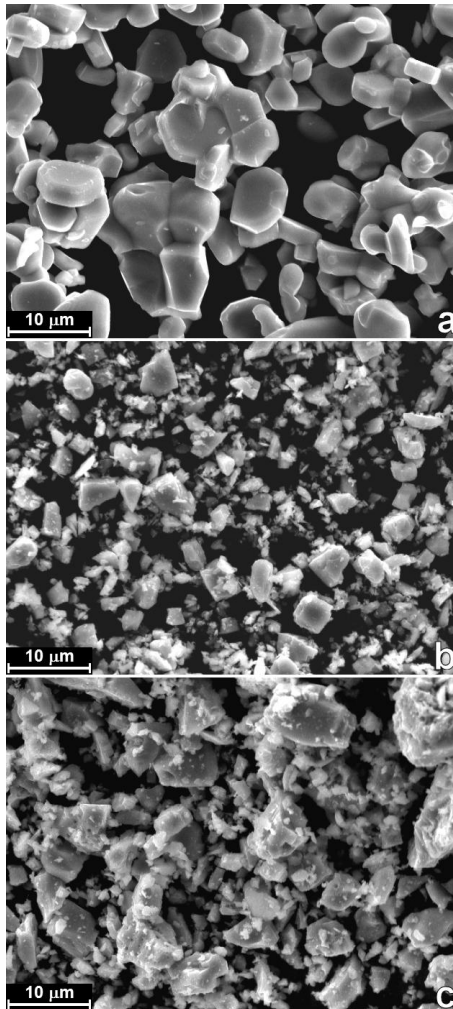
Figure IV – 5. SEM micrographs of the TiB$_2$ (a), TiC (b) and TiN (c) powders.

4.2.1.1   *Influence of the processing route*

For the fabrication of HWTS based MMCs two different routes were considered: powder mixing and MA. In this study of the influence of the processing route only the TiB$_2$ powder was considered as reinforcement and its content was fixed to 20%vol.

The particle size distribution of the atomized AISI H13 (Fig. 2) is much wider than that of TiB$_2$ and this results in a high PSR, defined as the ratio between the

mean particle size of AISI H13 (d_{H13}) and TiB_2 (d_{TiB2}). Therefore for the powder mixing process the AISI H13 powder was previously milled in order to refine its particle size and reduce the PSR. For purpose of comparison, a steel sample was produced using this milled AISI H13 powder.

The complete list of materials investigated in this stage is reported in Table 5.

Table IV – 5. Powder production steps and codes of the investigated materials.

Sample code	Description
sMM-H13	soft mechanically milled AISI H13
sMM-H13+20TiB$_2$	mechanically milled AISI H13 then dry mixed with 20%vol of TiB$_2$
MA(H13+20TiB$_2$)	as-atomized AISI H13 dry mixed with 20%vol TiB$_2$ powder and then mechanically alloyed

All the mixing stages were carried out in a "Turbula©" mixer for 20 minutes. The milling steps were conducted in a Fritsch Pulverisette 6 planetary mono mill at 450 rpm in vacuum atmosphere. To avoid overheating cycles of 2 min on + 9 min off were used for a total milling time of 200 minutes. Spheres in 100Cr6 (63 HRC) with 10 mm diameter were used to obtain a BPR of 10:1.5 and 0.2%wt Kenolube was added as PCA.

4.2.1.2   Influence of the reinforcing particles

From the analysis of the processing route, MA has resulted to be the most suited process for the production of these MMCs. Therefore all the materials investigated in this part of the thesis were produced according to the procedure previously described for the MA(H13+20TiB$_2$) sample (Tab. 5).

Fixing the amount of HPs to 20%vol, MMC powders with different kind of reinforcement were produced by MA. These powders and their corresponding sintered samples are generally named "MA-powders" and "MA-samples", respectively. Their names, which are listed in Table 6, identify both the kind and amount of reinforcement.

Table IV – 6. Composition and codes of the MA-powders.

Powder code	Reinforcement amount [vol%]	Reinforcement kind
MA(H13+20TiB$_2$)	20	TiB$_2$
MA(H13+20TiC)	20	TiC
MA(H13+20TiC)	20	TiN

4.3 Spark Plasma Sintering

All samples investigated in this PhD thesis were sintered in a DR.SINTER® SPS1050 (Sumitomo Coal & Mining, now SPS Syntex Inc.) apparatus with graphite punches and dies. All sample have cylindrical geometry with 5 mm height but diameter was set to 30 mm for samples described in paragraph 4.1 (hybrid tool steels) and to 20 mm for those described in paragraph 4.2 (HWTS based MMCs). Sintering was performed heating up to 1100 °C and the sintering rate was set to 50 °C/min for the 30 mm diameter samples and to 100 °C/min for the 20 mm ones. The holding time was set to 1 minute for all the MM-powders (MM-samples and all HWTS based MMCs) and to 5 minutes for the 80H13 blends. Final free cooling was performed after the isothermal soaking. Selecting the MA(H13+20TiC) and MA(H13+20TiN) powders a second round of samples was produced changing the holding time from 5 to 30 min. These samples are named with their powder code followed by a hyphen and the corresponding holding time (i.e. MA(H13+20TiC)-5min). Once the temperature reached 600 °C, to obtain a pressure of 60 MPa, a compressive load of 42 kN and 19 kN was applied to the 30 mm and 20 mm diameter samples, respectively. These conditions have been previously demonstrated to be the most suitable for sintering present steels (Pellizzari et al., 2011[1]). The displacement of the lower punch was monitored during sintering and used to follow material densification. The temperature was recorded by an optical pyrometer focused on the external wall of the graphite die.

All 80H13 blends and MM-samples were vacuum heat treated in a low pressure furnace. The austenization temperature was set to 1050 °C for 15 min and it was followed by 5 bar nitrogen quenching and then double tempering at 625 °C for 2 h each.

4.4 Material characterization

4.4.1 Particle size distribution

The powders particle size distribution was measured in a "Partica LA-950©" Laser Diffraction/Scattering Particle Size Distribution Analyzer at the Department of Chemistry, Physics and Environment, University of Udine (Italy). The measurement is based on light scattering phenomena and the system can detect a wide range of particle size, from 10 nm up to 3 mm.

4.4.2 X-ray diffraction

For both powders and sintered samples, XRD patterns were collected using a Mo kα (λ = 0.7093 nm) source. The experimental data were elaborated with the

Rietveld method (Rietveld, 1969) using the MAUD software (Materials Analysis Using Diffraction) (Lutterotti, 1997).

In this work XRD was used to determine the crystallite size and lattice strain of the MA-powders and the composition by quantitative analyses of both MA-powders and MA-samples. The formers were evaluated using the X-ray peak broadening techniques. Three factors determine the peaks broadening: the instrument, the crystallite size and the lattice strain (Lutterotti, 1997). After proper corrections taking into account the instrumental effect, crystallite size and lattice strain can be calculate applying the Scherrer formula (1),

$$B = (0.9 \ \lambda) / (d \ cos\theta) + \eta \ tan\theta \qquad (1)$$

where B is the peak width at half height, λ is the radiation wavelength, d is the crystallite size, η is the lattice strain and θ is the Bragg angle. The equation can be rewritten as follows:

$$B \ cos\theta = (0.9 \ \lambda) / d + \eta \ sin\theta \qquad (2)$$

This equation represents a straight line, where the lattice strain η is the slope and the intercept is $0.9\lambda/d$. This method is quite accurate for measuring crystallite size in the range of 10-100 nm (Suryanarayana, 2001).

The quantitative analysis, based on the Rietveld method, considers the area under the peak proportional to the volumetric fraction of the corresponding phase. MAUD fits the experimental data with the following relation:

$$= I \ f_j / V_j^2 \ L_k \ |F_{k,j}|^2 \ P_{k,j} \ A_j \qquad (3)$$

where   is the intensity of the k peak related to the j phase, I is the incident radiation intensity, f_j is the volumetric fraction of the j phase, V_j is the cell volume of the j phase, L_k is the Lorentz polarization for the k peak, $F_{k,j}$ and $P_{k,j}$ are structure factors and A_j is the absorption factor (Lutterotti, 1997).

4.4.3   Density

The density of the sintered samples was measured applying the Archimedes' principle, according to ASTM B962-08 standard.

For the determination of relative densities of composite materials, their theoretical absolute density was calculated according to the linear rule of mixture (4),

$$\rho_{composite} = v_i \cdot \rho_i + v_{ii} \cdot \rho_{ii} \qquad (4)$$

where v is the volume fraction and ρ is the absolute density of each component.

For the 80H13 blends the theoretical absolute density was calculated equal to 7.82 g/cm^3, assuming 7.76 g/cm^3 as the absolute density of AISI H13 and 8.05 g/cm^3 as the AISI M3:2 one.

For the MM-samples the theoretical absolute densities was calculated considering the absolute density of the two MM-steels measured by a pycnometer (ρ_{MM-H13} = 7.71g/cm^3, $\rho_{MM-M3:2}$ = 7.97g/cm^3).

In the case of HWTS based MMCs, literature data 7.76 g/cm^3, 4.38 g/cm^3, 4.94 g/cm^3 and 5.21 g/cm^3 were considered as the absolute densities of AISI H13, TiB$_2$, TiC and TiN, respectively.

4.4.4 Metallography

A metallographic cross section of the sintered sample was obtained by precision microcutting with diamond blade. Standard metallographic preparation, including grinding with SiC papers up to 1200 grit and final polishing with 3 μm and 1 μm diamond paste and chemical etching with Nital etchant (5% nitric acid in ethanol solution) was carried out for both sintered materials and powders.

Microstructures as well as powder morphologies were investigated by Scanning Electron Microscopy (SEM) and semi-qualitative chemical analysis was carried out by energy-dispersive X-ray spectroscopy (EDXS).

A Veeco Multimode Nanoscope IIIa Atomic Force Microscope (AFM) at the Department of Chemistry, Physics and Environment, University of Udine (Italy) was used to map the sMM-H13+20TiB$_2$ sintered sample surface. Topographic and surface Volta potential maps were obtained simultaneously using tapping and Scanning Kelvin Probe Force Microscopy (SKPFM)-interleave mode configuration on marked 25×25 μm^2 areas. SKPFM measures the local Volta potential giving information about the differences in the potential between the different particles and phases present on the sample investigated surface. The same areas were observed by SEM to provide a clear overview of the particle dimension and distribution inside the metal matrix. EDXS was used in order to obtain a semi-quantitative compositional analysis of the different phases.

4.4.5 Hardness and microhardness

Hardness of sintered materials was measured by Vickers method, according to ASTM E92-82. The applied load was set to 10 kg and reported results are the average of six measurements.

Microhardness was measured on both the sintered MA-samples and the MA-powders. Microhardness test was performed on the metallographic samples with a Vickers Paar MHT-4 micro-indenter. The applied load was set to 0.5 N for the sintered materials while it was reduced to 0.1 N for the powders in order to eliminate the influence of the substrate.

4.4.6   Fracture toughness

For the hybrid tool steels (80H13 blends and MM-samples) the apparent fracture toughness (K_a) was evaluated following the procedure proposed for small fracture toughness specimen (Lee et al., 2002). Notch depth (a) with root radii (ρ) of 50 µm were electro discharge machined in 6×3×30 mm^3 (W × B × L) specimens. The ratio of notch depth to the specimen width (a/W) was set at 0.5. Static fracture toughness testing was performed using a 10 ton capacity universal tester (Instron). The specimens were loaded in three-point bending at a crosshead speed of 0.5 mm/min, according to the ASTM E399. The decrease in stress triaxiality with increasing ρ causes a decrease in the stress that would initiate fracture, so that the K_a value is higher than that of K_{IC} measured on a fatigue precracked sample.

Chapter V

Hybrid Tool Steels

5.1 Influence of the Particle Size Ratio

Densification behaviour of soft/hard powder mixture was deeply investigated by Bouvard (2000). This analysis is based on the hypothesis that ceramic HPs are not deformable under the applied pressure while metal soft particles can be plastically deformed and their deformation is accountable for the material densification. The powders used in this work are a hot work tool steel and a high speed steel thus it is not possible to define a totally hard component and a totally soft one. In any case these two steels present different hot strength (Imbert et al., 1984; Rodenburg et al., 2004) and it is thus plausible to identify a harder material and a softer material. The differences in alloying contents between AISI H13 and AISI M3:2 (Tab. IV-1) produce a higher carbides volume fraction in the HSS AISI M3:2 microstructure (Fig. 1). Close to equilibrium condition, a conventional AISI M3:2 contains primary carbides such as M_6C type (tungsten or molybdenum carbides) and MC (vanadium carbides) (Fig. 1b) which are quite hard and do not dissolve at high temperature resulting in the high strength of this steel. In contrast in AISI H13 the major fraction of carbides consists of pro-eutectoid MC types (Fig. 1a), but in a lower amount and size than in AISI M3:2. These differences in the microstructure are

34

responsible for the different strength of the two steels. As shown in Figure 2, AISI M3:2 is always characterized by a higher flow stress compared to that of AISI H13 in the same working conditions (temperature and strain rate).
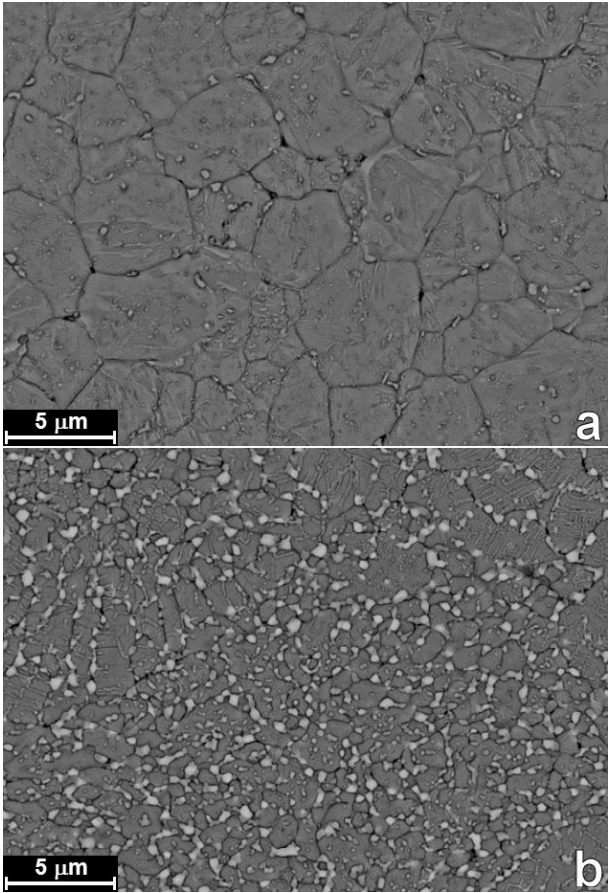
Figure V – 1. SEM micrographs of the microstructure of AISI H13 (a) and AISI M3:2 (b) after sintering.
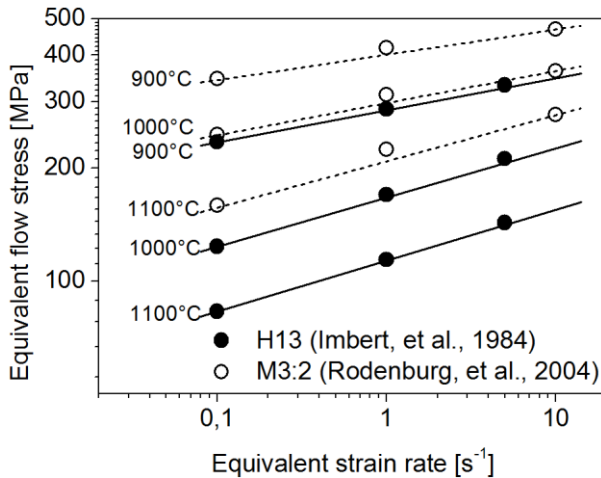
Figure V – 2. Flow stress as a function of strain rate and temperature for AISI H13 and AISI M3:2 (adapted from Fedrizzi et al., 2012[1]).

The powder microstructure (Fig. IV-3) is not the one at the equilibrium and therefore XRD analysis (Fig. IV-4) has highlighted that residual austenite is present in both powders and carbides has not precipitated in the AISI H13 powder while only a small amount of them has formed in the AISI M3:2 powder. DSC measurements on the powders highlight the presence of a exothermal signal starting around 490-500 °C and showing the maximum at 616 °C and 657 °C for AISI H13 and AISI M3:2, respectively (Fig. 3). These peaks can be related to the precipitation of carbides and therefore it can be assumed that during the heating stage of sintering, carbides precipitates in both materials before the maximum pressure is reached (700 °C). This means that during the sintering cycle, when pressure is applied, both steels microstructure is closer to the equilibrium one. Therefore experimental data in Figure 2 can be assumed to be relevant for the behaviour of present steels when pressure is applied. It can be concluded that at the sintering temperature (1100 °C) AISI H13 deforms more easily than M3:2 so that they can be considered as the "softer" and "harder" component, respectively, for the study of the densification mechanisms. Microstructural observations of the sintered blends confirm this assumption. As shown in Figure 4 AISI H13 particles are strongly deformed by the applied pressure. This deformation allows AISI H13 to fill all the pores around AISI M3:2 powders (black arrows). On the other hand, due to their higher resistance to plastic deformation AISI M3:2 particles are mainly not-deformed or slightly deformed on the surface (white arrows in Fig. 4).
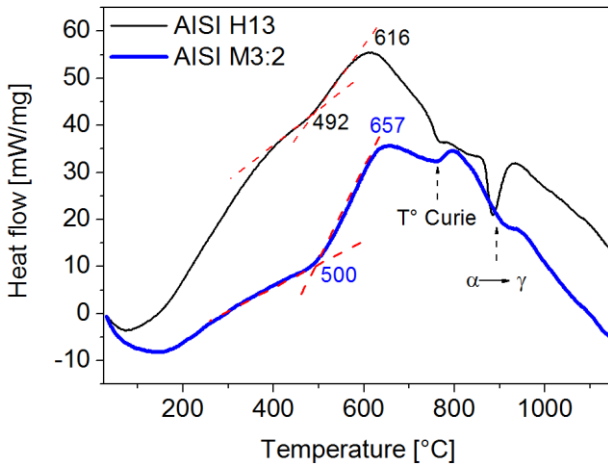
**Figure V – 3.** DSC curves for AISI H13 and AISI M3:2 powders.
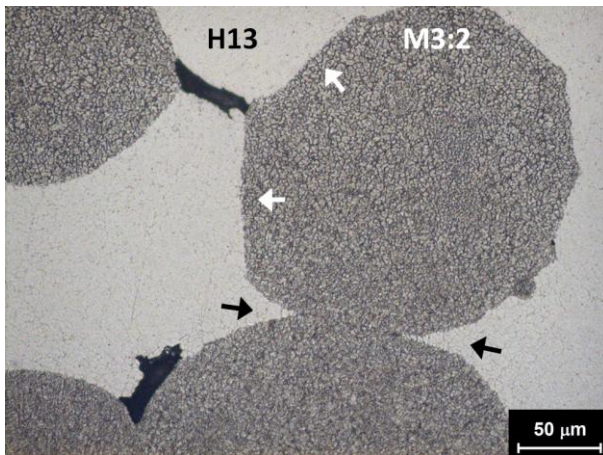
Figure V – 4. Optical micrograph of sample 80H13-250$_{250}$ in which light areas are AISI H13 and grey areas are AISI M3:2. Black arrows highlight AISI H13 heavy deformation and white arrow indicates small deformation of an AISI M3:2 particle.

The microstructure of the nine 80H13 blends has been investigated by optical microscope (Fig. 5). Even if the composition is the same for all materials, i.e. 80%vol of AISI H13, it is possible to see that the two components present different arrangements according to the PSR (d$_{H13}$/d$_{M3:2}$). As shown in Figure II-4 and as described by Bouvard (2000), for a fixed composition the HP distribution is ruled by the PSR. The three blends with PSR lower than 0.5 (i.e. samples 80H13-125$_{250}$, 80H13-45$_{250}$ and 80H13-45$_{125}$) represent the case of "isolated HPs" characterized by

a good dispersion of AISI M3:2 particles (Fig. 5d,g,h). In the three blends with PSR close to 1 (i.e. samples 80H13-250$_{250}$, 80H13-125$_{125}$ and 80H13-45$_{45}$) AISI M3:2 particles are still mainly dispersed but aggregates start to form (Fig. 5a,e,i) meaning that these blends fall into the "aggregation" field (Fig. II-4). Finally the three blends with PSR higher than 2 (samples 80H13-250$_{125}$, 80H13-250$_{45}$ and 80H13-125$_{45}$) show a net-like distribution of AIS M3:2 particles which form a nearly continuous skeleton (Fig. 5b,c,f). These microstructures are relevant to the percolative structure. The model of Bouvard (2000) predicts that for 20% volume fraction of HPs percolation occurs when PSR is higher than 1.95. Figure 6 shows the percolation threshold as a function of the PSR and the HP volume fraction. Present 80H13 blends data are also plotted and it is possible to see the good agreement between the 80H13 blends microstructures (Fig. 5) and the analysis of Bouvard (2000). It can be deduced that AISI H13/AISI M3:2 composites follow the typical densification behaviour of the soft/hard blends even if both their components present a visco-plastic deformation behaviour.
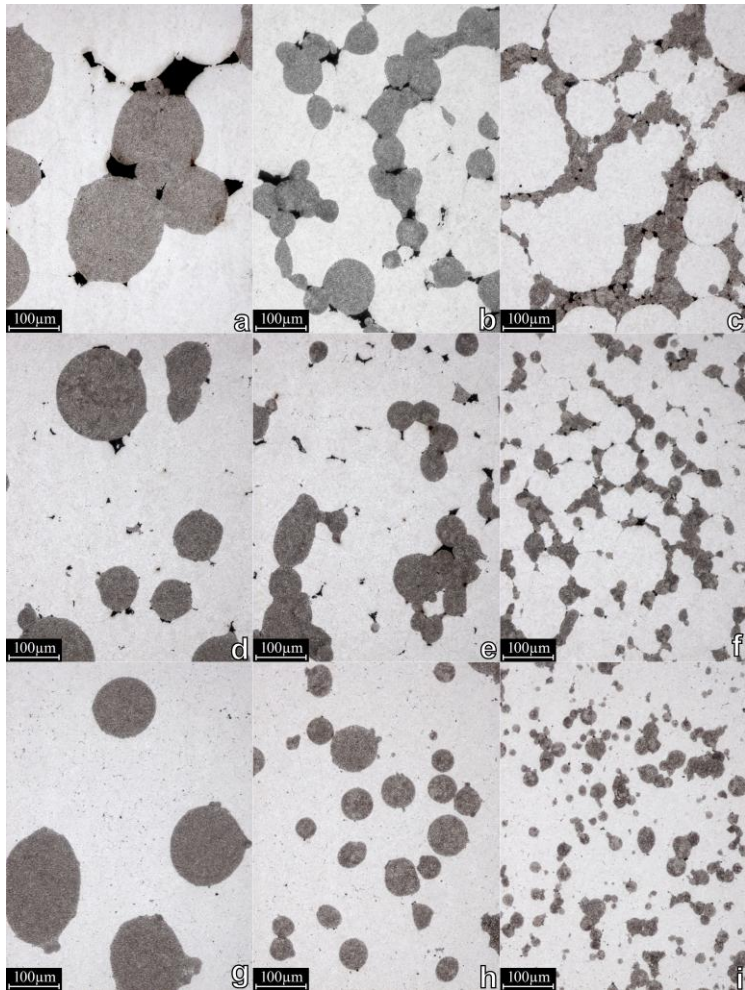
Figure V – 5. Optical micrographs after chemical etching of the samples 80H13-250$_{250}$ (a), 80H13-250$_{125}$ (b), 80H13-250$_{45}$ (c), 80H13-125$_{250}$ (d), 80H13-125$_{125}$ (e), 80H13-125$_{45}$ (f), 80H13-45$_{250}$ (g), 80H13-45$_{125}$ (h) and 80H13-45$_{45}$ (i). Light areas are AISI H13, dark grey areas are AISI M3:2 and black areas are pores (adapted from Fedrizzi et al., 2012 [1]).
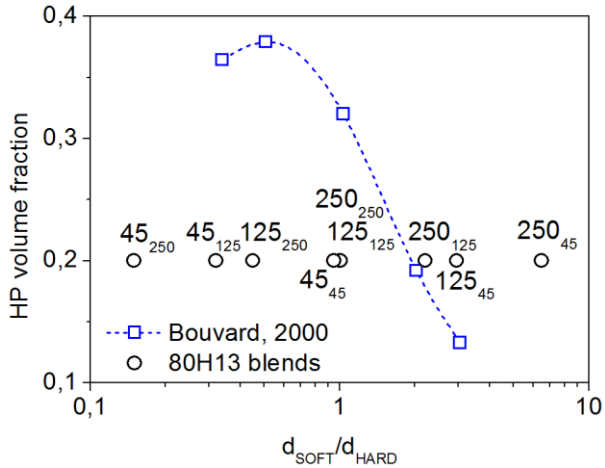
Figure V – 6. Percolation threshold as a function of hard particle volume fraction and particle size ratio according to Bouvard (2000) and values for 80H13 blends (adapted from Fedrizzi et al., 2012[1]).

The density of the 80H13 blends is mainly affected by the particle size of the principal component, i.e. AISI H13, as shown in Figure 7a, where the relative density is plotted as a function of the maximum AISI H13 particle size. Particularly, as the AISI H13 particle size decreases the relative density increases. This behaviour agrees with previous results, which showed an improvement in density as the mean particle size decreases and as the particle size distribution becomes narrower (Pellizzari et al., 2011[1]; Ting et al., 1994; Ting et al., 1995). Moreover, as the AISI H13 particle size decreases, the effect of AISI M3:2 particle size on density is minimized. Indeed the three samples with the smallest AISI H13 particles present the same value of density regardless of the AISI M3:2 particle size, while the three specimens with the bigger AISI H13 particles are characterized by quite different density values as the AISI M3:2 particle size changes (Fig. 7a).

Literature data show that relative density of soft/hard powder mixtures increases as the PSR decreases (Bonnenfant et al., 1998; Bouvard, 2000). The relative density of present blends as a function of the PSR is shown in Figure 7b. Considering samples having the same AISI M3:2 particle size it is clear that as PSR decreases relative density linearly increases in agreement with previous studies (Bonnenfant et al., 1998; Bouvard, 2000).

Figure 7b also points out the influence of the AISI M3:2 particle size on relative density. When considering samples having constant AISI H13 particle size, relative density trend shows a minimum as AISI M3:2 particle size changes. This minimum decreases as AISI H13 particle size decreases and it disappears for the smallest particle size, i.e. 80H1345$_{250}$, 80H1345$_{250}$ and 80H1345$_{250}$ samples. This

relation between relative density and AISI M3:2 particle size results from the superimposition of two distinct contributions as schematically shown in Figure 8. On one side there is the effect of the formation of aggregation/percolation microstructure (dashed curve in Fig. 8). For a constant AISI H13 particle size the PSR increases when AISI M3:2 particle size decreases. This leads to the formation of aggregates and percolative network of AISI M3:2 hindering blends densification (Bouvard, 2000). On the other side due to the decrease of AISI M3:2 particle size the "excluded volume" in the middle of the aggregates and the pores in the percolative skeleton also decrease as it is possible to see in Figure 5a,e,i. This results in increasing density as schematically shown by the dotted curve in Figure 8.
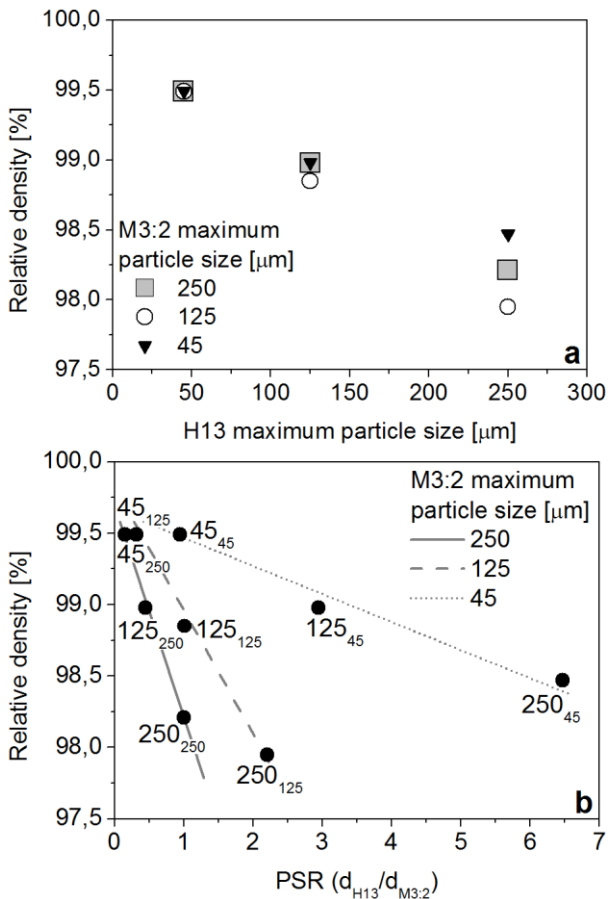

Figure V – 7. Relative density data as function of the maximum AISI H13 particle size (a) and as a function of the PSR ($d_{H13}/d_{M3:2}$) (b) (adapted from Fedrizzi et al., 2012[1]).
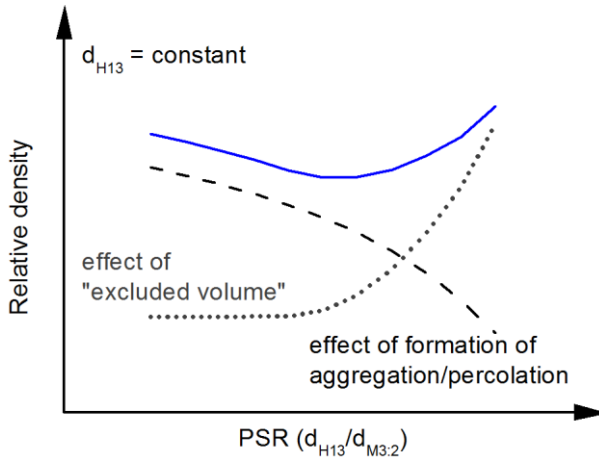
Figure V – 8. Scheme of the influence of AISI M3:2 particle size on the relative density (adapted from Fedrizzi et al., 2012[1]).

The lower punch displacement has been used to evaluate the material densification during sintering. The first derivative of displacement (ds/dT) against temperature is representative of the densification rate and it is shown in Figure 9. As previously stated (Pellizzari et al., 2011[1]), ferrite to austenite transformation during sintering is responsible for a slowdown in materials densification. Therefore the displacement first derivative curves present a minimum in correspondence to the ferrite to austenite transformation and consequently two relative maxima (Fig. 10). For all the nine samples the densification rate starts to slow down at about 830 °C, that is the onset of the ferrite to austenite transformation for AISI H13, and it reaches the minimum around 925 °C. Then the densification behaviour changes depending on the particle size of AISI H13, i.e. the main component of the blends. Figure 10 shows the influence of the particle size on the sintering rate and on the ferrite to austenite transformation in SPS. As particle size decreases the peak of sintering rate becomes narrower because densification is enhanced by smaller particles (Pellizzari et al., 2011[1]; Ting et al., 1994; Ting et al., 1995). It has been demonstrated (Diouf et al., 2012; Song et al., 2006) that during SPS of conductive powders the temperature at the contact points between particles is much higher than that of the particle core and this difference in temperature becomes greater as the particle size increases. This temperature difference is also confirmed by microstructural investigations on previous work sintered samples (Pellizzari et al., 2011[1]). AISI M3:2 sample sintered using particles smaller than 45 µm shows a coarser microstructure in the inner part of particles (areas A in Fig. 11) and a finer one at the particle surface (area B). This finer carbide precipitation can be due to the higher temperature achieved at the particle surface. This means that the ferrite to austenite

42

transformation occurs firstly near the contact points and only later at the particle core. Hence, the temperature range of transformation becomes wider as the particle size increases. Combining the influence of particle size on these two distinct effects it results that as the AISI H13 particle size increases the second relative maximum of the densification rate is shifted to higher temperature (Fig. 9). Indeed the blends with the smallest AISI H13 particles (samples $80H13-45_{250}$, $80H13-45_{125}$ and $80H13-45_{45}$) show the second peak at lower temperature (at about 1015 °C), while for the blends with medium sized AISI H13 particles (samples $80H13-125_{250}$, $80H13-125_{125}$ and $80H13-125_{45}$) the second peak occurs at 1045 °C just before the maximum sintering temperature. Finally in the case of the blends with the biggest AISI H13 particles (samples $80H13-250_{250}$, $80H13-250_{125}$ and $80H13-250_{45}$) the second peak falls beyond the maximum measured temperature (nearly 1070 °C). This means that for these samples the sintering cycle ends before complete densification as confirmed by their low relative density (< 98.5%).
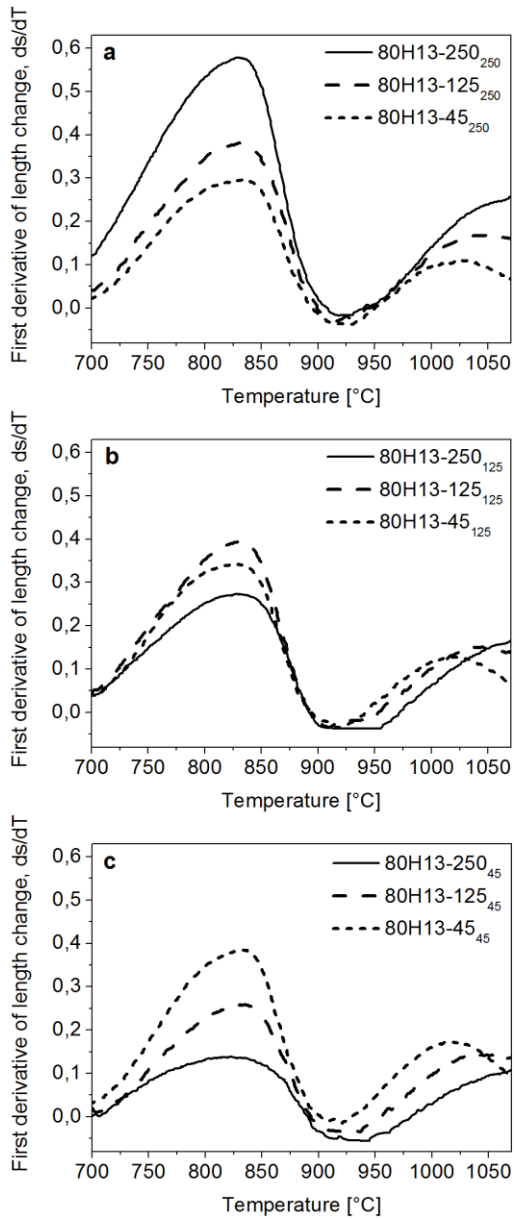
Figure V – 9. First derivative of displacement (ds/dT) against temperature during sintering for samples with biggest AISI M3:2 particles (a), with medium AISI M3:2 particles (b) and with smallest AISI M3:2 particles (c) (adapted from Fedrizzi et al., 2012[1]).
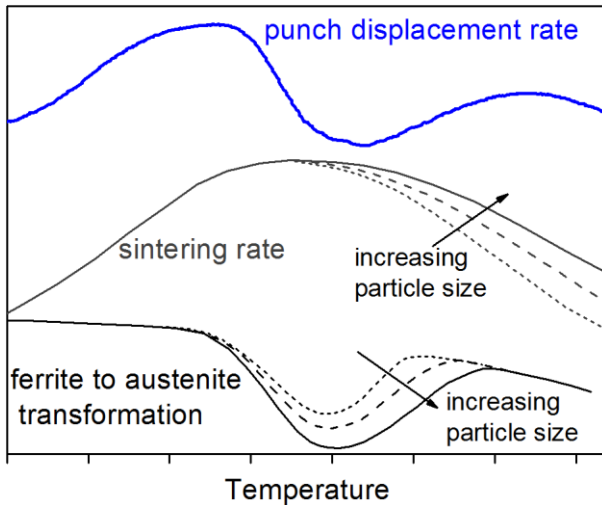
Figure V – 10. Schematic trend for sintering rate and ferrite to austenite transformation during SPS of tool steel powders (adapted from Fedrizzi et al., 2012[1]).
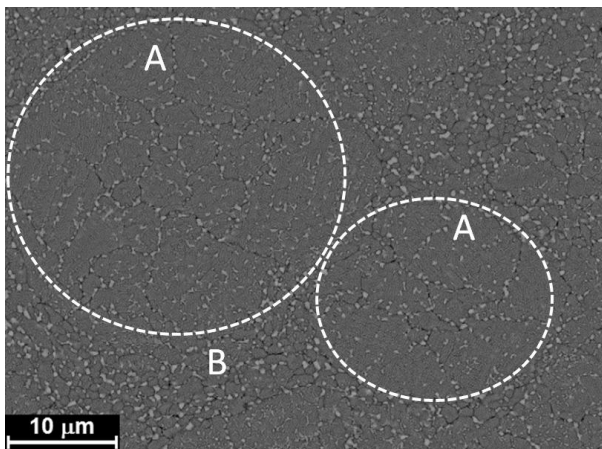
Figure V – 11. SEM micrograph of the microstructure of AISI M3:2 SPS sample sintered using as-atomized powder smaller than 45 µm.

The 80H13 blends hardness measured after thermal treatment is plotted in Figure 12 as a function of the relative density. Previous study on tool steel SPS (Pellizzari et al., 2011[1]) and literature data for ceramic materials, (Adachi et al., 2006; Abderrazak et al., 2011; Luo et al., 1999; Xu et al., 2009) showed that a lower porosity results in an improvement of hardness of sintered materials. Present materials confirm this behaviour showing a general increase of hardness as relative

density increases. Moreover as porosity decreases the standard deviation also decreases, meaning that materials become more homogeneous.

As shown for the relative density (Fig. 7b), as a first approximation three individual trends can be drawn according to AISI M3:2 particle size (curves in Fig. 12), meaning that this parameter also effects hardness. As AISI M3:2 particles become smaller the trend shifts to higher hardness, hence the three blends with the smallest AISI M3:2 particles (samples 80H13-250$_{45}$, 80H13-125$_{45}$ and 80H13-45$_{45}$) present the highest hardness in relation to their relative density. This improvement of hardness as AISI M3:2 particle size decreases can be related to the material microstructure. In the atomization process the cooling rate for smaller particles is much higher resulting in a much finer microstructure, as shown in Figure 13. Due to the fast heating rate and the short holding time in SPS, sintered materials still show these differences according to the particle size (Fig. 14). Therefore AISI M3:2 sintered using the smallest powder (0-45 µm) has a finer microstructure with small grains size (around 1 µm) and a finer and more homogeneous distribution of carbides (Fig. 14a). Both these features have a hardening effect on the AISI M3:2 component resulting in increased hardness for the whole composite.

The three densest blends (samples 80H13-45$_{250}$, 80H13-45$_{125}$ and 80H13-45$_{45}$) show relative density similar to that of the pure AISI H13 produced by SPS (99.5%) (Pellizzari et al., 2011[1]). As expected the addition of 20%vol of AISI M3:2 harder particles results in higher hardness compared to the pure AISI H13 (black square in Fig. 12).
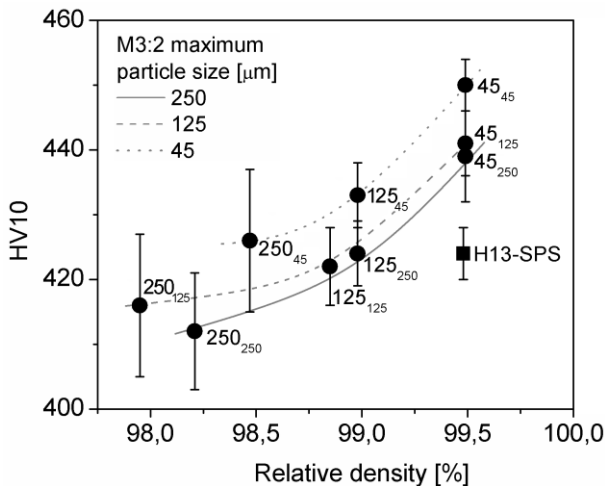

Figure V – 12. Hardness as a function of relative density (adapted from Fedrizzi et al., 2012[1]).
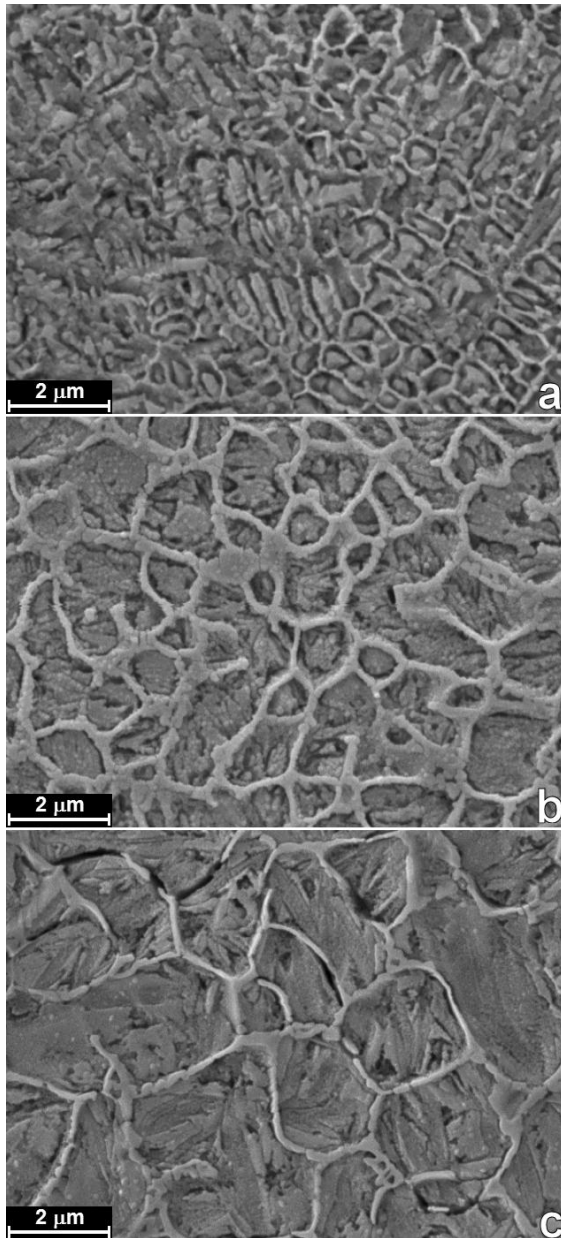
Figure V – 13. SEM micrographs of the microstructure of the AISI M3:2 powders depending on the particle size range: 0-45 µm (a), 45-125 µm (b) and 125-250 µm.
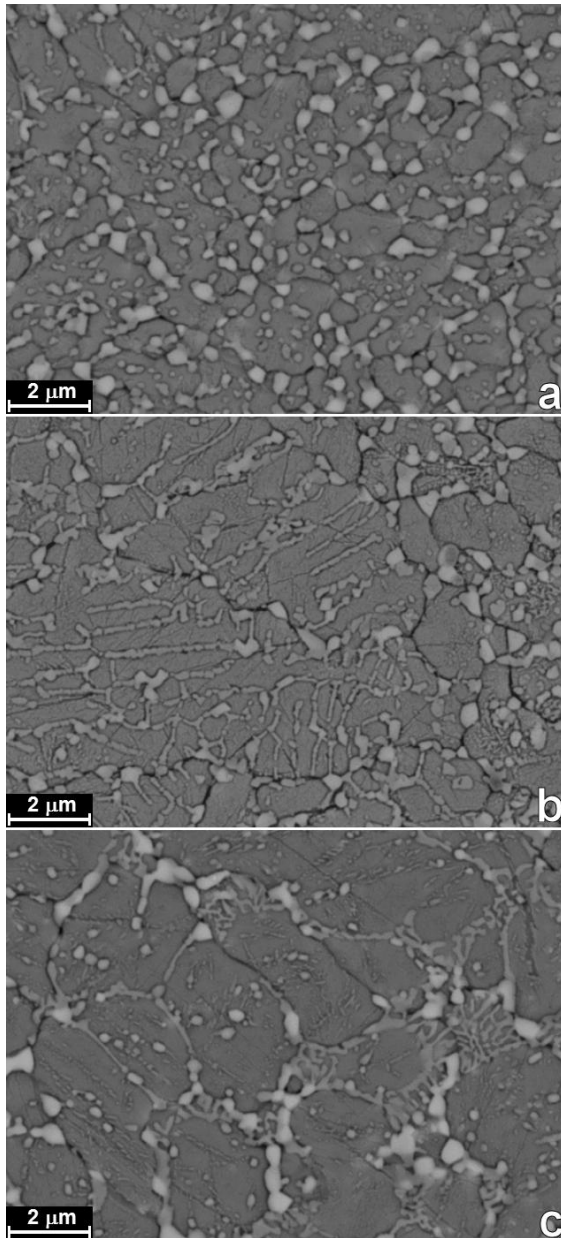
Figure V – 14. SEM micrographs of the microstructure of the sintered AISI M3:2 depending on the particle size range: 0-45 µm (a), 45-125 µm (b) and 125-250 µm.

Apparent fracture toughness (Fig. 15) shows a dependence on the density similar to that of hardness, confirming that density also influences mechanical properties of sintered materials (Adachi et al., 2006; Pellizzari et al., 2011[1]; Luo et al., 1999). Up to 99% of relative density apparent toughness increases linearly as relative density increases. In this range, apparent toughness seems not to be influenced by the AISI M3:2 particle size, as it has been highlighted for hardness instead (Fig. 12). When relative density is lower than 99%, the presence of pores mostly affects toughness, which decreases as porosity increases. In these conditions toughness is less sensible to other features, such as the presence of a brittle component. When considering the three highly dense blends (samples $80H13-45_{250}$, $80H13-45_{125}$ and $80H13-45_{45}$) the behaviour changes. In this case porosity has a minor effect and apparent toughness is influenced by AISI M3:2 particle size. Indeed as the harder particle size decreases apparent toughness increases considerably. This result can be explained by fractographic analysis. The two components show quite different fracture behaviour (Fig. 16). AISI M3:2 presents a brittle fracture characterized by flat surfaces which pass through the powder particles (area A in Fig. 16). In AISI H13 interparticle fracture occurs (rough area B in Fig. 16) The interparticle fracture is not typical for this material and it suggests that AISI H13 is not well consolidated even though it is well densified. Due to its poor consolidation, AISI H13 does not resist enough to crack propagation and therefore the crack can easily reach the harder AISI M3:2 particles where fracture propagation is accelerated due to their brittle behaviour. In this situation, smaller hard particles play a beneficial role on crack propagation improving the apparent toughness.

The addition of 20%vol of harder AISI M3:2 brings a decrease of toughness for all the 80H13 blends compared to that of pure AISI H13 produced by SPS (Pellizzari et al., 2011[1]) (squared data in Fig. 15). But in the case of sample $80H13-45_{45}$ this reduction of apparent toughness is quite restricted, about 3.6% only.
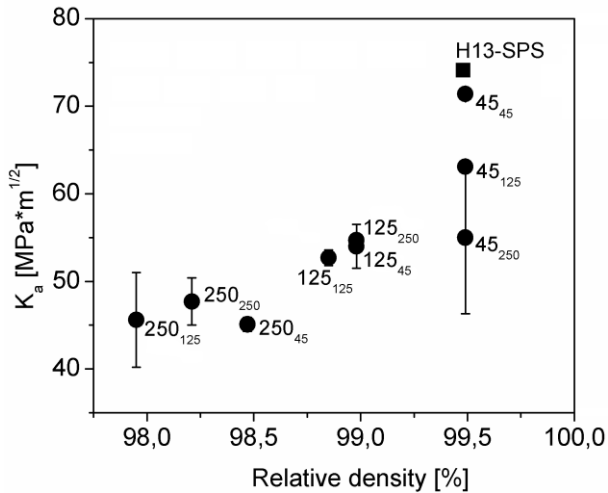
**Figure V – 15.** Apparent toughness as a function of relative density (adapted from Fedrizzi et al., 2012[1]).
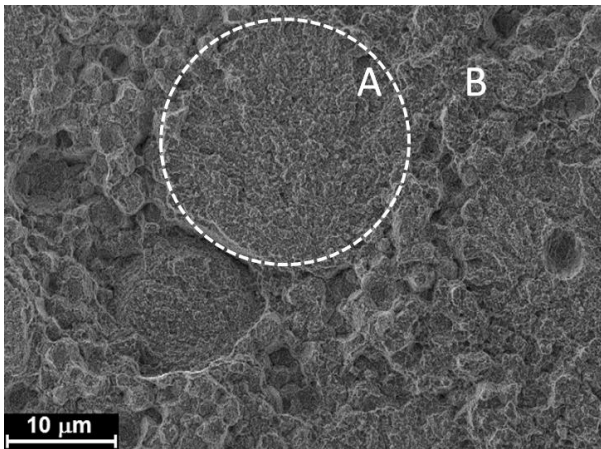
Figure V – 16. SEM micrograph of fracture surface for sample 80H13-45$_{250}$ (adapted from Fedrizzi et al., 2012[1]).

5.1.1   Conclusions

The microstructure of the nine 80H13 blends shows the effect of the PSR ($d_{H13}/d_{M3:2}$) on the phases distribution. If PSR is bigger than 1, the harder AISI M3:2 particles are not evenly dispersed and present the unwanted percolation structure. When PSR is close to 1 the harder particles tend to aggregates. To produce a

dispersion of isolated AISI M3:2 particles PSR has to be smaller than 1. This behaviour agrees with the analysis of Bouvard (2000) for soft/hard blends.

Density of the blends is mainly influenced by the particle size of AISI H13 (the major component) and it increases as the particle size decreases. The effect of PSR on density becomes evident comparing the samples with constant AISI M3:2 particle size. As PSR decrease the relative density increases. Considering samples with constant AISI H13 particle size, the curve of density vs. PSR shows a minimum due to the superimposition of two distinct contributions: the decrease of density by increasing PSR, due to the progressive formation of aggregates and percolative network of harder particles; the increase of density by increasing PSR, due to the smaller "excluded volume" formed between harder particles aggregates.

Relative density strongly influences both hardness and toughness which increase as density increase. Therefore the three highly dense samples made by small AISI H13 powders (blends 80H13-45$_{250}$, 80H13-45$_{125}$ and 80H13-45$_{45}$) presented the best hardness and apparent toughness.

The fine and homogeneous carbide dispersion and the small size of AISI M3:2 particles enable the sample 80H13-45$_{45}$ to gain the highest values of hardness combined with a very good toughness.

5.2 Influence of the Composition

As shown for the 80H13 blends, particle size influences the sintering kinetics (Fig. 10). Smaller particles enhance sintering and they reduce the temperature range of the ferrite to austenite transformation. According to this result it has been thought to reduce the particle size by MM.

The cumulative particle size distribution for as-atomized and mechanically milled AISI H13 and AISI M3:2 are compared in Figure 17. The as-atomized powders show a very similar particle size distribution with mean particle size equal to 123 µm and 115 µm for AISI H13 and AISI M3:2, respectively. After MM the particle size distributions become narrower and the mean particle size decreases to 14.6 µm for MM-H13 powder and to 18.3 µm for MM-M3:2 powder. The cumulative curves of the MM-powders have different shape: at the beginning (i.e. in the diameter range of 5-30 µm) the MM-M3:2 curve is less steep than the one of MM-H13 while the trend is inverted for larger diameters, i.e. MM-M3:2 curve is steeper than the MM-H13 one. This means that AISI M3:2 powder presents some big aggregates and it has not reached the equilibrium between fragmentation and agglomeration jet. This is confirmed by morphological and microstructural observations (Fig. 18 and 19). Both MM-powders show a round morphology, meaning that milling is not at the very early stage (Bailon-Poujol et al., 2011; Maurice et al., 1994), but MM-M3:2 has much bigger particles (Fig. 18b). Low magnification micrograph (Fig. 19c) confirms that

these big particles are aggregates which on the other hand are not present in the MM-H13 (Fig. 19a).

In MM-H13 (Fig. 19b) the as-atomized microstructure has completely disappeared due to the cold welding and fragmentation phenomena occurring during MM (Benjamin et al., 1974; Maurice et al., 1994; Suryanarayana, 2001). These events result in the stretching and deformation of the dendritic microstructure of the as-atomized powder, leading to the formation of a lamellar microstructure (Çetinkaya et al., 2007; Suryanarayana, 2001). As the milling time increases the lamellae become thinner until the microstructure is fully homogenized. After 1000 minutes no more traces of lamellar microstructure can be seen for AISI H13 (Fig. 19b) meaning that the MM process has been properly carried out. Microstructure investigation on MM-H13 also highlights the presence of some porosity inside the milled particles.

The MM-M3:2 powder microstructure shows some pores and traces of cellular structure (Fig. 19d) confirming that present MM conditions for AISI M3:2 are far from the optimum. Increasing milling time can be considered in future works to obtain the best microstructure for MM-M3:2 powder, too.
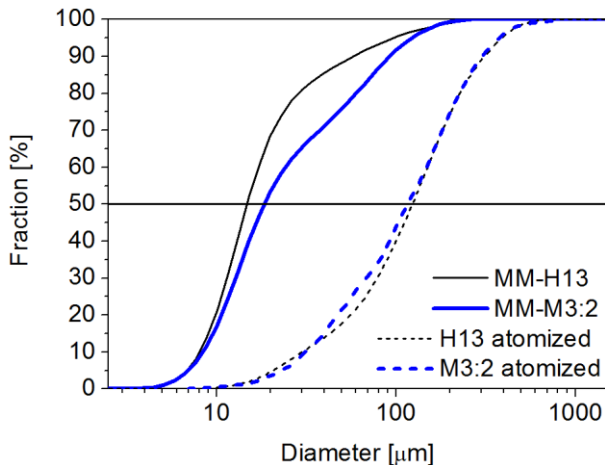
Figure V – 17. Cumulative particle size distribution of AISI H13 and AISI M3:2 powders after atomization and after MM.
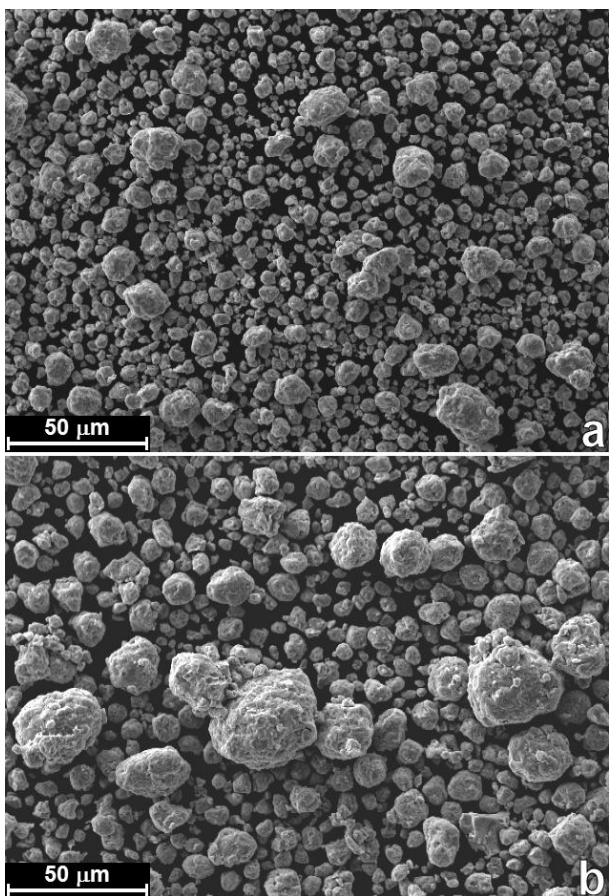
Figure V – 18. SEM micrographs of the morphology of the MM-H13 powder (a) and of the MM-M3:2 powder (b).
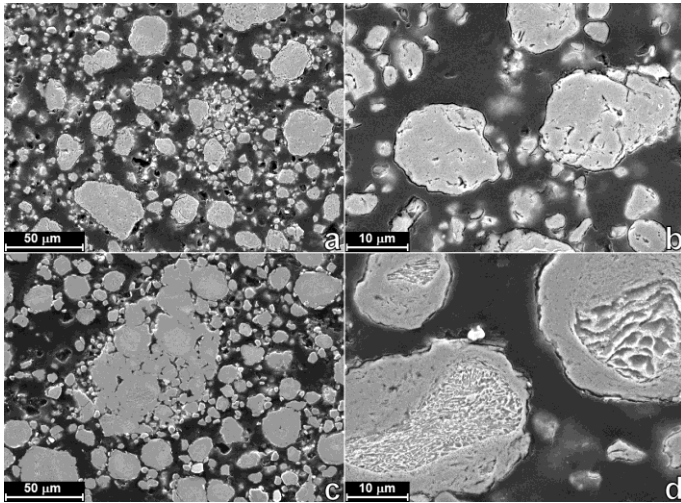
**Figure V – 19.** SEM micrographs of the microstructure of the MM-H13 powder at lower (a) and higher (b) magnification and of the MM-M3:2 powder at lower (c) and higher (d) magnification.

Microstructure of sintered MM-H13 and MM-M3:2 is shown in Figure 20. For both steels the grain size is much smaller than that shown for the as-atomized materials (Fig. 1). In the MM-H13 (Fig. 20a), MM has strongly refined the microstructure and finely dispersed the carbides which can now be seen only at higher magnification. Also in the case of MM-M3:2 the microstructure has been greatly refined by MM (Fig. 20b), but in this steel its higher alloying elements content results in a greater carbide precipitation, as previously stated (par. 5.1). The not uniform microstructure of the MM-M3:2 powder is responsible for the not homogeneous microstructure of the sintered material. Where MM has completely destroyed the cellular structure of the atomized powder and fully homogenized the steel structure the sintered material shows a fine and uniform distribution of carbides which act as a barrier to the grain growth. On the other hand where the cellular structure has not been destroyed carbide distribution is less homogeneous and the grain size is bigger.
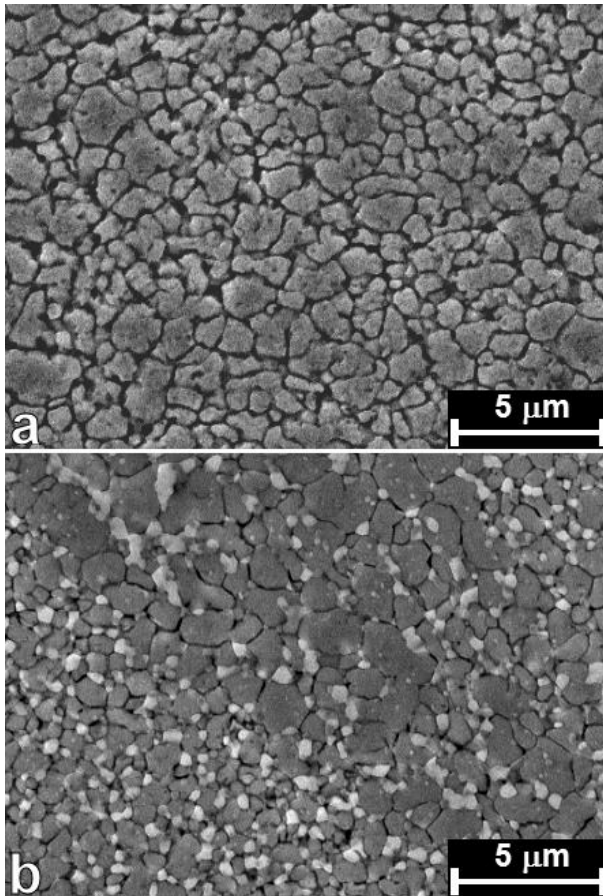
Figure V – 20. SEM micrographs of the microstructure of MM-H13 (a) and MM-M3:2 (b) after sintering.

The microstructure of the four blends is shown in Figure 21. It is possible to see that the two components are uniformly distributed in all the four MM-blends and the microstructures are quite homogeneous. The reduction of the particle size, especially of the biggest particles, results in a more uniform microstructure than that produced by using as-atomized powders (Fig. 22). MM-blends do not show any porosity which is very evident in the as-atomized blends instead (Pellizzari et al., 2011[2]).
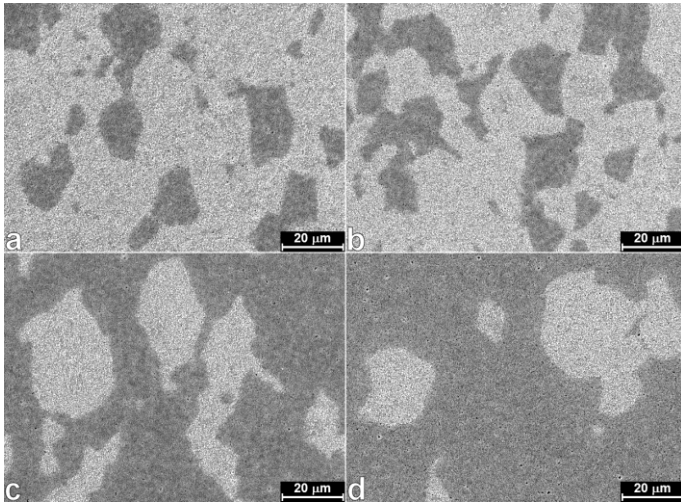
Figure V – 21. SEM micrographs of the microstructure of MM-20H13 (a), MM-40H13 (b) MM-60H13 (c) and MM-80H13 (d) after sintering. Brighter areas are AISI M3:2 and grey areas are AISI H13 (adapted from Fedrizzi et al., 2012[2]).
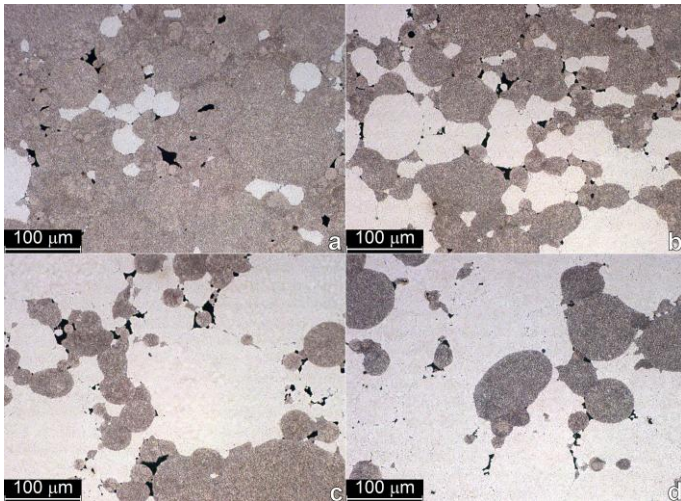
Figure V – 22. Optical micrographs of the microstructure of as-atomized blends 20H13 (a), 40H13 (b) 60H13 (c) and 80H13 (d) after sintering. Brighter areas are AISI H13, darker areas are AISI M3:2 and black spots are pores (adapted from Pellizzari et al., 2011[2]).

The absolute density of the MM-samples decreases linearly as the weight fraction of AISI H13 (i.e. the component with lower density) increases (black data in Fig. 23), in good agreement with the linear rule of mixture. The relative density

56

(empty circles in Fig. 23) has been calculated as the ratio to the density of the MM-powders measured by a pycnometer. Since the MM-powders have some internal porosity, especially the MM-M3:2 (Fig. 19), these measures are thought to be lower than the theoretical density of the two MM-steels. Therefore the relative density of MM-samples can be a little bit higher than the real values, particularly for the specimens with high amount of HSS, i.e. MM-M3:2, MM-20H13 and MM-40H13. In any case these data are meaningful and they show that all the MM-samples achieve high density, very close to theoretical one (relative density higher than 99.4%), as already highlighted by microstructural observations (Fig. 21).

Figure 24 shows previous density data for materials sintered using as-atomized powders (Pellizzari et al., 2011[2]). In that case the two base steels were sintered up to nearly full density (relative density around 99.5%) but all the four blends did not achieve theoretical density values predicted by the linear rule of mixture (dotted line in Fig. 24). All the four blends showed a high porosity (Fig. 22) and lower density (between 98.8% and 99.0%) than the two base steels.
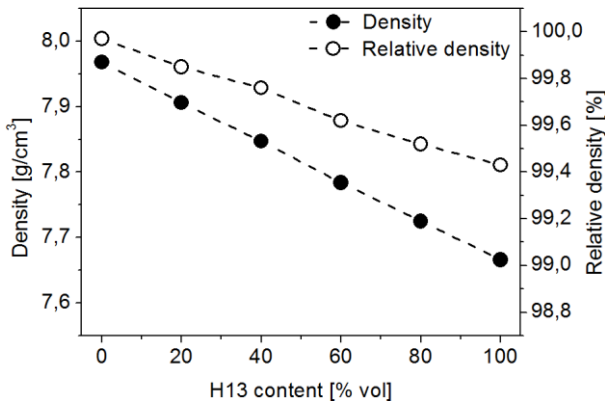
Figure V – 23. Density and relative density of the MM-samples as a function of the AISI H13 content.
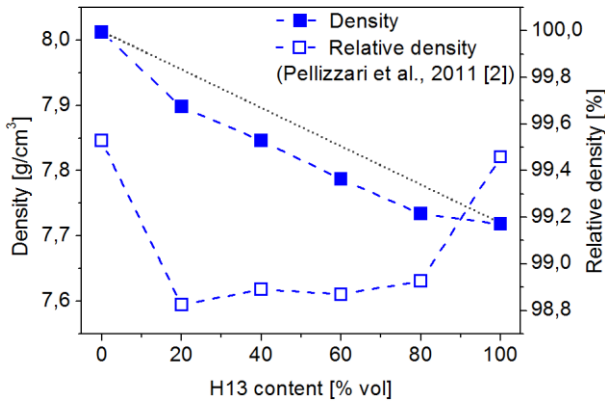
Figure V – 24. Density and relative density of the samples produced with as-atomized powders as a function of the AISI H13 content (adapted from Pellizzari et al., 2011[2]).

To better understand densification behaviour the punch displacement during sintering has been investigated. Figure 25 shows the first derivative of the punch displacement for MM-H13 and MM-M3:2. For comparison, data of samples produced using as-atomized powders have also been plotted (Pellizzari et al., 2011[2]). As highlighted for the 80H13 blends (Fig. 9) the derivative curves show a minimum in correspondence of the ferrite to austenite transformation. Also the MM-samples present this behaviour. MM-M3:2 shows this minimum at lower temperature (about 850 °C) than MM-H13 (around 900 °C). This is because the ferrite to austenite transformation occurs at lower temperature in the AISI M3:2 steel as it is shown by the dialtometric curves in Figure 26. Compared to the as-atomized samples (dashed lines in Fig. 25), MM-samples show higher densification rate and a new relative maximum around 750 °C, which was not shown by any material produced with as-atomized powders (Pellizzari et al., 2011[2]). Moreover the sintering peak of both MM-steels ends at a lower temperature (about 1050 °C) than that of the as-atomized samples. These results suggest that MM activates sintering, shifting the sintering peak at lower temperature (Zoz et al., 2003). It is plausible that both particle size and microstructural refinements promote sintering, particularly in in the range of low temperature, i.e. before 800 °C. The activation produced by MM seems more efficient for MM-M3:2. Indeed MM-M3:2 shows the highest densification rate and all its peaks are shifted to lower temperature than MM-H13. The as-atomized samples show reverse behaviour than MM-steels, i.e. as-atomized H13 densification occurs at lower temperature than that of as-atomized M3:2.

The derivative curves for all MM-sample are shown in Figure 27. The behaviour of the four blends follows the trend of their main component. This means that the MM-20H13 and MM-40H13 curves follow the MM-M3:2 one, while the MM-60H13 and MM-80H13 samples behave like the MM-H13. The densification of all

MM-samples ends before the maximum sintering temperature, suggesting that sintering temperature could even be decreased to 1050 °C.

The densification rate of the blends produced using as-atomized powder is plotted in Figure 28. Previous analysis (Pellizzari et al., 2011[2]) has highlighted that the different sintering kinetics of the two base steels hinder the densification of the blends, but this negative interaction can be minimized by reducing the particle size (Fig. 28b). Present data on the MM-samples confirm this last assumption. Indeed due to the particle size reduction achieved by MM, the MM-blends follow the base steels behaviour according to their composition (Fig. 27) as it was shown for as-atomized powder smaller than 45 µm (Fig. 28b).
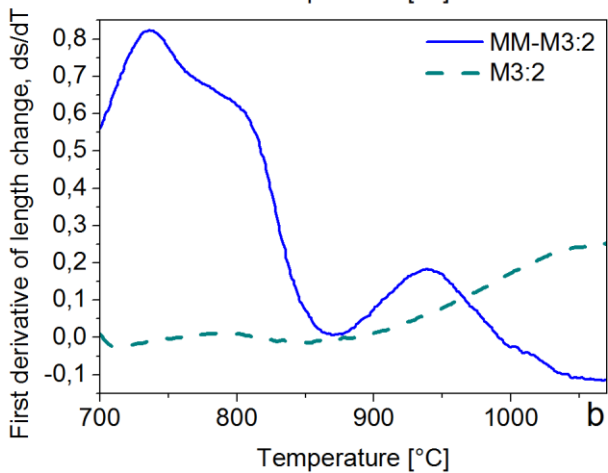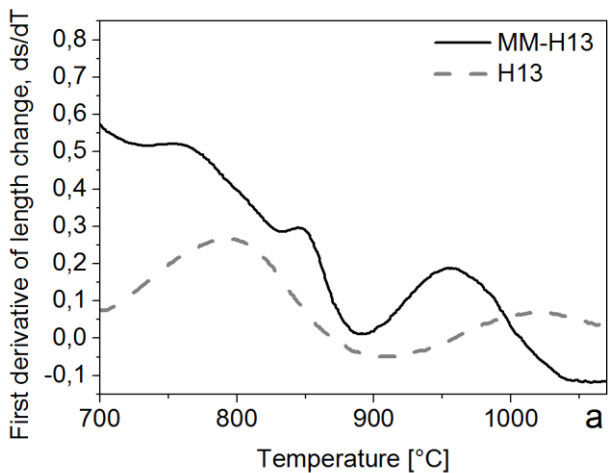
Figure V – 25. First derivative of displacement (ds/dT) against temperature during sintering for MM and as-atomized AISI H13 (a) and for MM and as-atomized AISI M3:2 (b).
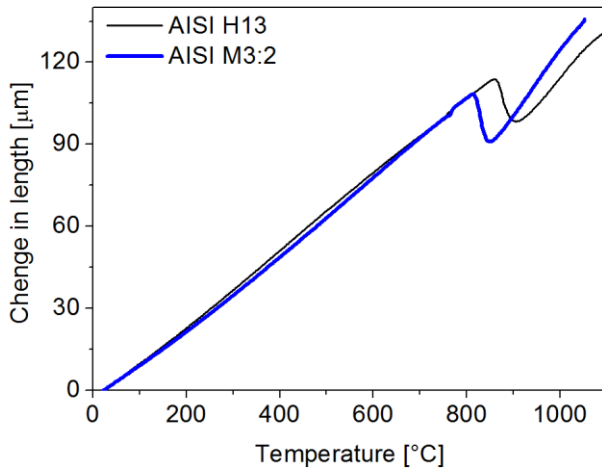
**Figure V – 26.** Change in length as a function of temperature.
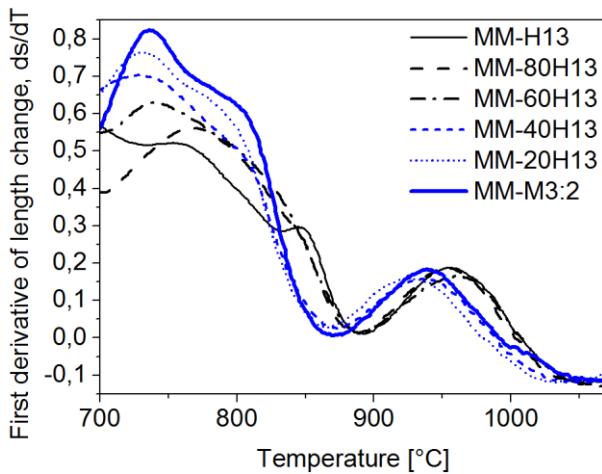
**Figure V – 27.** First derivative of displacement (ds/dT) against temperature during sintering for the MM-samples.
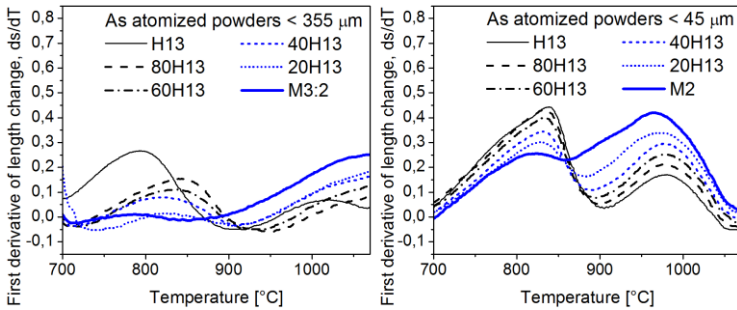
Figure V – 28. First derivative of displacement (ds/dT) against temperature during sintering for the sample sintered using as-atomized powders (adapted from Pellizzari et al., 2011[2]).

Hardness of the heat treated MM-samples is shown in Figure 29. The fine martensitic microstructure and the high amount of carbides in the MM-M3:2 are responsible for its higher hardness (about 546 HV10). As the AISI H13 content increases the hardness decreases down to 422 HV10 for the MM-H13. The lower hardness of AISI H13 is due to its lower content of carbon and alloying elements (Tab. IV-1) which results in the formation of a softer martensite with lower amount of carbides.

It is noticeable that all the four MM-blends achieve higher hardness than that predicted by the linear rule of mixture (dashed line in Fig. 29). Mechanisms responsible for the deformation behaviour in MMCs have scarcely been investigated so far and thus it is hard to predict MMCs properties (Pramanik et al., 2008; Shen et al., 2001). Experimental and numerical investigations showed that the dispersion of HPs in the metal matrix increases the flow resistance resulting in improved hardness (Pramanik et al., 2008). Investigation on the correlation between hardness and tensile strength highlighted that the slight improvement of tensile strength resulting from the addition of HPs may correspond to a comparatively higher increase of hardness (Shen et al., 2001). This higher work hardening for MMCs may be ascribed to different factors, among which the local increase in HPs concentration during loading and the parallel decrease in volume of matrix being deformed (Shen et al., 2001) and the change of stress distribution leading to the generation of stresses higher than the yield stress of the matrix since the initial stage of indentation (Pramanik et al., 2008). Consequently MMCs show higher work hardening rate than the pure metal (Pramanik et al., 2008). For present MM-blends it can be plausibly assumed that the dispersion of particles of a second constituent causes a similar modification of the stress field resulting in increased work hardening of the matrix.

As shown in Figure 29, after thermal treatment the hardness of the two base MM-steels is very close to that of the as-atomized materials (Pellizzari et al., 2011[2]). Indeed the tempering curves for AISI H13 show that the MM-steel hardness remains much higher than that of the as-atomized materials until the

secondary hardness peak (around 500 °C) (Fig. 30) (Pellizzari et al., 2012). For higher tempering temperature the hardness of MM-H13 suddenly drops to the same value of that of AISI H13 produced by as-atomized powder. Present MM-samples have been tempered at 625 °C so that the hardness is nearly the same of as-atomized AISI H13 (Fig. 30). It is plausible that AISI M3:2 would show similar behaviour and that at this tempering temperature all the hardening effects induced by MM are vanished. On the contrary all the MM-blends are harder than those obtained using as-atomized powders, which show a negative deviation from the linear rule of mixture. This result is directly correlated to the poor densification of these samples (Fig. 24) (Pellizzari et al., 2011[2]). In conclusion, present data confirm the efficacy of MM as a powerful technique for the achievement of high relative density and good hardness.
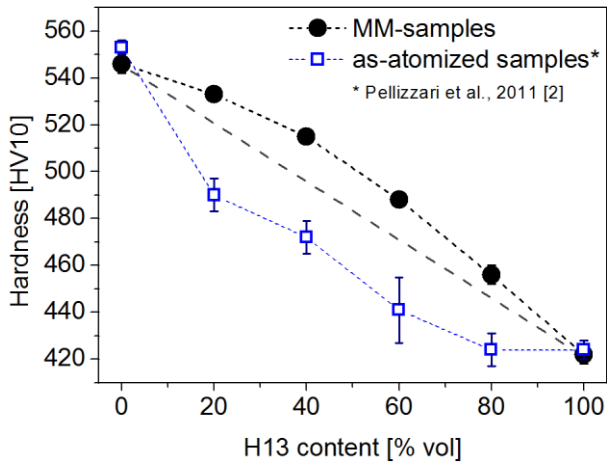
Figure V – 29. Hardness of the MM-samples and as-atomized samples after heat treatment as a function of the AISI H13 content (adapted from Fedrizzi et al., 2012[2]).
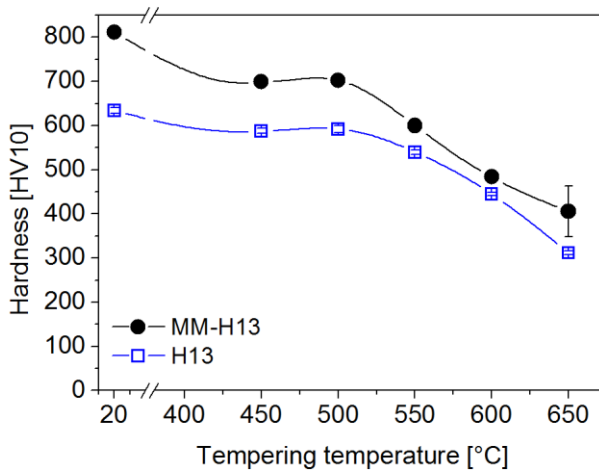
Figure V – 30. Tempering curves for AISI H13 sintered from MM-powder and as-atomized powder (adapted from Pellizzari et al., 2012).

Figure 31 shows the apparent toughness for the MM-samples. MM-M3:2 shows lower apparent toughness than MM-H13 according to its microstructure (Fig. 20) and its hardness (Fig. 29). The four MM-blends reach apparent toughness values in between those of the two base MM-steels. The values of the two blends containing a higher fraction of AISI H13 (i.e., MM-80H13 and MM-60H13) are close to those predicted by the linear rule of mixture (dashed line in Fig. 31). On the other hand, in MM-40H13 and MM-20H13, the addition of AISI H13 provides a positive deviation from the rule of mixture, suggesting a beneficial influence beyond that expected by simple mechanical mixing. As far as author experience is concerned, AISI H13 produced by SPS generally shows interparticle fracture resulting in quite rough fracture surface (Pellizzari et al., 2009; Pellizzari et al., 2011[2]). This behaviour highlights poor consolidation of AISI H13 in SPS, but this can give a toughening effect when AISI H13 particles are placed in a less tough matrix. During fracture propagation the AISI H13 particles force the crack to follow their surface (details A in Fig. 32b) instead of passing across AISI M3:2 particles (details B). This makes the crack path more winding and it dissipate more energy resulting in increasing material toughness. Moreover AISI H13 particles act as a barrier against crack propagation (Fig. 32c) and this also has a toughening effect. On the other hand, in the AISI H13 rich blends, the AISI M3:2 particles do not obstruct the propagation of the crack which proceeds straight across them (Fig. 33) decreasing the HWTS toughness in agreement with the linear rule of mixture.

Compared to the as-atomized materials (blue squares in Fig. 31) (Pellizzari et al., 2011[2]), the apparent toughness of the MM-M3:2 drops from 46 MPa*m$^{1/2}$ to 34 MPa*m$^{1/2}$ and that of MM-H13 from 77 MPa*m$^{1/2}$ to 58 MPa*m$^{1/2}$. This can be

explained in view of the oxygen pick-up shown by the powders after MM (Tab. 1). Due to the lack of a suited insulation system the oxygen content increases almost one order of magnitude compared to as-atomized powders (Tab. IV-1). The surface of the MM-powders is covered by a thin oxide layer which impairs consolidation during sintering, reducing toughness (Arnberg et al., 1988; Pellizzari et al., 2009; Pellizzari et al., 2011[2]). This result suggests that if the oxygen content had not increased, the toughness of all MM-samples could have been 10-20MPa*m$^{1/2}$ higher. However, despite of the negative effect of the higher oxygen content, all MM-blends show higher toughness than as-atomized blends (Fig. 31) which exhibit higher porosity (Fig. 24) (Pellizzari et al., 2011[2]). It can be concluded that the high porosity due to poor densification is more detrimental for toughness than high oxygen content. In other words, for the production of hybrid tool steels obtained by blending different powders, the benefits on densification by MM largely compensate the detrimental effect of higher oxygen content. Unquestionably, proper systems aimed at reducing oxidation could bring to much higher benefits than those evidenced in this research.
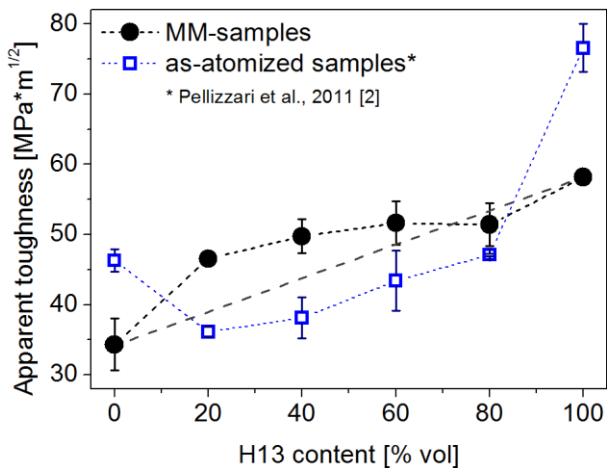
Figure V – 31. Apparent toughness of the MM-samples and as-atomized samples after heat treatment as a function of the AISI H13 content (adapted from Fedrizzi et al., 2012[2]).
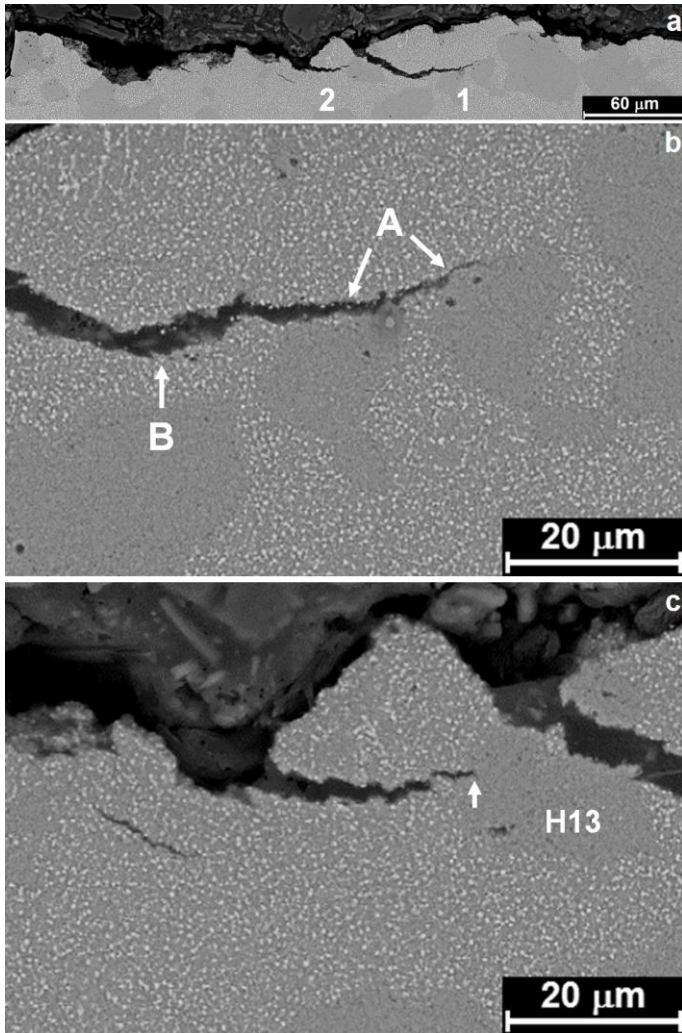
Figure V – 32. SEM micrograph of fracture propagation near the notch in MM-20H13: low magnification (a) and higher magnification of area 1 (b) and area 2 (c).
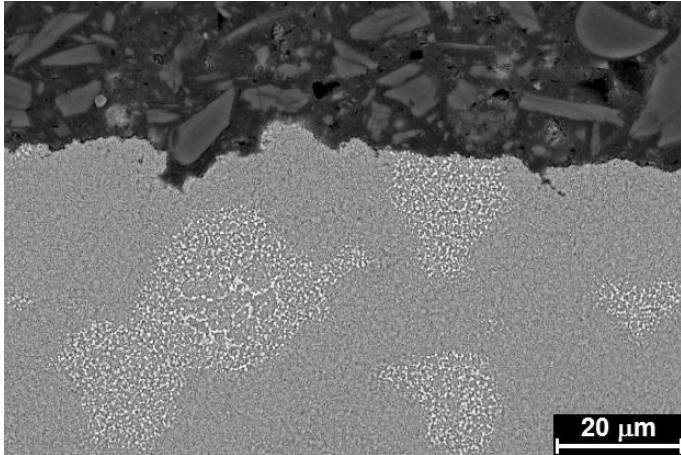
Figure V – 33. SEM micrograph of fracture propagation in MM-60H13.

Table V – 1. Oxygen and nitrogen content in the MM-powders [weight %].

Powder	O	N
MM-H13	0.1702	0.0978
MM-M3:2	0.1391	0.0950

5.2.1   Conclusions

MM has been successfully applied to reduce the particle size of AISI H13 and AISI M3:2, so to minimize their negative interference during co-sintering. The milling parameters have been already optimized for AISI H13 powder, which therefore shows a high refinement and a homogeneous microstructure after MM. MM process for AISI M3:2 has not been investigated so far and therefore MM of AISI M3:2 has been carried out in the same condition as for MM-H13. MM-M3:2 powder is less refined than MM-H13 and its microstructure is not completely homogenized. Traces of the as-atomized dendritic structure or of the lamellar structure, which is formed in the early stage of MM, can still be found in several particles. These results suggest that MM-M3:2 powder has not achieved the steady state of milling, probably because of a too short milling time.

Spark plasma sintered MM-samples achieve near full density confirming that the interference during co-sintering due to the different material densification kinetics can be minimized or completely eliminated by reducing the powder particle size. The higher density, hardness and toughness of MM-blends than that fabricated using as-atomized powders confirm the positive influence of MM.

Present results confirm that properties of the hybrid steel can be modulated by changing the blend composition. Density, hardness and apparent toughness of the

MM-blends fall in between the values measured for the two base MM-steels according to the HWTS/HSS content.

The lack of a suited protection against oxidation for MM-powders has caused a sharp increase of the oxygen content resulting in a marked drop of toughness for the two base MM-steels. Their toughness is much lower than that of samples produced using as-atomized powders. In spite of this higher oxygen content the toughness of the MM-blends is higher than that of the as-atomized blends. Indeed the positive influence of a higher density largely compensates the detrimental influence of the higher oxygen content.

Chapter VI

HWTS Based MMCs

6.1   *MA-powders characterization*

Figure 1 shows the particle size distribution of sMM-H13 powder and the three MA-powders (i.e. MA(H13+20TiB$_2$), MA(H13+20TiC) and MA(H13+20TiN)). The particle size distribution of as-atomized AISI H13 (par. 4.1.1) is also plotted for comparison. The soft MM of the pure steel nearly halves the mean particle size (59 μm) and promotes a narrower particle distribution, as confirmed by the steeper slope of the sMM-H13 line in Figure 1a. Compared to MM-H13 (Fig. V-17), the particle size refinement of sMM-H13 is much less intense. It has to be recalled that for sMM-H13 softer milling conditions have been applied, i.e. shorter time and lower BPR than MM-H13 (see par. 4.2.1.1 and 4.1.1.2, respectively). All the MA-powder curves are shifted towards left hand side. Their particles are smaller than 50 μm and their mean particle size falls below 10 μm (9.83μm, 9.42μm and 7.86μm for MA(H13+20TiB$_2$), MA(H13+20TiC) and MA(H13+20TiN), respectively). The presence of a hard phase enhances the particle refinement, which is reflected in a narrower size distribution and smaller mean particle size (Bailon-Poujol et al., 2011). MA(H13+20TiB$_2$) and MA(H13+20TiC) powders have nearly the same particle size distributions. It can be inferred that, in spite of its slightly lower hardness and its considerably smaller mean

particle size (par. 4.2.1), during MA TiC acts on the particle size refinement in a quite similar way to TiB₂. In the case of MA(H13+20TiN), the size distribution curve is further shifted to left hand side. TiN is the least hard reinforcement but it results to be more efficient in refining particle size than the other two compounds considered in this work.
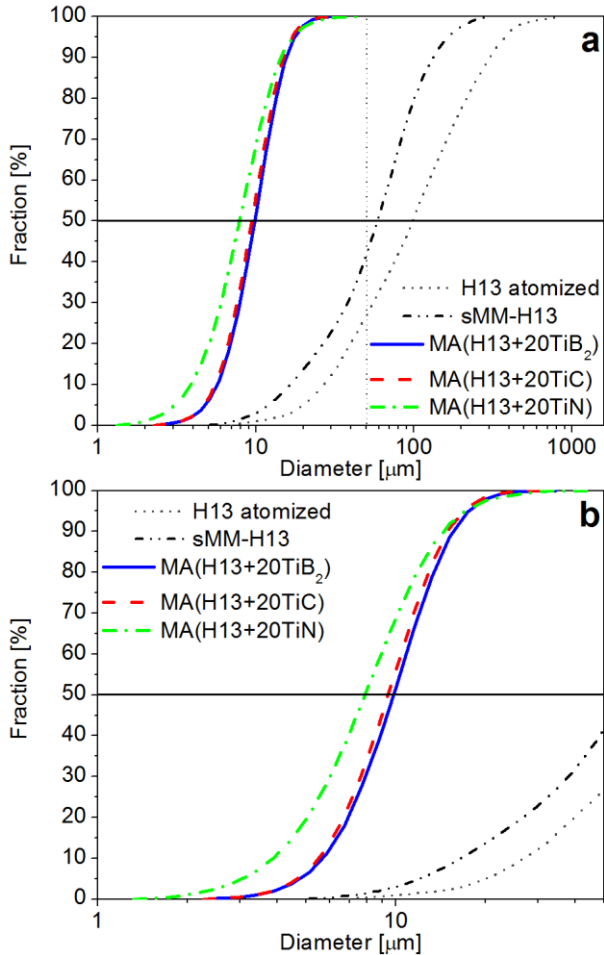
Figure VI – 1. Cumulative particle size distribution of as-atomized AISI H13, sMM-H13 and MA-powders: complete range (a) and the zoom for diameter < 50 μm (b) (adapted from Fedrizzi et al., 2013[1]).

The powder morphology is shown in Figure 2. Compared to the as-atomized AISI H13 particles (Fig. IV-1a), those of sMM-H13 are heavily deformed, being flat and elongated (Fig. 2a). This morphology is the typical one observed in the early stages of MM, when cold welding prevails over fragmentation (Maurice et al., 1994; Suryanarayana, 2001). SEM micrographs of the MA-powders (Fig. 2b,c,d) confirm the stronger refinement of particle size than sMM-H13. Moreover the presence of the HPs in the three MA-powders promotes a much rounder morphology. Particles have irregular shape but they are nearly equiaxial. The brittle HPs enhance the fragmentation process so that all MA-powders show the typical morphology of the second stage of MM, observed when fragmentation prevails over cold welding (Maurice et al., 1994; Suryanarayana, 2001). Indeed the presence of a brittle phase shifts all the stages of MM to lower times (Bailon-Poujol et al., 2011; Suryanarayana, 2001).
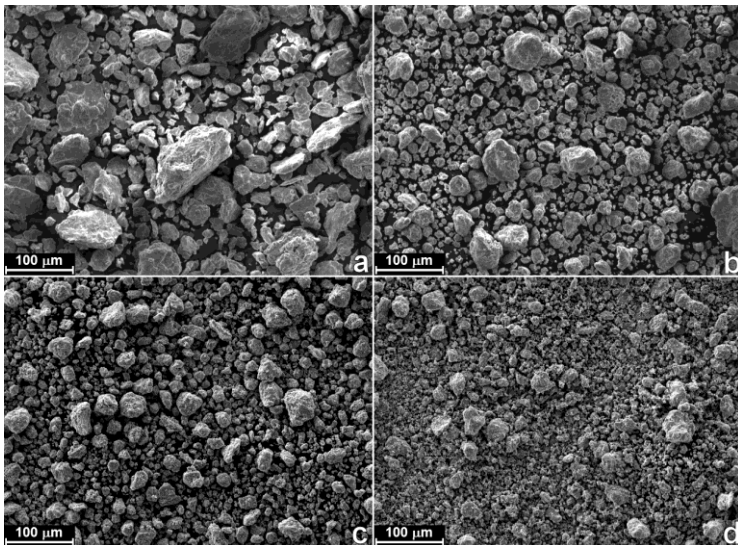
Figure VI – 2. SEM micrographs of the morphology of the sMM-H13 (a), MA(H13+20TiB$_2$) (b), MA(H13+20TiC) (c) and MA(H13+20TiN) (d) powders.

Figure 3 shows the microstructure of the milled powders. As described in paragraph 4.1.1, the as-atomized AISI H13 powder microstructure is constituted by dendrites surrounded by microsegregated regions (Fig. IV-3a). MM destroys this cellular microstructure, as evidenced by the distribution of the super-saturated phase which is stretched in lines, finely wrapped and closely packed (Fig. 3a). This lamellar microstructure is characteristic of the early stage of MM and the strain level can be identified by the spacing of microsegregated areas (Çetinkaya et al., 2007;

Suryanarayana, 2001). Generally, the deformation is not uniform through a particle section and particles showing different extent of deformation can be distinguished (areas A and B in Fig. 3a). As previously stated, these microstructures also indicate that MM has not achieved the stationary stage yet (Suryanarayana, 2001). The microstructures of the MA-powders (Fig. 3b,c,d) confirm that MA allows the HPs to be finely dispersed in the steel matrix. However their distribution is not uniform and large areas of pure poorly deformed steel, showing a lamellar structure, are still present inside the particles. As reported by Suryanarayana (2001), in the initial stages of MA, the collisions between balls and powder flatten the ductile metal particles and fragment the brittle ceramic particles. These small fragments of HPs are included and trapped in by the ductile metal powders and they are arranged along the interlamellar spacing. Longer milling time refines the lamellar microstructure, decreasing the interlamellar spacing and producing a more uniform dispersion of HPs (Suryanarayana, 2001). For systems similar to those investigated here it was stated that there is an optimal MM time leading to small powders with uniform distribution of reinforcement (Angers et al., 1999; Liu et al., 2001). In view of these studies it can be suggested that longer MM time could result in a more homogeneous HPs distribution.
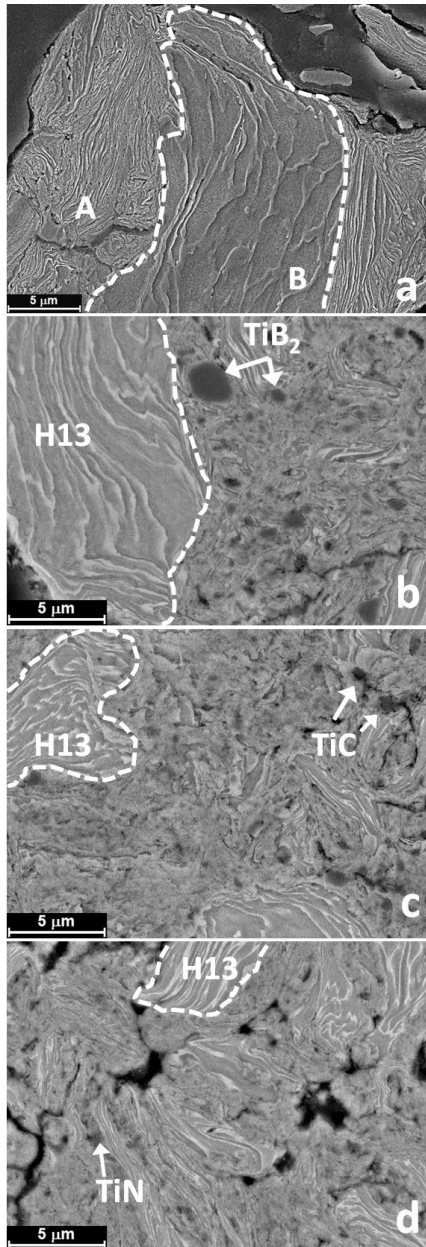
Figure VI – 3. SEM micrographs of the microstructure of the sMM-H13 (a), MA(H13+20TiB$_2$) (b), MA(H13+20TiC) (c) and MA(H13+20TiN) (d) powders.

As stated in paragraph 4.1.1, the atomized AISI H13 powder is constituted by ferrite (Fe-α) and retained austenite (Fe-γ) (Fig. IV-4a). The strain induced transformation of retained austenite into martensite takes place during MM (Delogu, 2011; Huang et al., 1996; Zoz et al., 2003) so that in the diffraction pattern of sMM-H13 no peaks pertaining to austenite can be detected (Fig. 4a). The XRD analyses of the MA-powders (Fig. 4b,c,d) show the peaks of ferrite and of the corresponding ceramic phase. The quantitative analysis reveals that the HP volume fraction is about 22.3% for MA(H13+20TiB$_2$) and MA(H13+20TiC) and 23.7% for MA(H13+20TiN). These results are in good agreement with the original target compositions (Tab. IV-6). No peaks pertaining to any other phases are present confirming that MA does not involve chemical reaction between the metal matrix and the HPs (Angers et al., 1999; Liu et al., 2001).
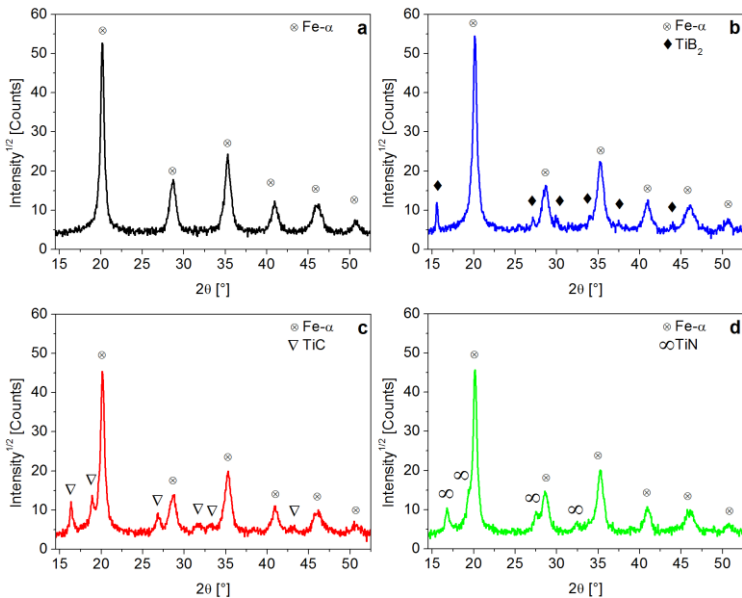
Figure VI – 4. XRD patterns for the sMM-H13 (a), MA(H13+20TiB$_2$) (b), MA(H13+20TiC) (c) and MA(H13+20TiN) (d) powders.

6.2   TiB$_2$ – MMCs: Analysis of the Processing Route

The influence of powder mixing or MA on the sintering process has been evaluated following the densification of the samples (Tab. IV-5). Both sintering shrinkage and final density have been considered.

Figure 5 shows the displacement of the lower punch and its first derivative, which represent the material densification and densification rate respectively, as a

function of sintering time. When load is applied after 360 s (corresponding to 600 °C), the lower punch start to move, and firstly, until the load reaches its maximum value after 480 s, the displacements increase almost linearly (Fig. 5a). In this first stage the displacement is mainly due to the rearrangement of the particles and it is ruled by their compressibility. The softest powder, i.e. sMM-H13, achieves the highest displacement in view of the highest densification rate (Fig. 5b). The presence of coarse hard TiB_2 particles in sMM-H13+20TiB_2 decreases the compressibility of the powder reducing the densification rate. This effect is more evident in MA(H13+20TiB_2) where the finer dispersion of TiB_2 particles (Fig. 3b) further impairs densification. During the second stage, i.e. heating up to the maximum temperature under constant load, a reduced displacement rate is observed for all materials. Under maximum constant load, densification proceeds at lower rate. In this stage the displacement of MA(H13+20TiB_2) increases almost continuously as the temperature increases while in the case of sMM-H13 and sMM-H13+20TiB_2 the displacement shows a clear slowdown just before 600 s (i.e. around 900 °C), as evidenced by the two plateau regions in the corresponding curves (Fig. 5a). As previously described for the 80H13 blends and the MM-samples (par. 5.1 and 5.2), in this temperature range the ferrite to austenite transformation occurs and this transformation is held to be responsible for the slower sintering rate (Pellizzari et al., 2011[1]). The absence of a plateau suggests that this transformation is much less important for MA(H13+20TiB_2). After the end of ferrite to austenite transformation, displacements restart to increase up to the maximum densification attainable by each sample (Fig. 5a). In the case of sMM-H13 this maximum densification, highlighted by a second plateau, is achieved before the end of the heating stage, at about 1020 °C. When the heating stage ends sMM-H13+20TiB_2 is approaching its maximum density and therefore the further increase of displacement in the holding stage is very small. Finally MA(H13+20TiB_2) reaches its maximum density far behind the end of the heating stage. Due to creep phenomena, this material keeps densifying during the holding stage, too, and the displacement curve flattens nearly at the end of this last stage.

The densification rate curves (Fig. 5b) better highlight these behaviours. sMM-H13 shows a minimum in the densification rate in correspondence of the ferrite to austenite transformation at 900 °C and its densification ends before the maximum sintering temperature, as shown for the MM-samples (Fig. V-27). The behaviour of sMM-H13+20TiB_2 is similar to that of sMM-H13 up to 600 s, where it shows the slowdown due to the ferrite to austenite transformation, too. After this point the densification curves of the two samples start to differ: sMM-H13+20TiB_2 presents a wider minimum and after it its densification rate shows the second relative maximum later, which means at higher temperature (1050 °C) and then it slowly goes back to zero during the holding stage. The curve of MA(H13+20TiB_2) is even different. It does show a shallow minimum around 600 s meaning that the ferrite to austenite

transformation still has an influence on sintering of this material, but less intense than in the other samples. Then MA(H13+20TiB$_2$) densification curve shows a wide relative maximum as if sintering proceeds at a constant rate. After this MA(H13+20TiB$_2$) densification rate constantly decreases until the end of the holding stage.

These results highlight that the addition of the hard TiB$_2$ changes the sintering kinetics in the composite materials. TiB$_2$ shifts the end of the sintering peak towards longer time meaning that the composite material requires higher temperature to be sintered.
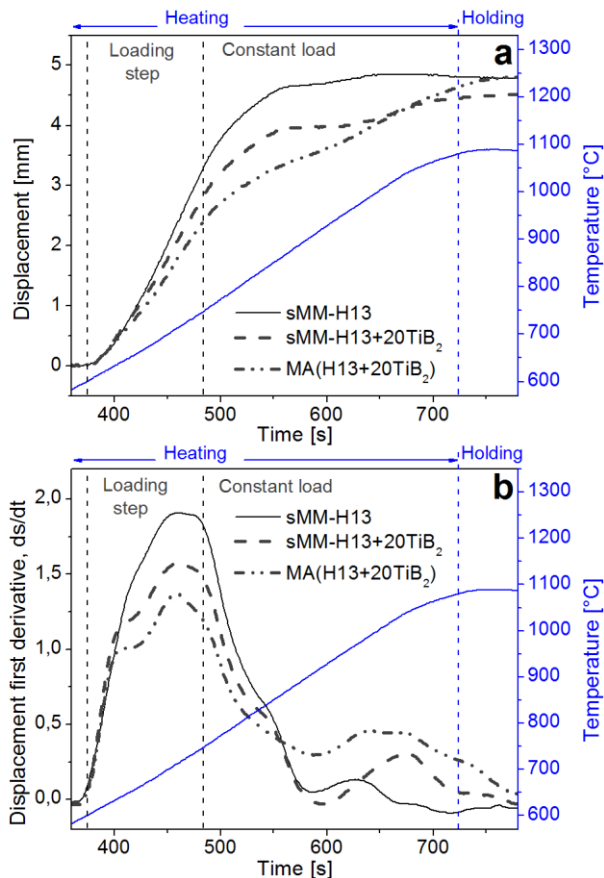
Figure VI – 5. Displacements of the lower punch (a) and its first derivative (ds/dT) (b) during the SPS cycle of sMM-H13, sMM-H13+20TiB$_2$ and MA(H13+20TiB$_2$).

Absolute and relative density data are listed in Table 1. Considering the displacement curves (Fig. 5) it is possible to see that relative density is proportional to the final displacement, i.e. higher is the final displacement higher is the relative density. This is because the three powders are characterized by very similar values of tap density, which is the apparent density of the starting powder when is poured into the die. Therefore the starting height of the lower punch, i.e. the zero point of displacement, is the same for all the samples. The relative density of sMM-H13 is 99.10% after sintering at 1100 °C for 1 minute, meaning that this material achieves near full density. The addition of 20%vol TiB_2 in sMM-H13+20TiB_2 causes a severe drop of density (96.41%). The reason is quite evident from Figure 6b where big pores (black areas) can be detected in the middle of large aggregates of TiB_2 particles (particles A). Porosity can be ascribed to an unfavourable PSR, i.e. the ratio between mean particle size of steel and TiB_2 ($d_{sMM-H13}$/d_{TiB2}) (Bonnenfant et al., 1998; Bouvard, 2000; Delie et al., 1998). In present case PSR is equal to 4.92 ($d_{sMM-H13}$=59 µm, d_{TiB2}=12 µm), i.e. above the percolation threshold (Fig. V-6) (Bouvard, 2000). The study of MM of AISI H13 has shown that the particle size can be further reduced up to 14.6 µm by milling for 1000 minutes with BPR equal to 10 (Fig. V-17). Using the fraction of this powder smaller than 25 µm only (i.e. 12.8 µm of mean particle size) and mixing it with 20%vol of TiB_2 a new sample has been produced having PSR reduced to 1.06. Relative density could be increased up to 98.53% but the formation of TiB_2 aggregates could not be avoided. These results confirm that the particle size of AISI H13 is the limiting factor for producing fully dense MMC by powder mixing. It is difficult to further reduce the steel particle size and therefore the PRS. This means that it is difficult to avoid aggregates formation and thus to increase relative density by powder mixing. On the other side, the addition of 20%vol TiB_2 is not so detrimental for the densification of MA(H13+20TiB_2) which achieves very high relative density (99.24%). In this material the limit of PSR has been overcome by MA which induces an even dispersion of fine hard TiB_2 fragments into the parent steel particles (Fig. 3b) avoiding the formation of agglomerates during sintering. This assures the achievement of high relative density.

Table VI – 1. Density and relative density of sintered samples.

Samples	Density [g/cm^3]	Relative density [%]
sMM-H13	7.69	99.10
sMM-H13+20TiB_2	6.84	96.56
MA(H13+20TiB_2)	7.03	99.24

The microstructures of the sintered samples are shown in Figure 6. sMM-H13 (Fig. 6a) has fine grain size and no pores can be seen confirming that this material is fully dense. Higher magnification image (Fig. 7a) shows the presence of small globular carbides placed both at the grain boundary and inside the grains. This

image also highlights that the grain size is not uniform, plausibly due to a not fully optimized MM process (Fig. 3a), as shown for MM-M3:2 (par. 5.2).

As previously stated, in sMM-H13+20TiB$_2$ the unfavourable PSR leads to the formation of aggregates of TiB$_2$ particles (particles A in Fig. 6b), which enclose big pores. Moreover, compared to that of sMM-H13, the microstructure of the AISI H13 matrix has changed. Grain size is much bigger in sMM-H13+20TiB$_2$ and coarse precipitates (particles B in Fig. 6b) can be found at the grain boundary. These precipitates are better shown in Figure 7b, where it is also possible to identify the formation of a different phase around the TiB$_2$ particles, highlighted by the presence of a thin layer with different colour in the SEM micrograph. This means that during sintering there is an interaction between steel and TiB$_2$. The grain growth and the formation of coarse precipitates suggest that at the steel particle surface there is a local overheating. It is known that during SPS the current causes an overheating of several hundred degrees at the particles contact points (Diouf et al., 2012; Song et al., 2006). According to the proposed model the overheated layer in the neck region can be few micrometers thick. Probably the presence of TiB$_2$ particles at these contact points may change the thermal conductivity and heat capacity of the material. Therefore it is plausible that the heat generated at the necks is mainly dissipated through the steel particles, resulting in a higher heat supply in the steel particles in the composite sample than in sMM-H13. The coarse grains, which can also be seen at the particle care, can be a piece of evidence of this higher heating in sMM-H13+20TiB$_2$.

Two main constituents can be seen iln the MA(H13+20TiB$_2$) microstructure (Fig. 6c): a composite area (A) in which pure AISI H13 steel particles (areas B) are embedded. The low signal of Ti in the light areas by EDXS analysis (Fig. 8c) has confirmed that these areas are made of pure steel. The bright particles in these areas have been identified as chromium carbides by spot EDXS analysis. The composite areas are constituted by steel (high signal of Fe as shown in Fig. 8b) with smaller carbides and uniformly distributed TiB$_2$ small particles (black spots in SEM micrographs, highlighted by intense Ti signal in Fig. 8c). As shown for the MA(H13+20TiB$_2$) powder (Fig. 3b), this microstructure arises from a not optimized MA process. However, compared to sMM-H13+20TiB$_2$, the dispersion of the hard TiB$_2$ particles during MA prevents the formation of aggregates allowing the material to be sintered to high density.
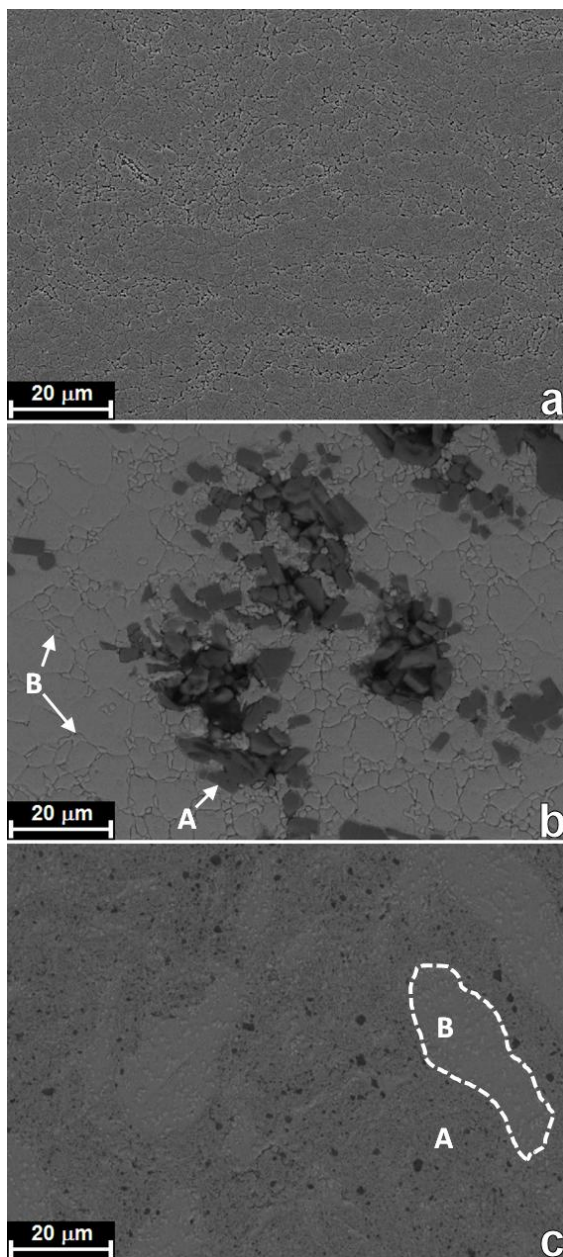
Figure VI – 6. SEM micrograph of the microstructure of sintered samples: sMM-H13 (a), sMM-H13+20TiB$_2$ (b) and MA(H13+20TiB$_2$) (c).
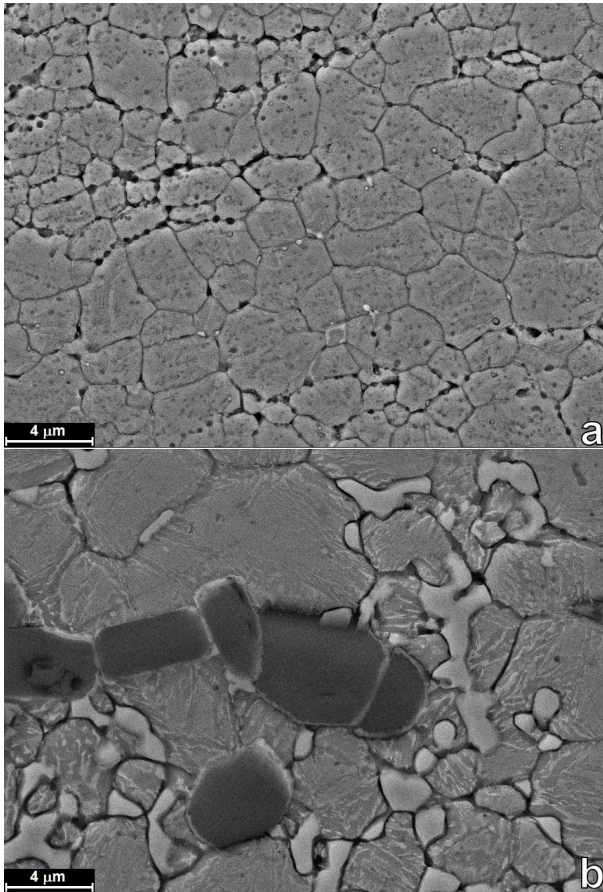
Figure VI – 7. Higher magnification SEM micrograph of the microstructure of sintered samples: sMM-H13 (a) and sMM-H13+20TiB$_2$ (b).
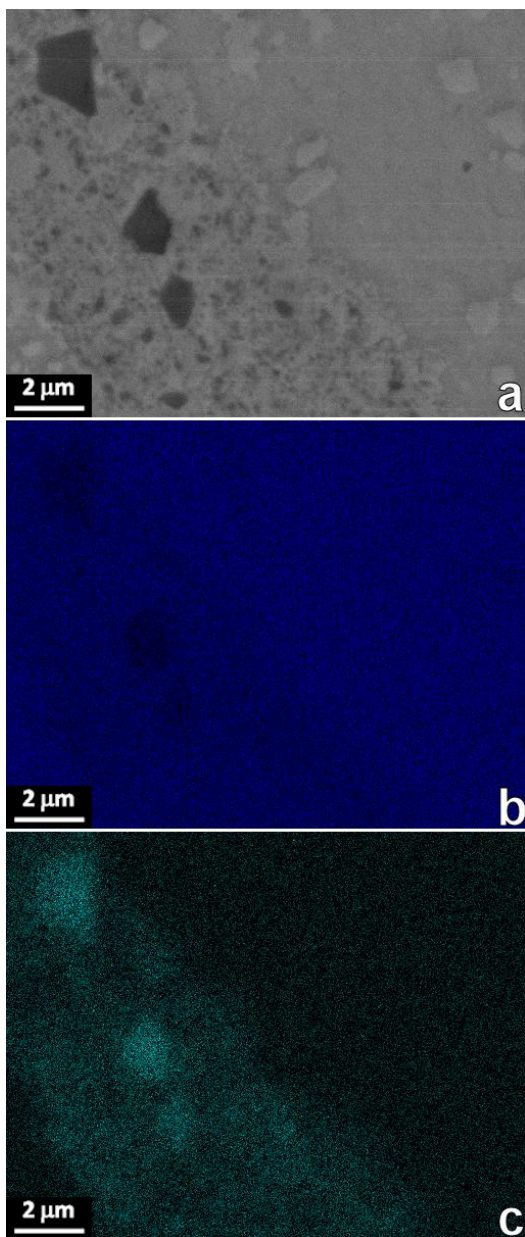
Figure VI – 8. SEM micrograph of the MA(H13+20TiB$_2$) microstructure (a) and the element distribution maps by EDXS analysis for iron (b) and titanium (c) (adapted from Fedrizzi et al., 2013[2]).

6.2.1   TiB$_2$ and AISI H13 interaction

The above microstructures have highlighted the occurrence of some interactions between TiB$_2$ and AISI H13 steel during SPS (Fig. 7b). Further investigations have been carried out to better understand these phenomena.

Figure 9 shows the XRD spectra for the three sintered materials. The XRD pattern of sMM-H13 evidences the presence of ferrite, (Fe,Cr)$_3$C carbides and retained austenite (Fig. 9a). The XRD patterns for the two TiB$_2$ reinforced steels are more complex. The sMM-H13+20TiB$_2$ spectrum (Fig. 9b) shows the signals of the same phases detected in sMM-H13 (Fe-α, (Fe,Cr)$_3$C and Fe-γ) together with the peaks of TiB$_2$ and also traces of new phases (TiC and Fe$_2$B). The presence of these new compounds confirms that during SPS the steel interacts with the TiB$_2$ particles, as shown in Figure 7b and as it was stated in other works (Degnan et al., 2002; Li et al., 2010; Sigl et al., 1991; Tanaka et al., 1999). For MA(H13+20TiB$_2$) the XRD pattern is even different (Fig. 9c). In this case the peaks are attributed to ferrite, TiB$_2$, Fe$_2$B, TiC and oxides. There are no peaks pertaining to austenite. In this sample the peaks of TiB$_2$ are weaker than in the case of sMM-H13+20TiB$_2$ whereas peaks related to TiC and Fe$_2$B are more intense. The quantitative analysis confirms that the volume fraction of TiB$_2$ decreased to 15.9% while 4%vol of TiC and 9.3%vol of Fe$_2$B have been formed. This result supports the partial dissolution of TiB$_2$ particles in favour of new and more thermodynamically stable compounds. The MA(H13+20TiB$_2$) pattern shows also some peaks related to oxides, which confirms the higher tendency of MM powder towards oxidation and the oxygen-induced Fe$_2$B formation (Tanaka et al., 1999).
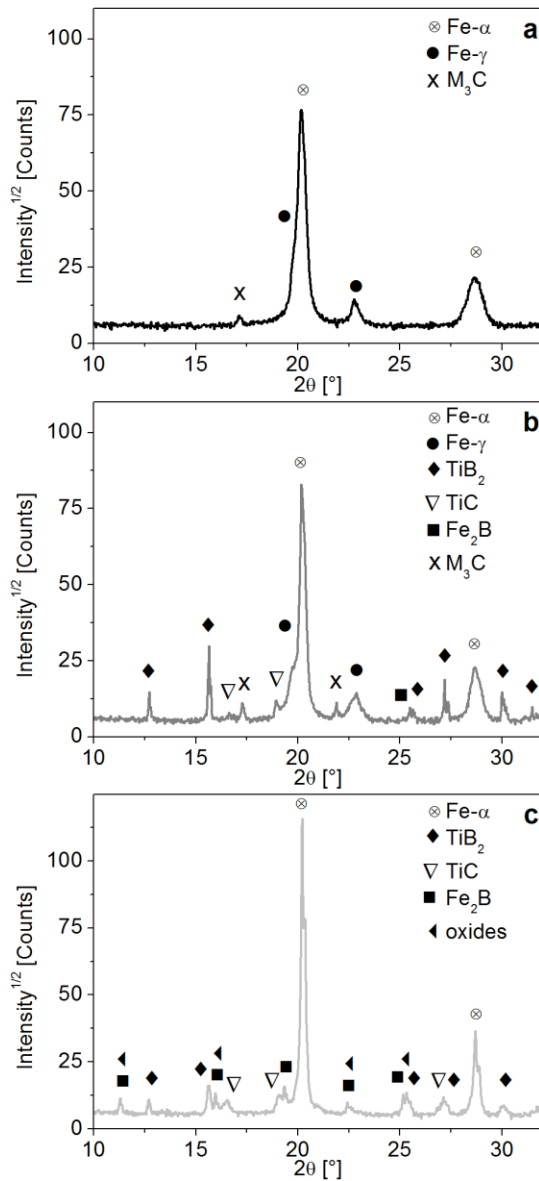
Figure VI – 9. XRD patterns of the sintered samples: sMM-H13 (a), sMM-H13+20TiB$_2$ (b) and MA(H13+20TiB$_2$) (c) (adapted from Fedrizzi et al., 2013[2]).

To evaluate the equilibrium conditions for the studied system, thermodynamic calculations have been carried out. The diagram in Figure 10 represents an isopleth of the AISI H13 (Fe-C-Cr-Mn-Si-V-Mo)-TiB$_2$ equilibrium diagram (according to the composition in Tab. IV-1 and 4) calculated by the Thermo-Calc® software using the TCFe3 database (Sundman et al., 1985). The author is conscious that the materials studied in this work are well far away from equilibrium conditions, but thermodynamic calculations are useful to determine in which way the system would evolve, according to energy-based conditions. For a system containing about 20%vol TiB$_2$ (i.e. Mole fraction B = 0.17) at the sintering temperature of 1100 °C, the model predicts ferrite, Fe$_2$B, TiB$_2$ and TiC as stable phases. The ferrite to austenite transformation is shifted to much higher temperature than that measured in pure AISI H13 (about 820 °C, according to dilatometric test in Fig. V-26).
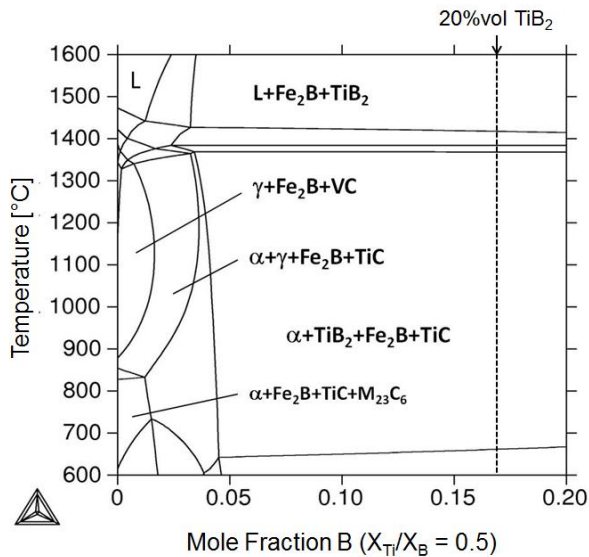
Figure VI – 10. H13-TiB$_2$ pseudobinary equilibrium phase diagram (adapted from Fedrizzi et al., 2013[2]).

The presence of Fe$_2$B and TiC peaks in the spectra of the composite samples (Fig. 9b,c) confirms the tendency of the system to move towards the equilibrium conditions. The reaction occurs at the interface between steel and TiB$_2$ particles, where the microstructural analysis highlighted the formation of a different phase (Fig. 7b). The refinement and the fine dispersion of the TiB$_2$ particles during MA have resulted in a considerable increase of the interface between steel and TiB$_2$ in MA(H13+20TiB$_2$). Thus this material has a much higher driving force for the reaction

and the XRD analysis shows more intense peaks for Fe_2B and TiC. Moreover the absence of austenite in the MA(H13+20TiB$_2$) XRD spectrum confirms the inhibition of the ferrite to austenite transformation during sintering. All these evidences confirm that during sintering the steel matrix and the TiB$_2$ particles strongly interact, in spite of the high heating rate and low holding time at elevated temperature made possible by SPS.

As proposed by Sigl et al. (1991) for a TiB$_2$-Fe system with carbon present as impurity, the plausible reaction that occurs during heating at the interface between TiB$_2$ and steel is given in the follow:

$$TiB_2 + \alpha\text{-}Fe_{(\uparrow C)} \rightarrow TiC + Fe_2B + \alpha\text{-}Fe_{(\downarrow C)} \qquad (5)$$
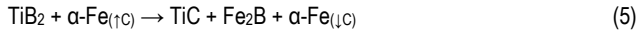
The TiB$_2$ particles react with the iron rich in carbon of the steel matrix producing TiC, Fe_2B and a ferrite with a lower amount of dissolved carbon. This ferrite, due to the lower carbon content, is more stable therefore the ferrite to austenite transformation is shifted to higher temperature and it concerns only the areas of pure AISI H13. All austenite is completely transformed into ferrite again after cooling. DSC measurements carried out on the powders have confirmed this assumption. As shown in Figure 11, the DSC curves during heating for all the three powders present the exothermic peak related to the carbide precipitation at 684 °C and the endothermic signal at the Curie's temperature (764 °C). At 877° C both sMM-H13 and sMM-H13+20TiB$_2$ powders show the endothermic peak related to the ferrite to austenite transformation, not present in the MA(H13+20TiB$_2$) curve. In MA(H13+20TiB$_2$) there is a weak endothermic signal at 1017 °C meaning that some ferrite to austenite transformation may occur, but at higher temperature, and it concerns only a small fraction of the material.
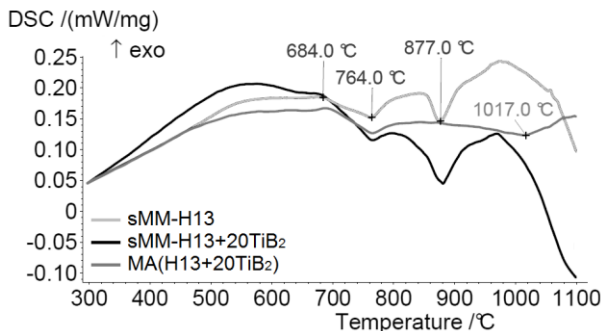
Figure VI – 11. DSC curves during heating for sMM-H13, sMM-H13+20TiB$_2$ and MA(H13+20TiB$_2$) powders (adapted from Fedrizzi et al., 2013[2]).

As stated at the beginning of this paragraph, the interaction between TiB$_2$ and steel has been firstly evidenced by microstructural analysis of sMM-H13+20TiB$_2$ (Fig. 7b). Thus deeper investigations have been carried out on this sample by means of

AFM and TEM. Figure 12 shows an AFM topographic map, a SKPFM Volta potential map and SEM micrographs for the sMM-H13+20TiB$_2$ sample. As previously shown by SEM analysis, too (Fig. 6b), the topographic map (Fig. 12a) highlights the presence of some pores (dark areas) in between the TiB$_2$ aggregates. The HPs are higher (lighter colour) than the matrix because during polishing they are less abraded due to their higher hardness. The Volta potential map (Fig. 12b) indicates that TiB$_2$ particles are characterized by a higher potential (about 50 mV) than the steel matrix. In the steel matrix this map also reveals the presence of some small precipitates which show a lower potential (darker colour) than the matrix. These precipitates are small secondary carbides, which are visible by SEM only at higher magnification (Fig. 7). Before chemical etching the SEM image (Fig. 12c) shows the HP distribution, confirming that the higher potential areas are made by TiB$_2$, and it highlights again the presence of a reaction layer around the TiB$_2$ particles. The chemical etching reveals the presence of the big precipitates at the steel grain boundary (Fig. 12d). These particles were displayed neither by AFM topographic analysis nor by SKPFM Volta potential. TEM investigations on these precipitates (Fig. 13) have revealed that they are rich in boron, vanadium, chromium, iron and molybdenum (Tab. 2). This result suggests that during SPS the boron coming from the decomposition of the TiB$_2$ particles can promote the formation of these compounds with complex composition, which can be responsible for the Fe$_2$B signal in the XRD analysis. The layer surrounding TiB$_2$ particles has been deeper investigated by TEM, too. In Figure 14a it is possible to see a TiB$_2$ particle and the reaction layer (darker border). EDXS analysis on this reaction layer shows the presence of carbon, titanium, vanadium, and iron, mainly (Tab. 3). This result suggests that the reaction layer can be composed by complex MC-carbide containing Ti and V. TEM analysis on the MA(H13+20TiB$_2$) has also evidenced the presence of small precipitates (Fig. 15) rich in carbon and titanium (Tab. 4). These precipitates are the products of the chemical interaction between TiB$_2$ and steel.
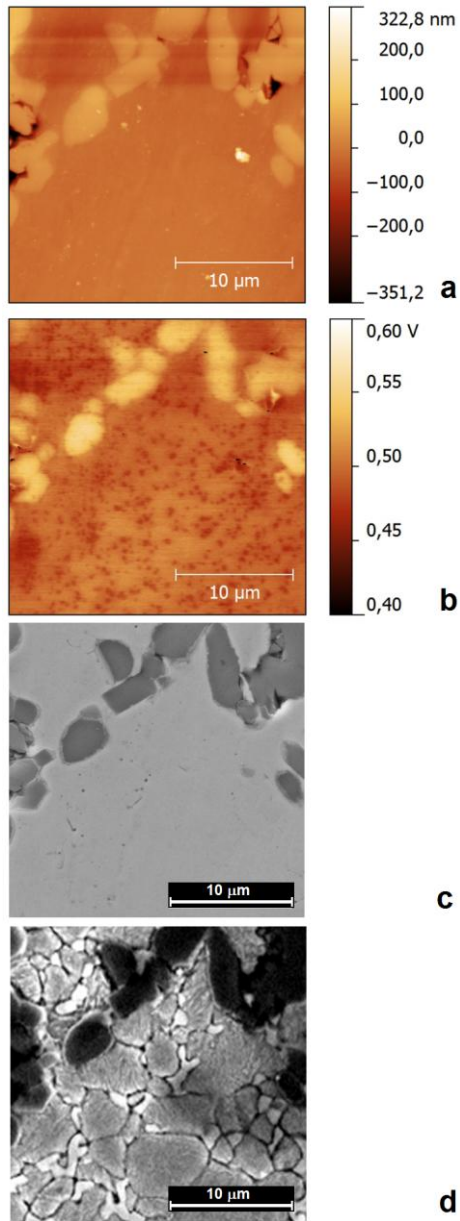
Figure VI – 12. AFM topographic map (a), SKPFM Volta potential map (b) and SEM micrograph before etching (c) and after chemical etching (d) of the sMM-H13+20TiB$_2$ sample (adapted from Fedrizzi et al., 2013[2]).
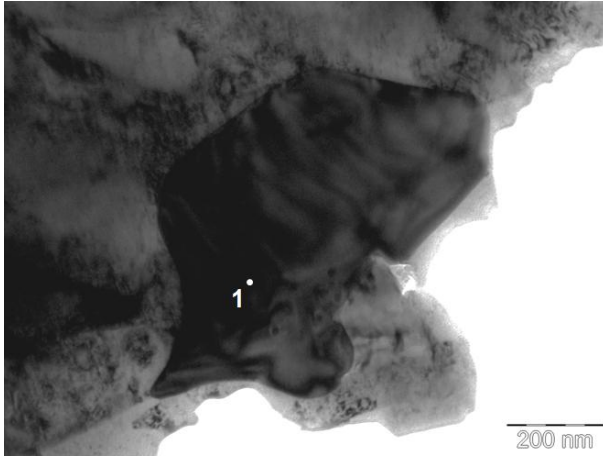
Figure VI – 13. TEM image of a precipitate in sMM-H13+20TiB$_2$.

Table VI – 2. EDXS localized analysis results [wt%] on the spot 1 in Fig. 13.

B	C	Si	Ti	V	Cr	Fe	Mo
15.8		0.7	3.3	12.5	12.5	31.9	23.4
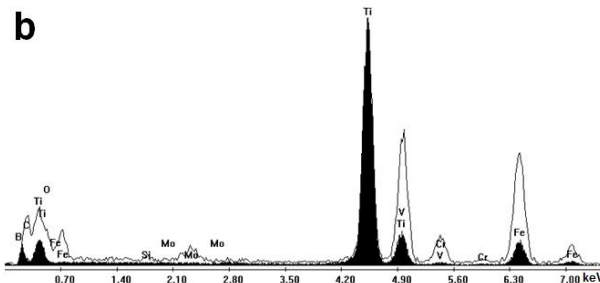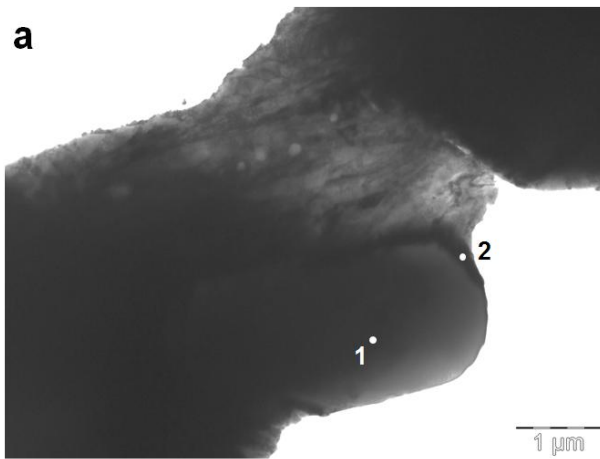
Figure VI – 14. TEM micrograph (a) of a TiB$_2$ particle in sMM-H13+20TiB$_2$ and EDXS spectra (b) for spot 1 (black area) and spot 2 (solid line).

Table VI – 3. EDXS localized analysis results [wt%] on the marked spots in Fig. 14a.

Analysis	B	C	Ti	V	Cr	Fe	Mo
Spot 1	38.9	-	53.9	-	0.4	6.8	-
Spot 2	-	10.3	41.1	16.9	2.9	25.1	3.8

Figure VI – 15. TEM image of MA(H13+20TiB$_2$).

Table VI – 4. EDXS localized analysis results [wt%] on the spot 1 in Fig. 15.

C	O	Si	Ti	V	Cr	Fe	Mo
12.1	7.2	0.7	48.9	1.7	1.5	24.5	3.4

6.2.2   Conclusions

Powder mixing and mechanical alloying techniques for producing HWTS based MMCs have been compared.

Investigations on the material densification during SPS have pointed out that the addition of the hard TiB$_2$ particles changes the sintering kinetics in the composite materials. The end of the sintering peak is shifted later in time meaning that the composite material requires higher temperature to sinter than the pure AISI H13. The mixed sample (i.e. sMM-H13+20TiB$_2$) shows little difference in sintering kinetics but it is the least dense one. MA amplifies the influence of TiB$_2$ on sintering: MA(H13+20TiB$_2$) sample shows only a slight slowdown in sintering rate in the range of ferrite to austenite transformation and it densifies during the holding stage, too, reaching full density only at the end of the sintering cycles.

Microstructure investigations have shown the formation of big TiB$_2$ aggregates in the sMM-H13+20TiB$_2$ sample. These aggregates, which enclose large pores, result from an unfavourable PSR and they cause poor densification. Results pointed out that the AISI H13 particle size is the limiting factor for producing fully dense MMC by powder mixing. It has been proved difficult to further reduce the steel particle size and therefore the PRS. This means that it is difficult to avoid aggregates formation and thus to increase relative density by powder mixing.

Problems related to the PSR have been overcome by MA which promotes a uniform dispersion of TiB_2 fragments into the parent steel particles avoiding the formation of agglomerates during sintering. This assures the achievement of high relative density. It can be stated that MA is a well suited technology for the production of MMC.

Microstructural characterization have highlighted the formation of TiC and Fe_2B in the sintered composites, meaning that TiB_2 and steel react during sintering. This phenomenon is more intense in the $MA(H13+20TiB_2)$ sample in view of the larger surface area of finely dispersed HPs which can react much easier with the steel matrix. These results clearly point out that the carbon, which is present in the steel matrix, destabilizes TiB_2 allowing the formation of new compounds.

6.3 TiC and TiN – MMCs: Improved Chemical Stability

The interaction between TiB_2 and H13 makes this compound not suitable for the production of HWTS based MMCs. Therefore two different compounds, i.e. TiC and TiN, have been considered. In order to predict their stability when sintered with AISI H13, equilibrium phase diagrams were calculated by Thermo-Calc® (Fig. 16). The diagrams show that both compounds are stable in AISI H13. Indeed for temperature higher than 900 °C the thermodynamic calculations give only austenite and the corresponding ceramic compound as stable phases. At low temperature (200 °C) the H13-TiC diagram (Fig. 16a) shows the presence of ferrite, TiC and the typical carbides found in AISI H13 (i.e. $M_{23}C_6$ and M_6C). Similar results have been found for the H13-TiN system (Fig. 16b), where at 200 °C the stable phases are ferrite, TiN, $M_{23}C_6$, M_6C and VN. In this case the presence of VN may imply a partial decomposition of TiN. Equilibrium calculation shows that the volume fraction of TiN at room temperature is 19.5%, meaning that any eventual formation of VN would be only moderate and that TiN can be assumed to be chemically stable in AISI H13. Thus, the equilibrium phase diagrams suggest that no reactions should occur for both systems during SPS and this makes TiC and TiN suitable reinforcements for the development of HWTS based MMCs.
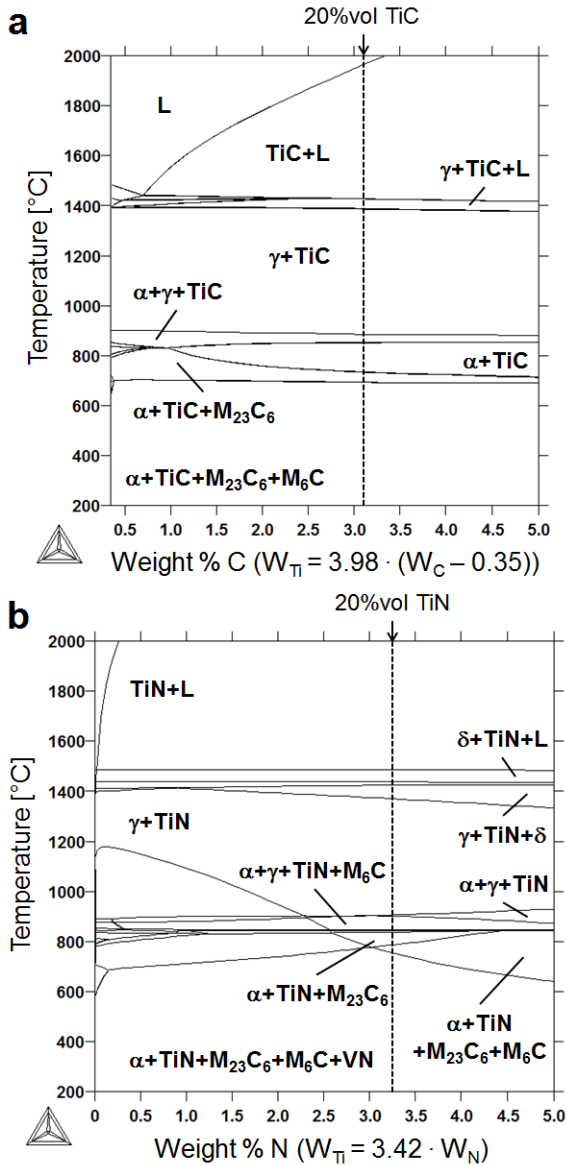
Figure VI – 16. H13-TiC (a) and H13-TiN (b) pseudobinary equilibrium phase diagrams.

Two samples containing 20%vol of reinforcement, MA(H13+20TiC) and MA(H13+20TiN), were sintered. First of all densification during sintering has been

investigated. The punch displacements and their derivatives are shown in Figure 17. Data for sMM-H13 and MA(H13+20TiB$_2$) samples are also plotted for comparison (see par. 6.2). The displacement of MA(H13+20TiC) and MA(H13+20TiN) is always lower than MA(H13+20TiB$_2$) (Fig. 17a), meaning that these two new powders are less compressible and more difficult to be sintered. During the loading step the displacement in MA(H13+20TiC) and MA(H13+20TiN) is almost coincident and increases linearly. As previously stated (par. 6.2), in the second stage the densification increases at a lower rate. This deceleration is higher in MA(H13+20TiN). At nearly 600 s, MA(H13+20TiC) and MA(H13+20TiN) present the slowdown related to the ferrite to austenite transformation (around 900 °C), which is less evident in MA(H13+20TiB$_2$). All the three MA-samples reach their maximum displacement at the end of the holding step, meaning that sintering has not been completed during the heating stage.

The curves of the densification rate (Fig. 17b) underline the occurrence of the ferrite to austenite transformation in MA(H13+20TiC) and MA(H13+20TiN). Both samples present a deep minimum quite similar to that of sMM-H13 (dashed line). Compared to the pure steel, the addition of HPs shifts the second densification rate peak later in time for all the MA-samples. MA(H13+20TiN) is characterized by the lowest peak, meaning that this sample has the highest resistance to densification. For MA(H13+20TiC) the second peak occurs at about 700 s, nearly at the end of the heating stage denoting that this composite requires the highest temperature to sinter.
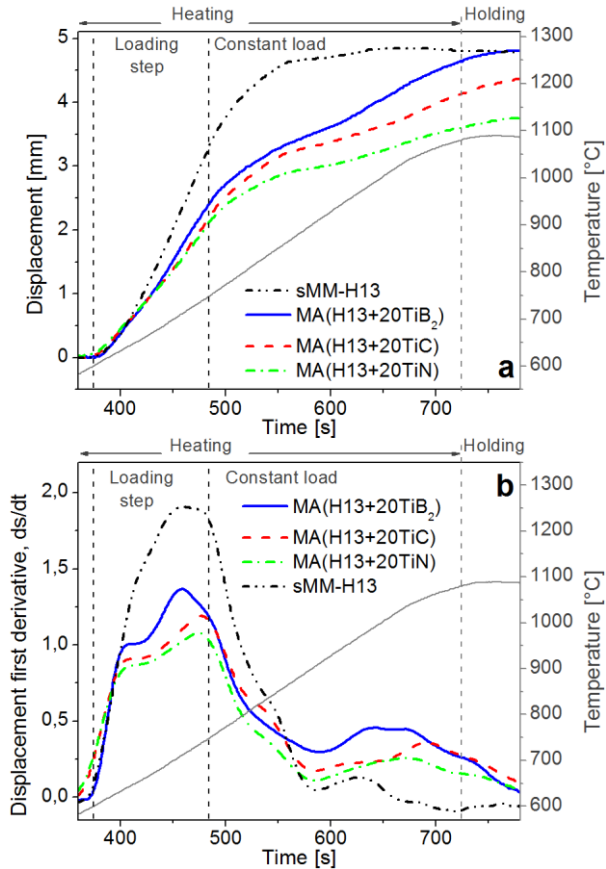
Figure VI – 17. Displacements of the lower punch (a) and its first derivative (ds/dT) (b) during the SPS cycle of sMM-H13 and MA-samples.

The absolute and relative density values are listed in Table 5. As well as for previous samples (par. 6.2), relative density values are proportional to the final displacement. The new samples show high porosity, particularly MA(H13+20TiN) whose relative density is only 87.86%. It has to be recalled that MA(H13+20TiB$_2$), which shows the highest displacement, reaches nearly full density (Tab. 1).

The sintered sample microstructures (Fig. 18) confirm density results. MA(H13+20TiN) (Fig. 18b) has a large amount of irregular and interconnected pores and powder particles show few contact points where sintering has happened. MA(H13+20TiC) (Fig. 18a) also has big pores but they are fewer and less interconnected than in MA(H13+20TiN).

As discussed in paragraph 6.1, the not fully optimized MA process is the cause of composite powders having nonhomogeneous HP distribution. The sintered materials still show this uneven microstructure (Fig. 18). As shown for MA(H13+20TiB$_2$) (Fig. 6c), the MA-samples microstructures are formed by two main components: a composite constituent and some pure AISI H13 areas. Due to the bigger size of the starting powder (par. 4.2.1), TiB$_2$ fragments are clearly displayed in the composite phase of MA(H13+20TiB$_2$) (Fig. 6c), whereas TiC and TiN particles have become too small to be detectable (Fig. 18).
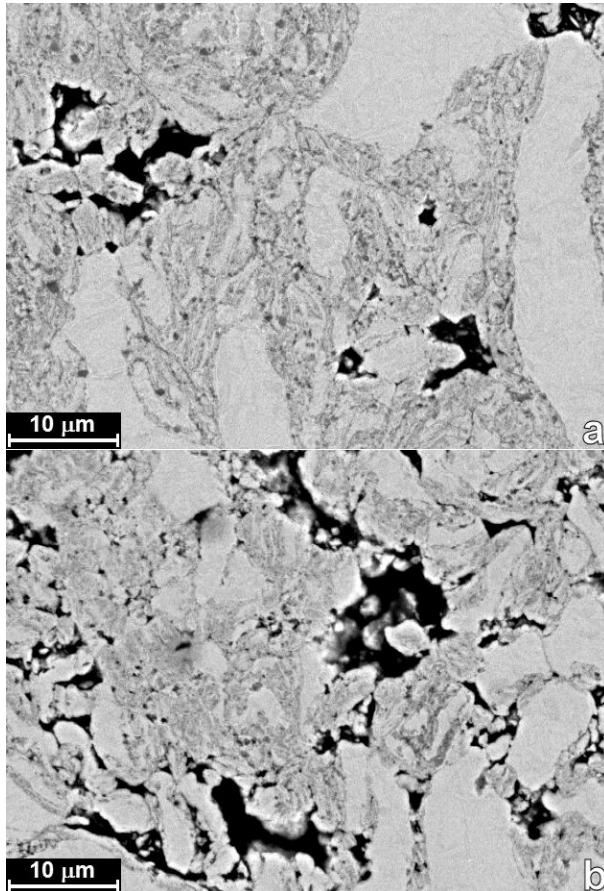
Figure VI – 18. SEM micrograph of the microstructure of sintered samples: MA(H13+20TiC) (a) and MA(H13+20TiN) (b) (adapted from Fedrizzi et al., 2013[1]).

Table VI – 5. Density and relative density of sintered samples.

Samples	Density [g/cm³]	Relative density [%]
MA(H13+20TiC)	6.59	91.58
MA(H13+20TiN)	6.37	87.86

XRD patterns for MA(H13+20TiC) and MA(H13+20TiN) after sintering are shown in Figure 19. These patterns are quite similar, they both show peaks related to ferrite (Fe-α), austenite (Fe-γ) and their ceramic reinforcement, i.e. TiC and TiN, respectively. Compared to the original powder (Fig. 4c,d), after SPS the austenite signal has appeared, as it happens for sMM-H13 (Fig. 9a). During sintering the composite powders are heated up to 1100 °C, where austenite is the stable phase for the steel matrix, as previously shown in the equilibrium phase diagrams (Fig. 16). Due to the fast cooling rate, austenite does not completely transform into martensite and some retained austenite remains in the sintered composites. The quantitative analysis has determined that the retained austenite volume fraction is about 4% and 5.6% for MA(H13+20TiC) and MA(H13+20TiN), respectively, and the ceramic content is about the same that it has been found in the composite powders. The unchanged volume fraction of HPs and the absence of signals related to new phases suggest that TiC and TiN do not react with the AISI H13 matrix. These results are in good agreement with thermodynamic calculations and they confirm the good chemical and thermal stability of TiC and TiN in steel matrix (Akhtar, 2008; Ma et al., 2012; Pagounis et al., 1998).
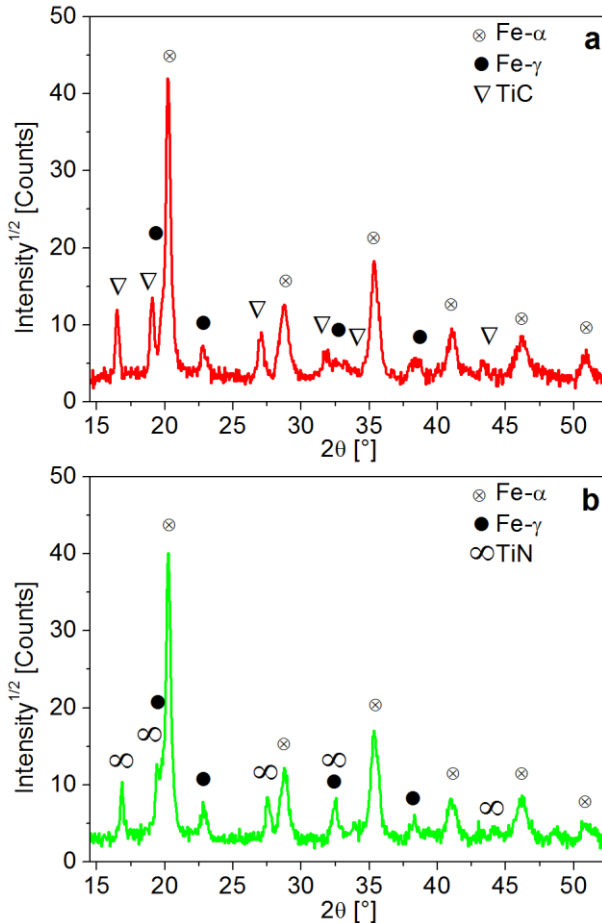
Figure VI – 19. XRD patterns of sintered MA(H13+20TiC) (a) and MA(H13+20TiN) (b) (adapted from Fedrizzi et al., 2013[1]).

The hardness of the MA-samples is listed in Table 6. For comparison sMM-H13 and MA(H13+20TiB$_2$) data are also reported. MA(H13+20TiC) is the hardest among the MA-samples while the hardness of MA(H13+20TiN) is the lowest. It is possible to see that all MA-samples are softer than sMM-H13. It is well known that porosity effects hardness (Abderrazak et al., 2011; Adachi et al., 2006; Luo et al., 1999; Pellizzari et al., 2011[1]; Xu et al., 2009). The high porosity of MA(H13+20TiC) and MA(H13+20TiN) causes the severe drop of their hardness, thwarting the strengthening of the HP addition.

Due to the uneven microstructure of the MA-samples, their hardness values result from the combination of the hardness of composite areas and that of the pure AISI H13 particles. Microhardness ($HV_{0.05}$) of these constituents has been measured and the results are listed in Table 6. Microhardness of the composite areas highlights that TiC has the highest hardening effect. TiN also increases steel microhardness, compared to the sMM-H13 value. On the other hand the composite areas in MA(H13+20TiB$_2$) are less hard than sMM-H13. Considering the steel particle microhardness, values measured in MA(H13+20TiC) and MA(H13+20TiN) are slightly lower than that of sMM-H13 but in any case they fall in the range of those of martensite. In contrast steel areas in MA(H13+20TiB$_2$) show very low microhardness, close to that characteristic of ferrite. These data confirm again that during sintering TiB$_2$ depletes carbon in the steel inhibiting martensite formation, as it has been deeply discussed in paragraph 6.2.1 and shown by the phase diagram (Fig. 10). Thus the composite areas have also a ferrite matrix which is responsible for their lower microhardness.

In the fully dense MA(H13+20TiB$_2$) hardness value is close to the combination of microhardness of the composite consituent and of steel particles. On the other hand hardness of MA(H13+20TiC) and MA(H13+20TiN) is much lower than the average microhardness. This decreased hardness is caused by the high porosity of these samples.

In view of the hardness measurements it can be suggested that due to its lower hardness MA(H13+20TiB$_2$) is more easily deformed during sintering allowing the achievement of full density.

Table VI – 6. Hardness and microhardness of sintered samples.

Samples	Hardness [HV10]	Microhardness [$HV_{0.05}$]	
		Composite phase	Steel areas
sMM-H13	759 ± 3	-	830.5 ± 21.4
MA(H13+20TiB$_2$)	459 ± 7	689.7 ± 55.1	268.0 ± 6.5
MA(H13+20TiC)	533 ± 23	1097.9 ± 43.3	719.4 ± 8.3
MA(H13+20TiN)	384 ± 19	961.4 ± 46.7	648.4 ± 39.5

6.3.1   Conclusions

Thermodynamic calculations have suggested that TiC and TiN are chemically stable in AISI H13 and thus they have been considered as reinforcing particles for HWTS based MMCs. The influence of the different HPs on densification, microstructure and hardness has been evaluated.

From the densification analysis during SPS, it is clear that the addition of HPs shifts the end of the densification peak later in time, meaning that generally composites require higher temperature for sintering than the pure steel matrix.

MA(H13+20TiC) and MA(H13+20TiN) are less compressible and more demanding to be sintered than MA(H13+20TiB$_2$). Indeed these two MA-samples do not achieve full density. They show high porosity content, particularly MA(H13+20TiN) relative density is the lowest.

XRD measurements point out that either TiC and TiN do not react with the AISI H13 matrix, supporting their good chemical and thermal stability in steel matrix. Microhardness measurements confirm the martensitic microstructure of the steel matrix and show that TiC has the higher hardening effect. On the other hand, hardness is negatively influenced by porosity, thwarting the hardening effect of HPs. Thus MA(H13+20TiC) and MA(H13+20TiN) hardness is lower than what expected from microhardness measurements.

This investigation points out that TiC and TiN are suitable for producing HWTS based MMCs. After sintering at 1100 °C for only 1 minute the composites materials are characterized by good microhardness, showing the hardening effect of the HPs. On the other hand their low density negatively affects the composite hardness. These results point out that SPS cycles have to be optimized in order to achieve full density and increased hardness.

6.4 TiC and TiN – MMCs: SPS Optimization

It has been shown that the addition of HPs shifts the sintering peak later in time, which means at higher temperature (Fig. 17b). Therefore firstly it has been decided to increase the sintering temperature until the end of the sintering peak. However there is a limit for the maximum sintering temperature. The surface of the sample is in contact with the graphite die and there carbon diffuses into the steel matrix. The local increase of carbon is quite high and the steel can reach the eutectic composition giving rise to the formation of liquid phase at quite low temperature (i.e. 1147 °C for pure Fe-C system). This liquid forms only at the surface of the sample and the applied pressure squeezes it out from the die. Therefore sintering has to be stopped. For present composites it has been experimentally proved that liquid phase forms at 1150-1160 °C and this small increase in the sintering temperature does not bring any remarkable improvement in the material density.

During holding step displacement curves (Fig. 17a) for MA(H13+20TiC) and MA(H13+20TiN) continuously increase. This means that densification occurs even at constant temperature due to creep phenomenon which causes material transport. The evolution of density during the holding stage has been investigated by sintering samples with holding time ranging from 1 to 30 minutes.

Figure 20 shows the displacement of the lower punch for the sample sintered for 30 minutes. As previously shown for the samples sintered for 1 minute (Fig. 17a), the displacement of MA(H13+20TiN) is always lower than that of MA(H13+20TiC). In the holding stage the displacement of MA(H13+20TiC) increases quickly in the first

minute, then the displacement rate sharply decreases. After 5 minutes the displacement still increases but at a very low rate, nearly approaching zero, and after 30 minutes the displacement is stable at its maximum. The MA(H13+20TiN) also shows a high displacement rate in the first minute of holding time, but in any case lower than that of MA(H13+20TiC). Then the displacement continuously increases at a constant rate and after 30 minutes of holding time the displacement does not shows any plateau, meaning that the displacement rate is still higher than zero and the displacement has not reached its maximum value yet.
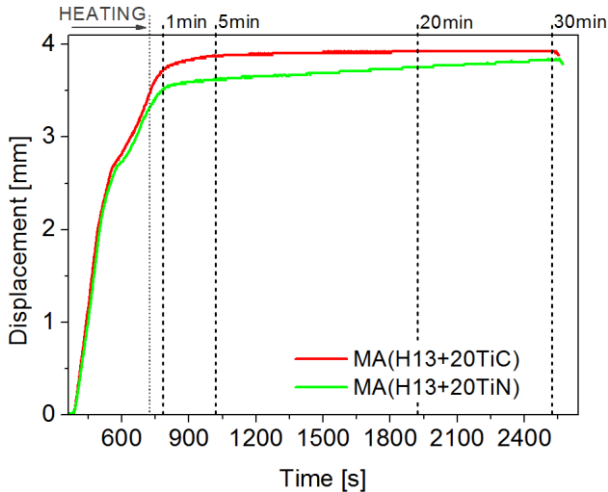
Figure VI – 20. Displacements of the lower punch during SPS cycle of MA(H13+20TiC)-30min and MA(H13+20TiN)-30min.

Relative density for MA(H13+20TiC) and MA(H13+20TiN) samples is plotted as a function of the holding time in Figure 21. The higher displacement of MA(H13+20TiC) results in higher relative density than MA(H13+20TiN). The trend of relative density is in good agreement with that of displacement. MA(H13+20TiC) relative density increases at a high rate moving from 1 to 5 minutes of holding time. Then it continuously increases but at a lower rate. After 20 minutes the densification rate is nearly equal to zero (i.e. 0.00047 min^{-1}) and MA(H13+20TiC)-30min sample reaches nearly full density (99.36%). MA(H13+20TiN) relative density increases quite fast going from 1 to 5 minutes, then it increases at a constant rate and after 30 minutes the composites is still far away from full densification showing only 94.34% relative density.

MA(H13+20TiC) density data are in good agreement with a power-law creep densification mechanism. Creep phenomena are time dependent and their effect diminishes as time increases. Olevsky et al. (2006) reported that densification is

mainly promoted by creep in the micron-sized materials, but the applied load can be the dominant factor for the final collapse of voids also in the ultrafine powders, i.e. the powder investigated in this work.

Present data for MA(H13+20TiN) follow a linear trend which may suggest that the densification mechanism acting in this material are other than power-law creep. MA(H13+20TiN) powder particle size is significantly smaller than that of MA(H13+20TiC) (Fig. 1), resulting in a higher specific surface and thus in a higher oxygen pick up after MA (Tab. 7). This thin oxide layer may have an effect on the densification mechanisms. Sintering for longer holding time can be suggested to further improve density but it has to be considered that for long sintering time SPS becomes less convenient than conventional processes, like HIP.
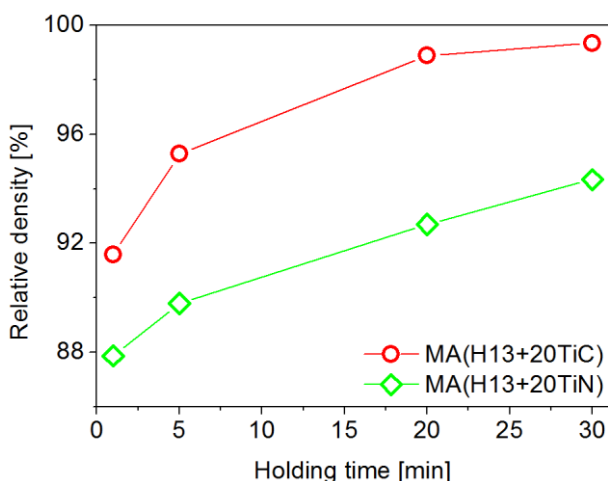
Figure VI – 21. Relative density as a function of the holding time for MA(H13+20TiC) and MA(H13+20TiN).

Table VI – 7. Oxygen content in the MA-powders [weight %].

Powder	O
MA(H13+20TiC)	0.2704
MA(H13+20TiN)	0.3137

The influence of the holding time on hardness is quite similar to that on relative density (Fig. 22). This is because hardness strongly depends on density (Adachi et al., 2006; Abderrazak et al., 2011; Luo et al., 1999; Pellizzari et al., 2011[1]; Xu et al., 2009) and thus increasing the holding time result in increased hardness. The dependency of hardness on relative density is highlighted in Figure 23. Hardness linearly increases as density increases. Porosity seems to be the dominant factor influencing hardness. Thus data for MA(H13+20TiC) and

MA(H13+20TiN) fall nearly on the same line regardless the different hardness of the two ceramic compounds.
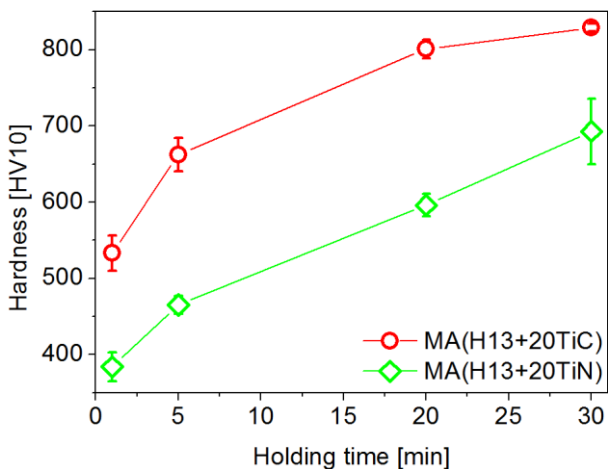
**Figure VI – 22.** Hardness as a function of the holding time for MA(H13+20TiC) and MA(H13+20TiN).
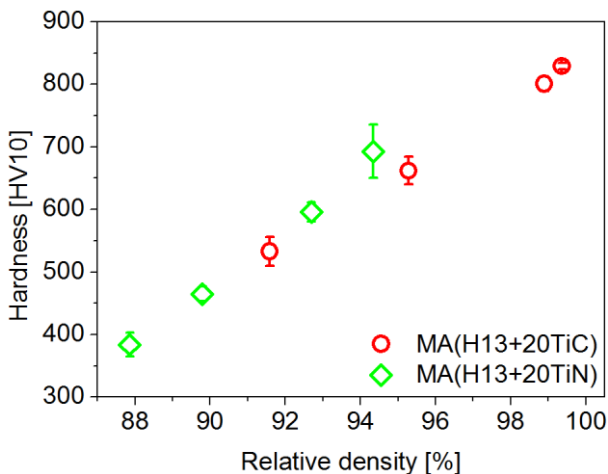
Figure VI – 23. Hardness as a function of the relative density for MA(H13+20TiC) and MA(H13+20TiN).

Figure 24 and 25 show the microstructure of MA(H13+20TiC) and MA(H13+20TiN), respectively. After sintering for 1 minute, large sintering necks have formed between most of the particles in MA(H13+20TiC) but some big isolated pores

are also present (Fig. 24a). Increasing the holding time up to 5 minutes the pores size decreases considerably (Fig. 24b) and after 30 minutes porosity has been completely close and no pores can be seen (Fig. 24c). The micrograph of MA(H13+20TiN) samples also show the reduction of porosity content by increasing the holding time (Fig. 25), but in this case pores can still be seen after sintering for 30 minutes. Generally pores in MA(H13+20TiN) samples are smaller in size that those in MA(H13+20TiC), but they are more interconnected. As a result of this elongated shape, pores surround the composite particles and thus sintering necks are smaller than in the case of MA(H13+20TiC). Small necks and interconnected porosity may suggest that sintering mechanisms could not act properly. The causes have to be deeper investigated. As previously stated it may be suggested that the oxide layer influences the diffusion mechanisms resulting in a slowdown of the sintering kinetics.
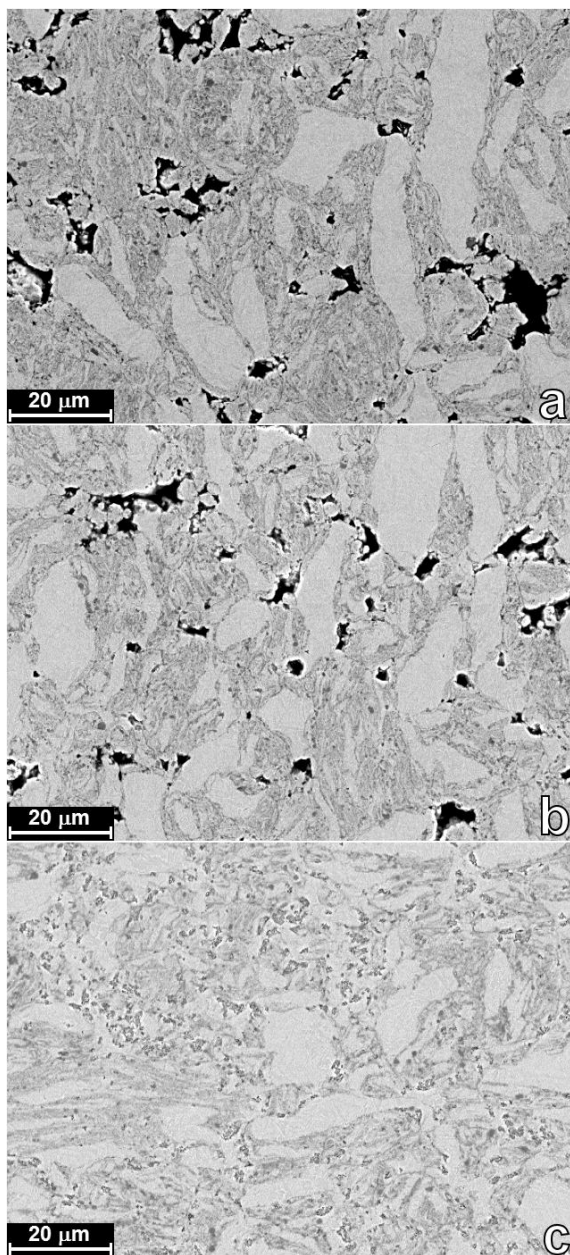
Figure VI – 24. SEM micrographs of the microstructure of MA(H13+20TiC) sintered for 1 minute (a), 5 minutes (b) and 30 minutes (c).
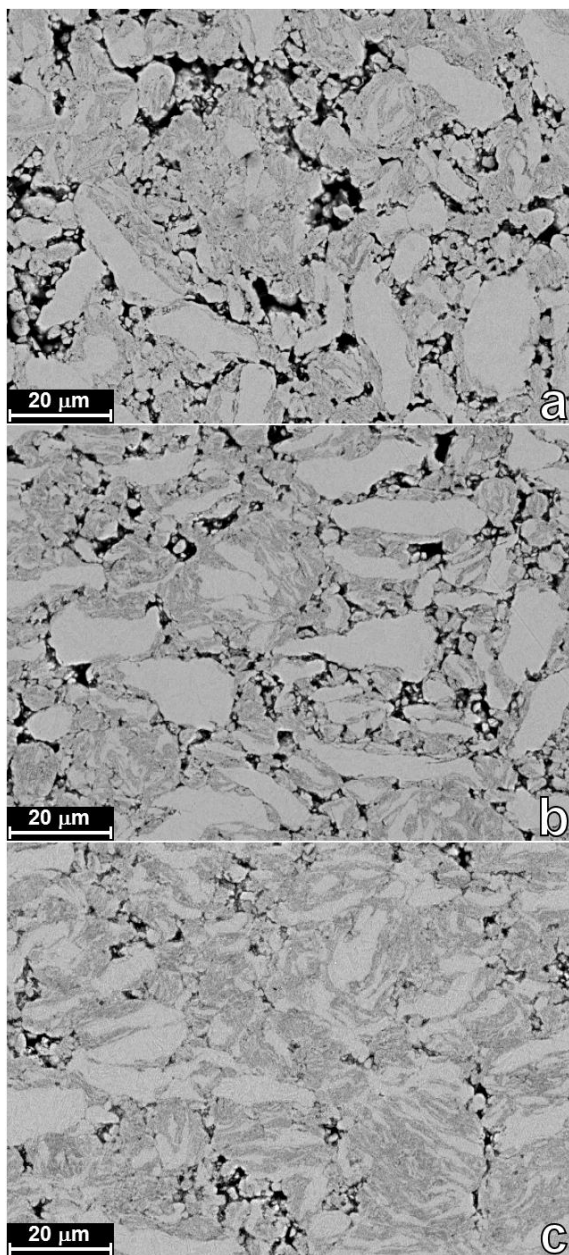
Figure VI – 25. SEM micrographs of the microstructure of MA(H13+20TiN) sintered for 1 minute (a), 5 minutes (b) and 30 minutes (c).

6.4.1   Conclusions

For sintered material higher density results in improved properties, such as higher hardness which is mandatory to guarantee wear resistance. Therefore sintering parameters have been modified in order to increase the density of TiC and TiN reinforced MMCs.

Due to the low strength of the graphite punches it is not possible to further increase the applied load and on the other hand temperature cannot be risen because of the formation of liquid phase at the sample surface. Thus investigations have been focused on the influence of the holding time on densification.

In the holding stage the composites show continuous densification, highlighting the occurrence of plastic deformation due to creep phenomena.

MA(H13+20TiC) shows a power-law creep behaviour. The displacement, and consequently the relative density, quickly increases in the early minutes of the holding stage, then the densification rate decreases and after 30 minutes the composite reaches nearly full density (99.36%).

MA(H13+20TiN) is characterized by higher resistance to densification. It shows lower densification rate than MA(H13+20TiC) in the early minutes of the holding stage. For longer holding time MA(H13+20TiN) densifies at a constant rate showing a linear dependence on time and after 30 minutes its relative density is still lower that 95%. MA(H13+20TiN) sintering seems to be influenced by densification mechanisms other than power-law creep. Microstructure investigations show interconnected porosity and small sintering necks. This may suggest that the oxide layer influences diffusion mechanisms changing the sintering kinetic.

The investigation of sintering process shows that AISI H13 composites with 20%vol of TiC can be fully densified by SPS for 30 minutes. On the other hand due to the slower sintering kinetic, AISI H13 composites with 20%vol of TiN still show porosity after 30 minutes of sintering. Longer sintering time can be considered but it has to be noticed that a strong point of SPS is the shorter processing time. If the holding time is further increased the SPS becomes less convenient than customary processes, such as HIP.

Chapter VII

Conclusions

In this PhD thesis powder metallurgy technology has been employed for the production of particle reinforced hot work tool steels (HWTSs). Particularly mechanical milling (MM) and mechanical alloying (MA) have been considered for the powder production and innovative Spark plasma Sintering (SPS) for the consolidation. The milling process refines both microstructure and powder particle size and promotes a more uniform distribution of the hard phase, resulting in increased strength and enhanced sintering and densification. On the other hand SPS allows sintering at lower temperature and in a shorter time comparing to customary processes. Indeed the high heating rate peculiar of SPS preserves the fine microstructure produced by MM and reduces the interaction between the metal matrix and the reinforcing particles.

As reinforcement a harder high speed steel (HSS) and different ceramic powders (TiB_2, TiC, and TiN) have been selected in order to produce Hybrid Tool Steels and Metal Matrix Composites (MMCs), respectively.

7.1   Hybrid Tool Steels

The first part of the research has been focused on the investigation of the advantages deriving from MM on the densification and the mechanical properties of HWTS/HSS blends. The following main results have been found:

- The co-sintering behaviour of HWTS/HSS blends has highlighted the negative interaction of the two components due to their different sintering kinetics. This results in poor densification of the blends.
- Particle size plays the main role in material densification and in the phases distribution. The negative interaction during co-sintering can be reduced by selecting powders with smaller particles size. Moreover the particle size ratio (PSR) influences the phase distribution and thus the material properties. It has been proved that fully dense blends with a good dispersion of the reinforcing particles can be sintered by small sized powders setting the PSR smaller than 1. The finer and more homogeneous microstructure of these fully dense hybrid steels result in high hardness and high toughness.

- MM has been successfully applied to reduce the particle size of HWTS and HSS powders, so to enhance sintering. Spark plasma sintered MM-samples achieve near full density confirming that the interference during co-sintering can be minimized or completely eliminated by reducing the powder particle size.
- For the MM-blends hardness shows a positive deviation from the linear rule of mixture which can plausibly suggest that the dispersion of particles of a second constituent modifies the stress field resulting in increased work hardening of the matrix. On the other hand the lack of a suited protection against oxidation for MM-powders has caused a sharp increase of the oxygen content resulting in a marked drop of toughness for the two base MM-steels compared to that of samples produced using as-atomized powders. In spite of this higher oxygen content the toughness of the MM-blends is higher than that of the as-atomized blends. Indeed the positive influence of a higher density largely compensates the detrimental influence of the higher oxygen content.

7.2   HWTS Based MMCs

The second part of research has concerned the development of HWTS based metal matrix composites (MMCs), considering different production routes for the composite powders (i.e. powder mixing and MA) and different reinforcing compounds (i.e. TiB_2, TiC and TiN). The main result are summarized in the following:

- Due to the high PSR, the powder-mixed sample shows the presence of big TiB_2 aggregates, which enclose large pores. HWTS particle size is the limiting factor for producing fully dense MMCs by powder mixing. Since it is difficult to reduce the steel particle size below a certain limit, even using longer milling time, it is practically impossible to avoid aggregates and thus to increase relative density by easy powder mixing.
- Problems related to the PSR have been overcome by MA which promotes a uniform dispersion of TiB_2 fragments into the parent steel particles avoiding the formation of agglomerates. This assures the achievement of high relative density. It can be stated that MA is a suited technology for MMC production.
- Microstructural characterization have highlighted the formation of TiC and Fe_2B in the sintered composites, meaning that TiB_2 and HWTS react during sintering. These results clearly point out that the carbon, which is present in the steel matrix, destabilizes TiB_2 allowing the formation of new compounds. Moreover the TiB_2-steel interaction inhibits the ferrite to austenite transformation thus the steel matrix cannot be heat treated anymore. These results prove that TiB_2 is not a suitable reinforcement for the production of HWTS based MMCs.
- Thermodynamic calculations and X-ray diffraction analyses show that TiC and TiN are chemically stable in the steel matrix. Microhardness confirms the martensitic microstructure of the steel matrix and shows that TiC has higher

hardening effect. On the other hand, after only 1 minute of sintering, hardness is negatively influenced by porosity, thwarting the hardening effect of HPs. Thus the hardness of both MA-samples is lower than what expected from microhardness measurements.

- The TiN-reinforced MMC is characterized by higher resistance to densification and after 30 minutes of sintering its relative density is still lower that 95%. For this composite sintering seems to be influenced by densification mechanisms other than power-law creep. Microstructure investigations show interconnected porosity and small sintering necks. This may suggest that the oxide layer influences diffusion mechanisms changing the sintering kinetic. Longer sintering time can be considered but it has to be noticed that a strong point of SPS is the shorter processing time. If the holding time is further increased the SPS becomes less convenient than customary processes, such HIP.

- For the 20%$_{vol}$TiC-reinforced MMC density quickly increases in the early minutes of the holding stage, then the densification rate decreases and after 30 minutes the composite reaches nearly full density (99.36%).

List of abbreviations and acronyms

AFM   atomic force microscopy
BPR   ball to powder ratio
DC   direct continuous
EDXS   energy-dispersive X-ray spectroscopy
FGM   functionally graded material
HHS   high speed steel
HIP   hot isostatic pressing
HP   hard particle
HWTS   hot work tool steel
MA   mechanical alloying
MM   mechanical milling
MMC   metal matrix composite
PCA   process control agent
PM   powder metallurgy
PSR   particle size ratio
PVD   physical vapour deposition
SEM   scanning electron microscopy
SKPFM   Scanning Kelvin Probe Force Microscopy
SPS   spark plasma sintering
TEM   transmission electron microscopy
XRD   X-rays diffraction

References

Abderrazak H., F. Schoenstein, M. Abdellaoui, N. Jouini, *Spark plasma sintering consolidation of nanostructured TiC prepared by mechanical alloying*. International Journal of Refractory Metals and Hard Materials, **2011**. 29: p. 170-176.

Adachi J., K. Kurosaki, M. Uno, S. Yamanaka, *Porosity influence on the mechanical properties of polycrystalline zirconium nitride ceramics.* Journal of Nuclear Materials, **2006**. 358: p. 106-110.

Akhtar F., *Microstructure evolution and wear properties of in situ synthesized TiB_2 and TiC reinforced steel matrix composites*. Journal of Alloys and Compounds, **2008**. 459: p. 491-497.

Angers R., M.R. Krishnadev, R. Tremblay, J. Corriveau, D. Dubé, *Characterization of $SiC_p/2024$ aluminium alloy composites prepared by mechanical processing in a low energy ball mill*. Material Science and Engineering A, **1999**. 262: p. 9-15.

Arnberg L., A. Karlsson, *Influence of powder surface oxidation on some properties of a HIPped martensitic chromium steel*. International Journal of Powder Metallurgy, **1988**. 24: p. 107-112.

Artz E., M.F. Ashby, K.E. Easterling, *Practical Applications of Hot-Isostatic Pressing Diagrams: Four Case Studies*. Metallurgical Transactions A, **1983**. 14: p. 211-221.

Bailon-Poujol I., J.P. Bailon, G. L'Espèrance, *Ball-mill grinding kinetics of master alloys for steel powder metallurgy applications*. Powder Technology, **2011**. 210: p. 267-272.

Benjamin J.S., *Dispersion Strengthened Speralloys by Mechanical Alloying*. Metallurgical Transaction, **1970**. 1: p. 2943-2951.

Benjamin J.S., M.J. Bomford, *Dispersion Strengthened Aluminum Made by Mechanical Alloying.* Metallurgical Transaction A, **1977**. 8: p. 1301-1305.

Benjamin J.S., R.D. Schelleng, *Dispersion Strengthened Aluminum-4 Pct Magnesium Alloy Made by Mechanical Alloying*. Metallurgical Transaction A, **1981**. 12: p. 1827-1832.

Benjamin J.S., T.E. Volin, *The Mechanism of Mechanical Alloying*. Metallurgical Transactions, **1974**. 5: p. 1929-1934.

Berns H., *Comparison of wear resistant MMC and white cast iron*. Wear, **2003**. 254: p. 47-54.

Berns H., A. Melander, D. Weichert, N. Asnafi, C. Broeckmann, A. Gross-Weege, *A new material for cold forging tools*. Computational Material Science, **1998**. 11: p. 166-180.

Berns H., F.D. Sinesio, *Effect of coarse hard particles on high-temperature sliding abrasion of new metal matrix composites*. Wear, **1997**. 203-204: p. 608-614.

Berns H., S. Koch, *Influence of abrasive particles on wear mechanism and wear resistance in sliding abrasion tests at elevated temperatures*. Wear, **1999**. 233-235: p. 424-430.

Berns H., N. von Chuong, *A new microstructure for PM toolling material*. Metallugical Physical Advanced Technology, **1996**. 6: p. 61-71.

Berns H., T. Schneiders, W. Theisen, *Properties of double dispersed tool steels*. in *Proceedings of the 7th International Tooling Conference*. **2006**. Turin (Italy). p. 77-84.

Bolton J.D., A.J. Gant, *Fracture in ceramic-reinforced metal matrix composites based on high-speed steel*. Journal of Material Science, **1998**. 33: p. 939-953.

Bonnenfant D., F. Mazerolle, P. Suquet, *Compaction of powders containing hard inclusions: experiments and micromechanical modelling*. Mechanics of Materials, **1998**. 29: p. 93-109.

Bouvard D., *Densification behaviour of mixtures of a hard and soft powders under pressure*. Powder Technologies, **2000**. 111: p. 231-239.

Çetinkaya C., T. Findik, S. Özbilen, *An investigation into the effect of experimental parameters on powder grain size of the mechanically milled 17-4 PH stainless steel powders*. Materials and Design, **2007**. 28: p. 773-782.

Chawla N., K. Chawla, *Metal Matrix Composites*. **2006**, New York: Springer.

Cho J.H., K.T. Kim, *Densification of mixed metal powder at high temperature*. International Journal of Mechanical Science, **2001**. 43: p. 921-933.

Dai L., Y. Liu, Z. Dong, *Size and structure evolution of yttria in ODS ferritic alloy powder during mechanical milling and subsequent annealing*. Powder Technology, **2012**. 217: p. 281-287.

Degnan C.C., P.H. Shipway, *A comparison of the reciprocating sliding wear behaviour of steel based metal matrix composites processed from self propagation high-temperature synthesised Fe-TiC and Fe-TiB$_2$ masteralloys*. Wear, **2002**. 252: p. 832-841.

Delie F., D. Bouvard, *Effect of inclusion morphology on the densification of powder composites*. Acta Materialia, **1998**. 46: p. 3905-3913.

Delogu F., *A few details of the austenite to martensite phase transformation in 304 stainless steel powders under mechanical processing*. Acta Materialia, **2011**. 59: p. 2069-2074.

Diouf S., A. Molinari, *Densification mechanisms in spark plasma sintering. Effect of particle size and pressure*. Powder Technology, **2012**. 221: p. 220-227.

dos Santos J.A.B.O., W.F. Sales, S.C. Santos, A.R. Machado, M.B. da Silva, J. Bonney, E.O. Ezugwu, *Tribological evaluation of TiN and TiAlN coated PM-HSS gear cutter when machining 19MnCr5 steel*. International Journal of Advanced Manufacturing and Technologies, **2007**. 31: p. 629-637.

Du B., S.R. Paital, N.B. Dahotre, *Phase constituents and microstructure of laser synthesized TiB$_2$–TiC reinforced composite coating on steel*. Scripta Materialia, **2008**. 59: p. 1147-1150.

Duarte A., M. Vila, F.J. Oliveira, F.M. Costa, *Structure and morphology of TiB$_2$ duplex coatings deposited over X40 CrMoV 5-1-1 steel by DC magnetron sputtering*. Vacuum, **2009**. 83: p. 1291-1294.

Deutsche Edelstahlwerke, Ferro-Titanit®. http://www.ferro-titanit.com/en/home/

El-eskandarany M.S., *Mechanical alloying for fabrication of advanced engineering materials*. **2001**, New York: William Andrew Publishing.

Farid A, S. Guo, F. Cui, P. Feng, T. Lin, *TiB$_2$ and TiC stainless steel matrix composites*. Materials Letters, **2007**. 61: p. 189-191.

Fecht H.J., *Nanostructure formation by mechanical attrition*. Nanostructured Materials, **1995**. 6: p. 33-42.

Fedrizzi A., M. Pellizzari, M. Zadra, *Influence of particle size ratio on the densification behaviour of AISI H13/AISI M3:2 powder mixture*. Powder Technology, **2012[1]**. 228: p. 435-442.

Fedrizzi A., M. Pellizzari, M. Zadra, *Production of hybrid tool steel by mechanical milling and spark plasma sintering*. In *Proceedings of the 2012 Powder Metallurgy World Congress & Exhibition*. **2012[2]**. Yokohama (Japan).

Fedrizzi A., M. Pellizzari, M. Zadra, *Production of a particle reinforced hot work tool steel by mechanical alloying*. La Metallurgia Italiana, **2013[1]**. 105: In Press.

Fedrizzi A., M. Pellizzari, M. Zadra, F. Dies, *Fabbrication of fine grained hot work tool steel by mechanical milling and spark plasma sintering*. In *Proceedings of the 2012 Powder Metallurgy World Congress & Exhibition*. **2012[3]**. Yokohama (Japan).

Fedrizzi A., M. Pellizzari, M. Zadra, E. Marin, *Densification and microstructure analysis of hot work tool steel matrix composites reinforced with TiB$_2$ particles*. Submitted to Materials Characterizzation **2013[2]**.

German R.M., *Sintering densification for powder mixtures of varying distribution widths*. Acta Metallurgica Materialia, **1992[1]**. 40: p. 2085-2089.

German R.M., *Prediction of sintered density for bimodal powder mixtures*. Metallurgical Transactions A, **1992[2]**. 23: p. 1455-1465.

Grinder O., *PM HSS and tool steels - Present state of the art and development trends*. In *Proceedings of the 5th International Conference on Tooling*. **1999**. Leoben (Austria). p. 39-58.

Guo W., A. Iasonna, M. Magini, S. Martelli, F. Padella, *Synthesis of amorfhous and metastable Ti$_{40}$Al$_{60}$ alloys by mechanical alloying of elemental powders*. Journal of Material Science, **1994**. 29: p. 2436-2444.

Helle A.S., K.E. Easterling, M.F. Ashby, *Hot-isostatic pressing diagrams: new developments*. Acta metallurgia, **1985**. 33: p. 2163-2174.

Hillskog T., *Powder-Metallurgy Tool Steel: an overview*. Metalforming Magazine, **2003**. p. 48-51.

Huang H., J. Ding, P.G. McCormick, *Microstructural evolution of 304 stainless steel during mechanical milling*. Material Science and Engineering A, **1996**. 216: p. 178-184.

Hulbert D.M., A. Anders, J. Andersson, E.J. Lavernia, A.K. Mukherjee, *A discussion on the absence of plasma in spark plasma sintering*. Scripta Materialia, **2009**. 60: p. 835-838.

Imbert C., N.D. Ryan, H.J. McQueen, *Hot workability of three grades of tool steel*. Metallurgical Transactions A, **1984**. 15: p. 1855-1864.

Jagota A., G.W. Scherer, *Viscosity and sintering rates of composite packings of spheres*. Journal of American Ceramic Society, **1995**. 78: p. 521-528.

Koch C.C., O.B. Cavin, C.G. McKamey, J.O. Scarbrough, *Preparation of "amorphous" Ni$_{60}$Nb$_{40}$ by mechanical alloying*. Applied Physics Letters, **1983**. 43: p. 1017-1019.

Kugler G., R. Turk, T. Večko-Pirtovšek, M. Terčelj, *Wear behaviour of nitrided microstructures of AISI H13 dies for hot extrusion of aluminium*. Metalurgija, **2006**. 45: p. 21-29.

Kuhrt C., H. Schropf, L. Schultz, E. Arztz, *Syntesis of nanocrystalline FeAl and NiAl by mechanical alloying*. In *2nd International Conference on Structural Applications of Mechanical Alloying*. **1993**. Vancouver (Canada). p. 269-273.

Lange F.F., L. Atteraas, F. Zok, *Deformation consolidation of metal powders containing steel inclusion*. Acta Metallurgical Materialia, **1991**. 39: p. 209-219.

Lee B.W., J. Jang, D. Kwon, *Evaluation of fracture toughness using small notched specimens*. Materials Science and Engineering A, **2002**. 334: p. 207-214.

Lemster K., T. Graule, T. Minghetti, C. Schelle, J. Kuebler, *Mechanical and machining properties of X38CrMoV5-1/Al$_2$O$_3$ metal matrix composites and components*. Materials Science and Engineering A, **2006**. 420: p. 296-305.

Li B., Y. Liu, J. Li, H. Cao, L. He, *Effect of sintering process on the microstructures and properies of in situ TiB$_2$-TiC reinforced steel matrix composites produced by spark plasma sintering*. Journal of Material Processing and Technologies, **2010**. 210: p. 91-95.

Li Y., X. Li, Y. Long, W. Xia, M. Zhu, W. Chen, *Fabrication of iron-base alloy by spark plasma sintering*. Journal of Materials Science and Technology, **2006**. 22: p. 257-260.

Libardi S., M. Zadra, F. Casari, A. Molinari, *Mechanical properties of nanostructured and ultrafine-grained iron alloys produced by spark plasma sintering of ball milled powders*. Materials Science and Engineering A, **2008**. 478: p. 243-250.

Liu Z.Y., N.H. Loh, K.A. Khor, S.B. Tor, *Mechanical alloying of TiC/M2 high speed steel composite powders and sintering investigation*. Material Science and Engineering A, **2001**. 311: p. 13-21.

Luo J., R. Stevens, *Porosity-dependence of elastic moduli and hardness of 3Y-TZP ceramics*. Ceramics International, **1999**. 25: p. 281-286.

Lutterotti L., *Materials Analysis Using Diffraction (MAUD)*, **1997**. http://www.ing.unitn.it/~maud/

Ma Y.-P., X.-I. Li, C.-H. Wang, L. Lu, *Microstructure and impact wear resistance of TiN reinforced high manganese steel matrix*. International Journal of Iron Steel Resistance, **2012**. 17: p. 60-65.

Mamedov V., *Spark plasma sintering as advanced PM sintering method*. Powder Metallurgy, **2002**. 45: p. 322-328.

Matula G., L.A. Dobrzański, *Structure and properties of FGM manufactured on the basis of HS6-5-2*. Journal of Achievements in Materials and Manufacturing Engineering, **2006**. 17: p. 101-104.

Maurice D., T.H. Courtney, *Modelling of mechanical alloying: part I. Deformation, coalescence and fragmentation mechanisms*. Metallurgical Material Transactions A, **1994**. 25: p. 147-158.

Munir Z.A., U. Anselmi-Tamburini, M. Ohyanagi, *The effect of electric field and pressure on the synthesis and consolidation of materials: A review of the spark plasma sintering method*. Journal of Materials Science, **2006**. 41: p. 763-777.

Oh-ishi K., H.W., Zhang, T. Ohkubo, K. Hono, *Microstructure characterization of bulk nanocrystalline Fe-0.8C alloy produced by mechanical milling and spark plasma sintering*. Material Science and Engineering A, **2007**. 456: p. 20-27.

Olevsky E., L. Froyen, *Constitutive modelling of spark-plasma sintering of conductive materials*. Scripta Materialia, **2006**. 55: p. 1175-1178.

Oliveira M.M., J.D. Bolton, *High-speed steels: increasing wear resistance by adding ceramic particles*. Journal of Materials Processing Technology, **1999**. 92-93: p. 15-20.

Omori M., *Sintering, consolidation, reaction and crystal growth by the spark plasma system (SPS)*. Materials Science and Engineering A, **2000**. 287: p. 183-188.

Pagounis E., V.K. Lindroos, *Development and Performance of New Hard and Wear-Resistant Engineering Materials*. Journal of Materials Engineering and Performance, **1997**. 6: p. 749-756.

Pagounis E., V.K. Lindroos, *Processing and properties of particulate reinforced steel matrix composites*. Materials Science and Engineering A, **1998**. 246: p. 221-234.

Pellizzari M., A. Fedrizzi, F. Dies, Production of a novel hot work tool steel by mechanical milling and spark plasma sintering. In Proceedings of the 9th International Tooling Conference. **2012**. Leoben (Austria). p. 207-214.

Pellizzari M., A. Fedrizzi, M. Zadra, *Influence of processing parameters and particle size on the properties of hot work and high speed tool steels by spark plasma sintering*. Materials and Design, **2011[1]**. 32: p. 1796-1805.

Pellizzari M., A. Fedrizzi, M. Zadra, *Spark Plasma co-Sintering of hot work and high speed steel powders for fabrication of a novel tool steel with composite microstructure*. Powder technology, **2011[2]**. 214: p. 292-299.

Pellizzari M., M. Zadra, A. Fedrizzi, *Development of a hybrid tool steel produced by Spark Plasma Sintering*. Materials and Manufacturing Processes, **2009**. 24: p. 873-878.

Pramanik A., L.C. Zhang, J.A. Arsecularatne, *Deformation mechanisms of MMCs under indentation*. Composite Science and Technology, **2008**. 68: p. 1304-1312.

Rajasekaran B., G. Mauer, R. Vaßen, A. Röttger, S. Weber, W. Theisen, *Development of cold work tool steel based-MMC coating using HVOF spraying and its HIP densification behaviour*. Surface and Coatings Technology, **2010**. 204: p. 3858-3863.

Reade, Ferro-Tic Alloys. http://www.reade.com/Products/Ferro_Alloys/ferro_tic.html

Rietveld H.M., *A profile refinement method for nuclear and magnetic structures*. Journal of Applied Crystallography, **1969**. 2: p. 65-71.

Roberts G.A., R.A. Cary, *Tool Steels*. **1992**, Ohio: American Society for Metals.

Rodenburg C., M. Krzyzanowski, J.H. Beynon, W.M. Rainforth, *Hot workability of spray-formed AISI M3:2 high-speed steel*. Materials Science and Engineering A, **2004**. 386: p. 420-427.

Sadagopan D., R. Pitchumari, *Application of genetic algorithms to optimal tailoring of composite materials*. Composites Science and Technology, **1998**. 58: p. 571-589.

Salahinejad E., R. Amini, E. Askari Bajestani, M.J. Hadianfard, *Microstructural and hardness evolution of mechanically alloyed Fe-Cr-Mn-N powders*. Journal of Alloys and Compounds, **2010**. 497: p. 369-372.

Shen Y.-L., N. Chawla, *On the correlation between hardness and tensile strength in particle reinforced metal matrix composites*. Material Science and Engineering A, **2001**. 297: p. 44-47.

Sigl S.L., K. Schwetz, *TiB$_2$-based cermet borides: a new generation of hardmetals*. PIM, **1991**. 23: p. 221-224.

Söderberg S., *Advances in coating technology for metal cutting tools*. Metal Powder Report, **2001**. 56: p. 24-30.

Song X., X. Liu, J. Zhang, *Neck formation and self-adjusting mechanism of neck growth of conducting powders in spark plasma sintering*. Journal of the American Ceramic Society, **2006**. 89: p. 494-500.

Staab G.H., *Laminar composites*. **1999**, Boston, USA: Butterworth-Heinemann.

Sundman B., B. Jansson, J.-O. Andresson, *The Thermo-Calc databank system*. Calphad, **1985**. 9: p. 153-190.

Suryanarayana C., *Mechanical alloying and milling*. Progress in Materials Science, **2001**. 46: p. 1-184.

Tanaka K., T. Saito, *Phase equilibria in TiB$_2$-reinforced high modulus steel*. Journal of Phase Equilibria, **1999**. 20: p. 207-214.

Ting J.M., R.Y. Lin, *Effect of particle size distribution on sintering - part I modelling*. Journal of Materials Science, **1994**. 29: p. 1867-1872.

Ting J.M., R.Y. Lin, *Effect of particle size distribution on sintering - part II sintering*. Journal of Materials Science, **1995**. 30: p. 2382-2389.

Tjong S.C., K.C. Lau, *Properties and abrasive wear of TiB$_2$/Al-4%Cu composites produced by hot isostatic pressing*. Composite Science and Technologies, **1999[1]**. 59: p. 2005-2013.

Tjong S.C., K.C. Lau, *Sliding wear of stainless steel matrix composite reinforced with TiB$_2$ particles*. Materials Letters, **1999[2]**. 41: p. 153-158.

Tjong S.C., Z.Y. Ma, *Microstructural and mechanical characteristics of in situ metal matrix composites*. Materials Science and Engineering R, **2000**. 29: p. 49-113.

Tokita M., Mechanism of Spark Plasma Sintering. Journal of the Society of Powder Technology Japan, **1993**. 30: p. 790-804.

Wilcox B.A., I.G. Wright, *Observations on strengthening and oxidation behavior of a dispersion hardened Fe-Cr-base alloy prepared by mechanical alloying*. Metallurgical Transactions, **1974**. 5: p. 957-960.

Xu Z., C.-C. Jia, C. Kuang, K. Chu, X. Qu, *Spark plasma sintering of nitrogen-containing nickel-free stainless steel powders and effect of sintering temperature*. Journal of Alloys and Compounds, **2009**. 484: p. 924-928.

Zavaliangos A., A. Laptev, *The densification of powder mixtures containing soft and hard components under static and cycling pressure*. Acta Materialia, **2000**. 48: p. 2565-2570.

Zhaohui Z., W. Fuchi, W. Lin, L. Shukui, S. Osamu, *Sintering mechanism of large-scale ultrafine-grained copper prepared by SPS method*. Materials Letters, **2008**. 62: p. 3987-3990.

Zhong H.L., Y. Fang, C. Kuang, X. Kuang, Q. Hao, X. Li, *Development of powder metallurgy high speed steel*. Materials Science Forum, **2010**. 638-642: p. 1854-1859.

Zhu S., K. Iwasaki, *Characterization of mechanically alloyed ternary Fe-Ti-Al powders*. Materials Science Engineering A, **1999**. 270: p. 170-177.

Zoz H., K. Ameyama, S. Umekawa, H. Ren, D.V. Jaramillo, *The millers' tale: high-speed steel made harder by attrition*. Metal Powder Report, **2003**. 58: p. 18-29.

Zum Gahr K.-H., *Wear by hard particles*. Tribology International, **1998**. 31: p. 587-596.

Scientific Production

International Journal

[1] M. Pellizzari, M. Zadra, **A. Fedrizzi**, *Development of a hybrid tool steel produced by spark plasma sintering*, Materials and Manufacturing Processes 24:7 (2009) 873-878.

[2] M. Pellizzari, **A. Fedrizzi**, M. Zadra, *Influence of processing parameters and particle size on the properties of hot work and high speed tool steels by spark plasma sintering*, Materials and Design 32:4 (2011) 1796-1805.

[3] M. Pellizzari, **A. Fedrizzi**, M. Zadra, *Spark plasma co-sintering of hot work and high speed steel powders for fabrication of a novel tool steel with composite microstructure*, Powder Technologies 214 (2011) 292-299.

[4] **A. Fedrizzi**, M. Pellizzari, M. Zadra, *Influence of particle size ratio on densification behavior of AISI H13 / AISI M3:2 powder mixture*, Powder Technologies 228 (2012) 435-442.

[5] N. Vicente, **A. Fedrizzi**, N. Bazzanella, F. Casari, F. Buccioti and A. Molinari, *Microstructure of interface of SPS co-sintered and sinter bonded cp2-Ti and Co–28Cr–6Mo*, Powder Metallurgy (2012) DOI 10.1179/1743290112Y.0000000040.

[6] S. Diouf, **A. Fedrizzi**, A. Molinari, *A fractographic and microstructural analysis of the neck regions of coarse copper particles consolidated by Spark Plasma Sintering*, Submitted to Materials Letters (2013).

[7] **A. Fedrizzi**, M. Pellizzari, M. Zadra, E. Marin, *Densification and microstructure analysis of hot work tool steel matrix composites reinforced with TiB2 particles*, Submitted to Materials Characterization (2013).

National Journal

[1] **A. Fedrizzi**, M. Pellizzari, M. Zadra, *Sviluppo di un acciaio per lavorazione a caldo rinforzato tramite alligazione meccanica*, La Metallurgia Italiana, 105 (2013) in Press.

[2] **A. Fedrizzi**, M. Pellizzari, M.Zadra, F. Francesco, *Studio del processo di macinazione meccanica di un acciaio per lavorazioni a caldo*, La Metallurgia Italiana, (2013) Accepted.

Proceedings

[1] **A. Fedrizzi**, M. Pellizzari, *Properties of an 80%H13-20%M3:2 PM tool steel produced by Spark Plasma Sintering*, Proc. 3rd Int. Conf. on "Heat Treatment and Surface Engineering of Tools and Dies, Wels (Austria) 2011, pp. 181-189.

[2] **A. Fedrizzi**, M. Pellizzari, M. Zadra, *Spark Plasma Sintering of mechanically milled hot work tool steel powder*, Proc. European Powder Metallurgy Congress & Exhibition - EUROPM2011, Barcelona (Spain) 2011, vol. 1, pp. 165-170.

[3] M. Pellizzari, **A. Fedrizzi**, F. Dies, *Production of a novel hot work tool steel by mechanical milling and spark plasma sintering*, Proc. of the 9th International Tooling Conference, Tool12, Leoben (Austria) 2012, pp. 207-214.

[4] **A. Fedrizzi**, M. Pellizzari, M. Zadra, *Production of a hybrid tool steel by mechanical milling and spark plasma sintering*, Proc. of the 2012 Powder Metallurgy World Congress & Exhibition, Yokohama (Japan) 2012, on electronic support.

[5] **A. Fedrizzi**, M. Pellizzari, M. Zadra, F. Dies, *Fabrication of fine grained hot work tool steel by mechanical milling and spark plasma sintering*, Proc. of the 2012 Powder Metallurgy World Congress & Exhibition, Yokohama (Japan) 2012, on electronic support.

Acknowledgments

… e quelli meno formali…

Come nelle migliori opere, sono giunta anch'io alla fine dell'ultimo capitolo di questa trilogia metallurgica ed è quindi doveroso (tri)nominare chi mi ha sostenuto e accompagnato (in varia maniera) in questo percorso…

Un ringraziamento di cuore va a Mario, sempre disponibile a chiarire i miei dubbi, a sostenermi e indirizzarmi nel percorso e a consigliarmi con franchezza e discrezione. Restando in quel di Pergine, segue Luca, che mi ha sempre spronato a puntare all'obiettivo. Inoltre un grazie ad entrambi per il contributo materiale! Senza i campioni della K4Sint ovviamente non avrei potuto scrivere una sola virgola!!!

Con immenso affetto ringrazio tutte le "girls di Metallurgia"! Prime fra tutte Cinzia e Lorena! Siete state due meravigliose compagne di viaggio, dal punto di vista lavorativo ma molto più importante dal punto di vista umano. Sempre pronte e disponibili, siete un supporto costante per tutti e la forza e l'energia con cui affrontate qualsiasi cosa sono un insegnamento che porterò sempre con me. Segue Melania, costante e insostituibile presenza in tutti questi tre anni, compagna di ufficio, ma soprattutto carissima amica! Un ringraziamento poi a tutte le metallurgiste che si sono avvicendate, Elena e Ketner nei primi anni, seguite da Giulia e Elisa con cui abbiamo monopolizzato l'ufficio! E un affettuoso ricordo a Giusy…

Ovviamente non posso trascurare la parte maschile del laboratorio! Pertanto un grazie va al mio "compagno di banco" Nerio, con cui ho condiviso tutti i crucci di questo SPS, ma soprattutto tanti momenti gioiosi; un ringraziamento speciale a Zanza che mi ha sempre sostenuta; ringrazio Saliou per tutti i lunghi discorsi sulla metallurgia e non solo; Marcolino, punto di riferimento quando la strumentazione di laboratorio proprio non ne voleva sapere di stare dalla mia; Ibo sempre pronto per dare una mano o semplicemente fare due chiacchiere (o due foto!); grazie a Nicolò, Luca, Lazslo, Piergiorgio, Pedro e tutti i tesisti che si sono susseguiti, con un ringraziamento particolare a Francé sostegno sia materiale che morale di questo lavoro. Per adozione rientra nel gruppo anche Talla, che ha reso molto più gioiosi i viaggi in treno!